THE TRIBOLOGICAL BEHAVIOUR OF A HIGH NITROGEN MANGANESE AUSTENITIC STAINLESS STEEL

BY DUNCAN JOHN MILLS

A Thesis submitted to the Faculty of Engineering, University of Cape Town in fulfilment of the degree of Master of Science in Applied Science.

Department of Materials Engineering

University of Cape Town

September 1995

1. ABSTRACT

The tribological behaviour of two experimental alloys, namely a high nitrogen manganese austenitic stainless steel and a vanadium micro-alloyed stainless steel is compared to the tribological behaviour of standard stainless steels AISI 304 and AISI 316 and to the wear resistant steel, Hadfields manganese steel. The wear tests performed on these steels were abrasion, abrasion-corrosion and cavitation erosion.

The high nitrogen alloy contained 0.63wt% nitrogen and 0.83wt% nickel and was found to have mechanical properties superior to the other steels studied in this thesis. This alloy was also subject to cold deformation and strain ageing and the wear resistance of the material in these different conditions was measured. No mechanical testing was performed on the vanadium micro-alloyed steel because of specimen size constraints. Hardness tests were performed on the high nitrogen alloy after deformation and ageing treatments at different temperatures for different times and the results show an improvement in hardness.

Under abrasion Hadfields manganese steel has the best abrasion resistance followed by the vanadium micro-alloyed steel, the high nitrogen alloy and then AISI 316 and AISI 304.

The abrasion-corrosion results show that the vanadium micro-alloyed steel and the high nitrogen alloy have the best abrasion-corrosion resistance followed by AISI 316 and AISI 304 and lastly Hadfields manganese steel.

The high nitrogen stainless steel shows a decrease in the abrasion resistance with an increase in the amount of prior cold deformation. Strain ageing is found to have no effect on the abrasion resistance. This is in contrast to the results for cavitation erosion where there is an improvement in the cavitation erosion resistance with an increase in the amount of cold deformation. Strain ageing improves the cavitation resistance especially when material with between 16% and 48% prior cold deformation is strain aged

Abrasion-corrosion was not performed on the processed material as the test is not sensitive enough to record any differences.

For the vanadium micro-alloyed steel it is seen that despite there being an improvement in the hardness of the alloy with increased ageing time there is no corresponding

increase in the abrasion resistance. With regard to cavitation erosion resistance, ageing treatments at 700°C lead to an improvement in the steady state erosion rate and an increase in the incubation time. After ageing at 900°C the steady state erosion rate shows no change whilst the incubation time increases.

ACKNOWLEDGEMENTS

To,

Rob Knutsen,
Glen Newins,
Nick Dreeze,
Bernard Greeves,
James Petersen ,
Reggie Hendricks,

and to everyone else who contributed to this thesis
thank you for your help, hardwork and encouragement.

And thank you to

Columbus Stainless Steel and Chris Rennhard,
FRD
and UCT
for material and financial support.

Dedicated to Jeanine

CONTENTS

2. INTRODUCTION

It has long been known that the addition of nitrogen can impart beneficial properties to stainless steels [9,11]. The most important effect is that nitrogen is a potent austenite stabiliser and can be used to replace nickel in austenitic stainless steels. Ground work for the production of these nitrogen rich alloys began in the 1960's when the USA worked on finding elements which could be used to replace nickel in austenitic steels. The AISI 200 series steels were developed as a consequence of this research. In these steels the nickel content has been reduced to about 5wt% and nitrogen has been introduced to about 0.25wt%. It is important to note that the nitrogen has to remain in solid solution to stabilise the austenite and to improve the mechanical properties. The reason for the nickel not being completely substituted with nitrogen was that production technology was not available to enable stainless steels to be alloyed with nitrogen above the solubility of nitrogen at atmospheric pressure. In the early 1980's pressurised furnaces were developed which made it possible to produce steel with high nitrogen contents but these furnaces could only produce limited quantities of the steel and were therefore not commercially viable. More recently research has been completed which shows that nitrogen can be introduced into the steel at atmospheric pressure with the addition of the appropriate alloying elements[18]. These alloying elements are necessary to increase the solid solubility of nitrogen. It is for this reason that the stainless steel under investigation has such a high manganese content. Manganese is found to increase the solubility of nitrogen

These stainless steels have considerably better mechanical properties than other austenitic steels like AISI 304 and AISI 316 and it is these good mechanical properties and their good corrosion resistance which make them candidates for wear resistant applications. There has been relatively little work done on the wear behaviour of these high nitrogen stainless steels. Another approach to strengthening stainless steels is by the formation of precipitates, and these precipitates are often found to be particularly good at improving the abrasion resistance of the steel. A high nitrogen steel of this nature is included in the study and is investigated to find out whether there is any heat treatment which could improve the wear resistance of this steel . The objectives of this thesis are as follows:

1. To compare the abrasion, abrasion-corrosion and cavitation erosion of the high nitrogen and the vanadium micro-alloyed steel to Hadfields manganese steel, AISI 304, AISI 316 and mild steel and to explain any differences between the wear behaviour of these steels.

2. To investigate whether or not mechanical and/or thermal treatments could improve the wear properties of the high nitrogen stainless steel and to explain any differences that might be found.

3. To study the effects of ageing time and temperature on the wear behaviour of the vanadium micro-alloyed stainless steel.

3. LITERATURE REVIEW

3.1. Stainless Steels

Stainless steels, by virtue of their alloy composition, production history and crystallography fall into three main categories, namely austenitic, ferritic or martensitic steels. Duplex steels have been developed and these are made up of a combination of ferrite and austenite. The type of steel produced is very dependent on the chromium content and a steel that contains more than 12wt% Cr usually exibits sufficient corrosion resistance to be called a stainless steel. Above 12wt% chromium the steel is usually ferritic as the property and nature of the steel is dictated by the alloy composition.

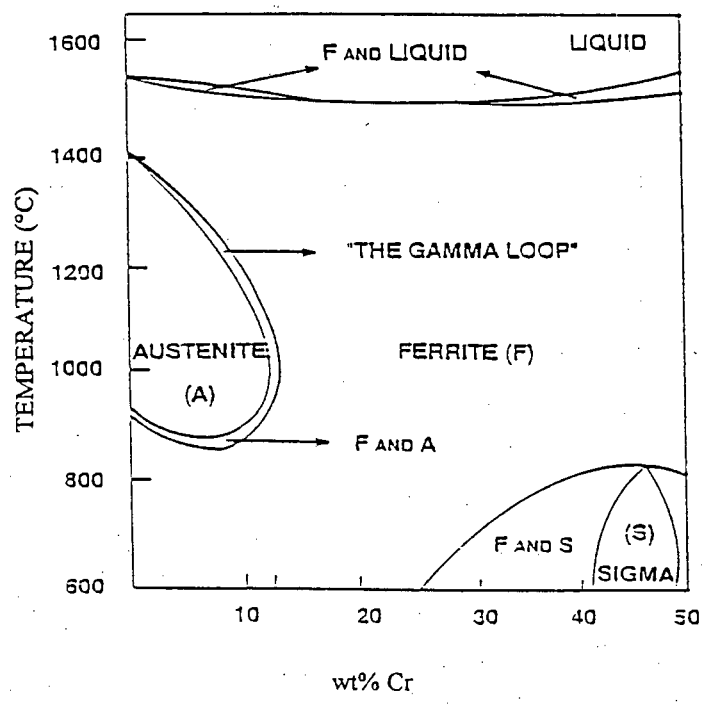

Figure 3.1: Section of the Iron - Chromium (Fe-Cr) Phase Diagram[1].

Figure 3.1 shows the Fe - Cr phase diagram and this phase diagram dictates the phase of a stainless steel. The austenite and ferrite areas are clearly indicated and martensite can be produced, after an appropriate heat treatment, by a diffusionless phase transformation from austenite. Since chromium is a strong ferrite former, in order to obtain an austenitic structure it is necessary to extend the austenite loop in stainless steels containing more than 12wt%

chromium. This can be achieved by adding either substitution or interstitial austenite formers. Substitutional austenite formers are elements which take the place of the iron (Fe) in the crystal structure and, because of their size and interaction with the matrix, stabilise the austenitic structure. Nickel (Ni) and manganese (Mn) are elements most commonly used for this purpose. Interstitial austenite stabilisers are atoms that are held in the interstitial sites of the face centred cubic (f.c.c.) austenite structure and from there hinder any transformation of the desirable austenite phase to ferrite or martensite. Carbon (C) and Nitrogen (N) are elements of this nature.

3.2. Austenitic Stainless Steels

The development of the austenitic stainless steel family, with improved mechanical and corrosion properties, began in the sixties and the widespread use thereof became prevalent in the eighties[2]. There is currently a wide range of austenitic steels, either stable or metastable, available on the market, all of which offer excellent corrosion resistance, good yield strength and good toughness. Table 3.1 describes a few common austenitic steels and their properties. This table gives an indication of the range of austenitic steels currently available. Hadfields manganese steel has been included in the table as it is a wear resistant austenitic steel, it has no chromium and is therefore not a stainless steel, but it is wide availability and its good wear resistance make it a good standard for comparison in this thesis.

Alloy	Yield Strength (MPa)	Tensile Strength (MPa)	Corr. Resis.	SFE ($mJ.m^{-2}$)
AISI 304	310[3]	600[3]	good	30[4]
AISI 316	310[3]	580[3]	good	78[7]
AISI 201	260[5]	655[5]	good	40[7]
Hadfields	350[6]	700[6]	bad	+/- 21[7]

Table 3.1: A few common austenitic steels and their properties.

As is indicated by this table, there are a wide range of steels available all with properties relevant to specific applications. They all, except the Hadfields austenitic steel, offer a high degree of corrosion resistance in most environments with the more highly alloyed steels being

better suited for more specific applications. The mechanical properties of these steels vary considerably across the alloy range.

The mechanical properties are highly dependent on the processing route of the stainless steel, but in annealed AISI 304 and AISI 316 the yield strength is 310 MPa and the tensile strength is 600 MPa and 580 MPa respectively[8]. High nitrogen austenitic stainless steels show a large improvement on the yield and tensile strength of standard austenitic stainless steels and yield strengths in the order of 500 MPa, depending on the nitrogen content and grain size, have been reported[9]. The tensile strength of high nitrogen stainless steels is reported to be in the order of 800 MPa[10]. It is important to consider the strengthening mechanisms operating in these steels, because it is evident that higher strengths can be obtained by alloying with nitrogen and manganese. The mechanisms by which this is accomplished are revealed in section 3.4.

3.2.1. Nitrogen Solubility in Stainless Steels

The most important reason for nitrogen alloyed stainless steels not to have been developed to commercial success more rapidly is that nitrogen has limited solubility in austenitic stainless steel at atmospheric pressure. It has been known since World War II that nitrogen can impart beneficial properties to a stainless steel. During the 1950s there was a scarcity of nickel in the USA and steels were developed in which all, or part, of the nickel was replaced by nitrogen. The most successful steels of this era were the AISI 200 series stainless steel, the composition of which is given in Table 3.2[11].

Alloy	Cr	Mn	Ni	N	C	Mo
AISI 304	18.3	1.2	9.3	-	0.05	-
AISI 316	16.5	1.5	10.3		0.05	2.15
AISI 201	17.0	6.5	5.2	0.25	0.15	-
Hadfields	-	10	-	-	1.2	-

Table 3.2: The composition of a few austenitic steels. This table reveals the high Ni content in the AISI 304 and AISI 316 steels in contrast to the low Ni content in AISI 201.

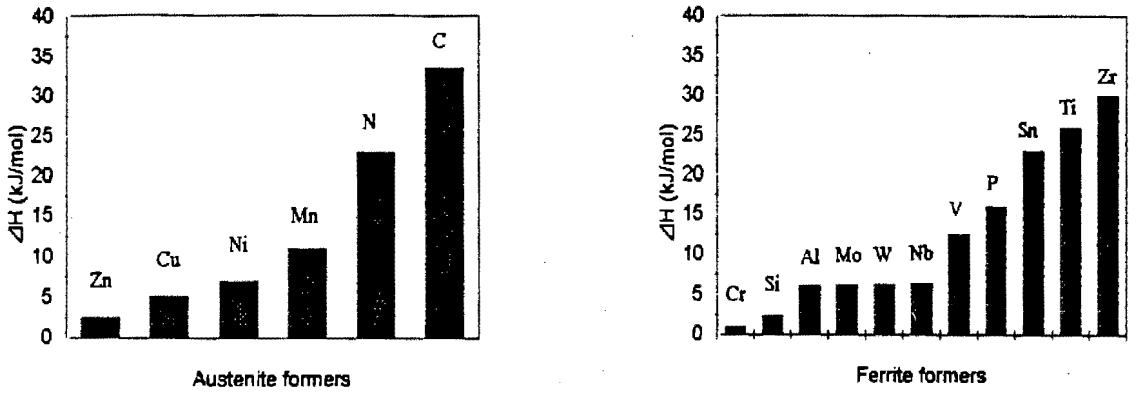

Figure 3.2: The effect of the addition of alloying elements on the austenite and ferrite phase stability. Nitrogen is a strong austenite forming element.

Because of the work carried out in the 1960s the potency of nitrogen as an austenite forming element is well know and documented[12]. Figure 3.2 shows the strength of nitrogen as an austenite forming element, and in particular that it is more than twice as effective as nickel in reducing the enthalpy of austenite. These results can be contrast with the ones obtained from the well known nickel and chromium equivalent equations used to calculate the potency of an element as either an austenite or ferrite former. A recent Ni equivalent equation published by Espy [13] indicates that nitrogen is up to 20 times more effective in stabilising austenite than nickel.

Before being able to produce high nitrogen steels it is necessary to have relevant models available to predict the phase of the stainless steel produced and whether or not nitrogen will remain in solid solution or precipitate out of solution. Much work was conducted in the 1960's on the solubility of nitrogen in iron alloys and on the effect of alloying elements on the solubility of nitrogen [14 15]. It was shown in this work, on Fe-Cr-Ni alloys, that the nitrogen solubility in iron adheres to Sieverts law in that the solubility is proportional to the square root of the N_2 pressure. More recently Rawers and Kikuchi [16] have derived equations to show the effect of manganese and chromium concentrations on the nitrogen solubility. Their results are shown in Figure 3.3, which indicate the theoretically derived solubility of nitrogen as a function of Cr and Mn concentrations when melted at 1650°C and 200 MPa of nitrogen pressure. Their work reveals a deviation from linearity of Sieverts Law with increasing manganese content which indicates that Mn increases the nitrogen solubility. The diagram does not take into account the resulting microstructure and it is certain that a great deal of the nitrogen would be taken up by precipitate formation on cooling. These precipitates will not necessarily be beneficial to the mechanical properties of the steel. The optimisation of the nitrogen concentration needed to form beneficial precipitates will be dealt with in section

3.4.7. Raghavan[17] has found that the addition of Mn is found to destabilise austenite and concluded from this that the role of the Mn is not to stabilise austenite but rather to increase the solubility of nitrogen.

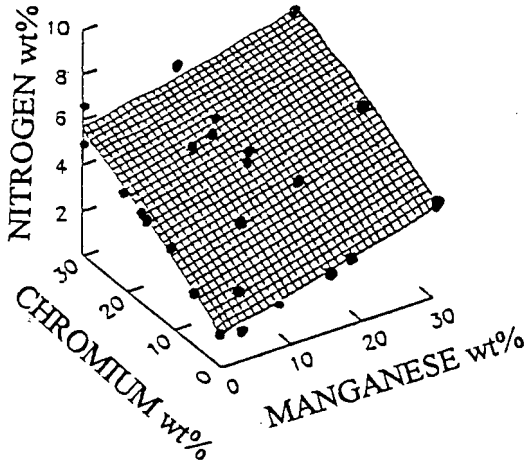

Figure 3.3: The solubility of nitrogen as a function of Cr and Mn. (After ref. 16)

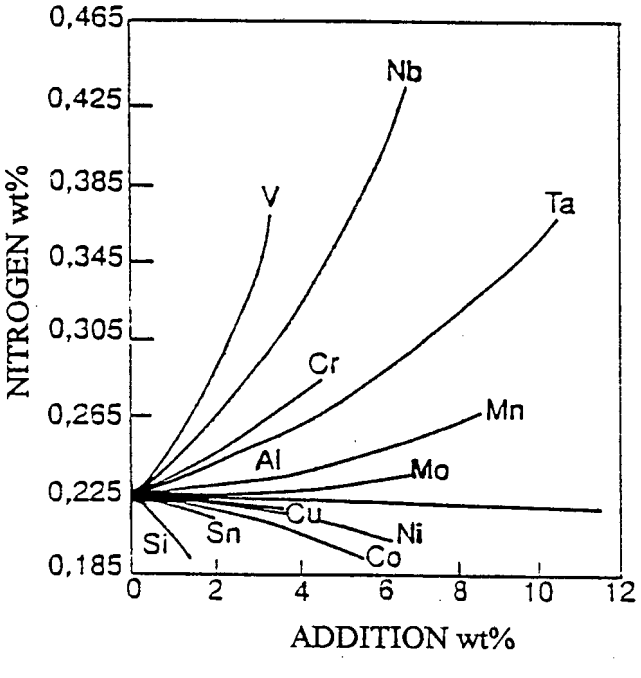

Figure 3.4: The effect of alloying elements on the solubility of nitrogen in a Fe18Cr8Ni alloy at 1600°C and 1 atm. N_2. (from ref. 18)

Other elements, besides manganese, can also be used to increase the solubility of nitrogen and the effect of these alloying elements on the solubility of nitrogen is shown in Figure 3.4.

Once a knowledge of the solubility of nitrogen in austenite was obtained the difficulty was to be able to produce high nitrogen austenitic stainless steel in commercially viable quantities. It was not until the mid 1980's that the technology was available to produce high volumes of this material. The most commonly used method is pressurised electroslag remelting (PESR) in which the alloying is performed at high nitrogen partial pressure and nitrogen is either bubbled through the melt or added as nitrogen rich ferrochrome powder[19]. It is not always possible to get an even nitrogen distribution by this method. An atmospheric pressure alternative to PESR has been developed. In this method the nitrogen concentration and the microstructure can be controlled[20] by careful alloying.

3.3. Mechanical Properties

The mechanical properties of high nitrogen austenitic stainless steels have been researched by many workers[2,9,34]. The vast majority of results have been obtained from steels with a moderate to high Ni content (from 6wt% Ni up to 30wt% Ni) This thesis deals with a nearly nickel free stainless steel but we will consider the results obtained by other workers because they elucidate the effect nitrogen has on the austenite matrix. The reasons for the improvement in the properties of these steels are outlined in section 3.4.

3.3.1. Yield Strength and Ultimate Tensile Strength

At room temperature and with a grain size between 50 μm and 100 μm Uggowitzer *et al* [2] find a five fold improvement in yield strength when the nitrogen content is increased from 0wt% to 0.5wt% in CrNi and CrMn steels. Spiedel[21] *et al* have found similar trends. There have been attempts to describe the strengthening effect of nitrogen by using empirical equations and the two most successful are those by Irvine et. al.[22] and Norström[23]. Varin and Kurzydlowski[24] have conducted tests and verified the accuracy of these equations. The ultimate tensile strength is also increased by cold deformation and this effect is most pronounced in results obtained from cold drawn wires[25].

3.3.2. Work Hardening Rate

A phenomenon of, but not restricted to, face centred cubic metals is that the mechanical properties can be improved by cold working. This means that when plastic flow occurs in the metal it becomes increasingly difficult to create or move dislocations. The fact that dislocations are easily produced implies that the hardening is due to an increase in immobile dislocation density[26]. In this regard Nutting[27] has stated that the work hardening rate depends on the stacking fault energy such that raising the stacking fault energy lowers the work hardening rate. A material with a low stacking fault energy will have a high work hardening rate. The dislocation barriers involved in work hardening are most likely to be the grain boundaries, twin boundaries or areas of transformed material. A measure of the work hardening rate can be obtained by analysing tensile test data. The work hardening exponent n is defined according to Equation 3.1.

$$\sigma = k\varepsilon^{n}$$

Equation 3.1

σ - true stress
ε - true strain
k - material constant
n - work hardening exponent

The work hardening exponent, n, is strain dependent. As the graph of $\ln\sigma$ vs. $\ln\varepsilon$ does not always produce a straight line the slope measured to obtain n has to be measured between set strain values. The value of n can be about 0.2 for aluminium, 0.25 for mild carbon steels and over 0.5 for stainless steels for strains of 0.3[28]. The reason for austenitic stainless steels high work hardening rate is its low SFE. As soon as a dislocation is allowed to cross slip across a dislocation barrier the material is no longer being work hardened. A low stacking fault energy will reduce cross slip and therefore increase the work hardening rate. The SFE will be dealt with in greater detail in section 3.4.5.

3.3.3. Fatigue Resistance

The fatigue resistance is important in our discussion because of its relevance to cavitation erosion. The process of fatigue is described by Suresh[29] in five stages;

(1) the creation of irreversible changes in microstructure and substructural constitution,
(2) nucleation of microscopic defects,
(3) the formation of dominant macroscopic defects,
(4) subcritical growth,
(5) failure or instability.

The form of fatigue crack growth depends on the size of the zone of plastic flow. When the zone of plastic flow at the crack tip is smaller than the grain size deformation is restricted to a single slip system and the fatigue crack advances along the most dominant slip plane, but when the plastic zone is larger than many grain diameters fatigue fracture emerges as a result of simultaneous or alternating slip on 2 different slip systems. Figure 3.5 below shows the process of duplex slip ahead of a fatigue crack[30].

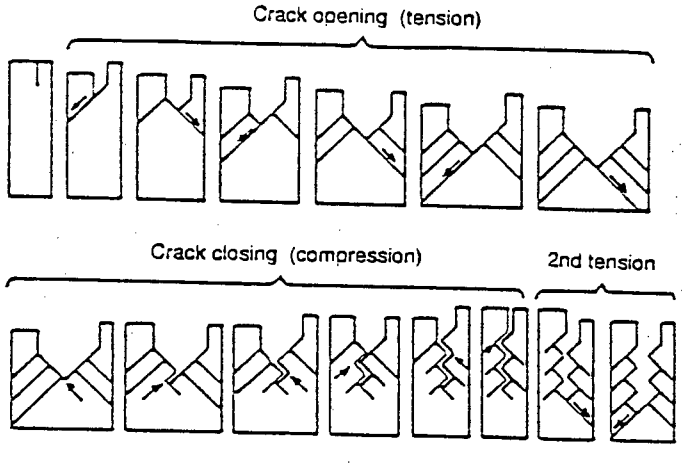

Figure 3.5: The process of fatigue caused by slip.

Returning to high nitrogen steels, Nilsson[31] has shown that a materials ability to undergo planar slip increases its fatigue resistance, whereas cross slip lowers the fatigue resistance. When cross slip is prevented, as in low SFE alloys, the fatigue crack tip growth rate is reduced[32].

3.4. The Strengthening Mechanisms Operating in a High Nitrogen Manganese Austenitic Stainless Steel

3.4.1. Solid Solution Strengthening

Solid solution strengthening involves the addition of various alloying elements either as substitutional alloying elements or interstitial alloying elements. The graph below gives the relative strengths of the different alloying elements. The graph illustrates that the interstitial elements carbon and nitrogen have the greatest solid solution strengthening effect.

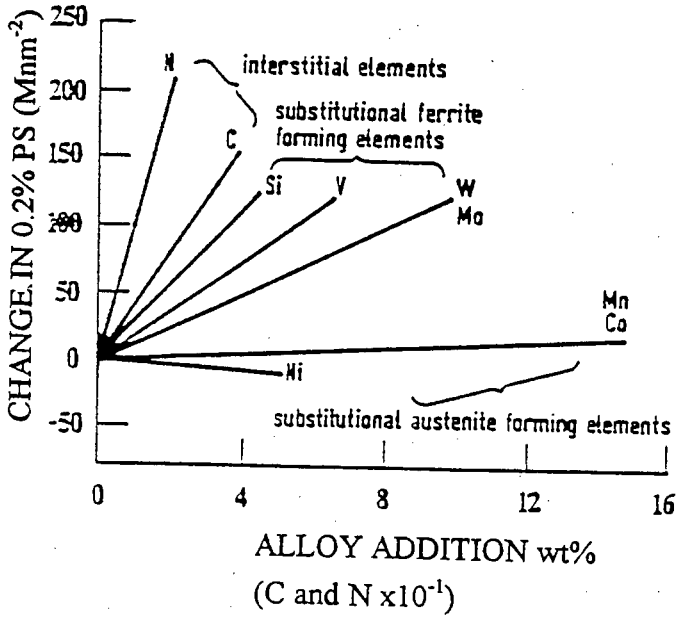

Figure 3.6: Graph of the solid solution strengthening effects of alloying elements in an austenitic stainless steel. (after ref. 18)

Nitrogen and carbon, as interstitial elements, occupy the octahedral voids in the face centred cubic (f.c.c.) austenite lattice. The accommodation of these interstitial atoms in the f.c.c. lattice is found to dilate the lattice. Research[33] performed on Fe-Cr-Ni alloys indicates that the lattice parameter is affected according to Equation 3.2.

$$a = 0.3586 + 0.000854\, x_{C+n}$$

Equation 3.2

a - lattice parameter

x_{C+N} - atomic concentrations of carbon and nitrogen

The extent to which the lattice is dilated depends on the size of the interstitial atom with respect to the volume available in the lattice and on the attraction the interstitial elements have for the matrix and substitutional alloying elements. For this reason the alloy composition will affect the extent to which lattice dilation occurs. It is also shown[33] that nitrogen, although being smaller than carbon, has a greater dilatation effect on the f.c.c. matrix. This can be ascribed to the Fe-C bonds being stronger than the Fe-N bonds[33]. The dilatation of the matrix is important because it creates strain fields which inhibit the movement of dislocations.

In a theoretical calculation by Uggowitzer *et al*[9] they argue that the shear strength from a random array of atoms interacting with a moving dislocation can be calculated using Equation 3.3.

$$\tau . = \left(C_N\right)^{\frac{1}{2}} \left(f_0\right)^{\frac{3}{2}}$$

Equation 3.3

C_N - concentration of solute nitrogen atoms

f_0 - measure of the interacting force between dislocations and solute atoms

In Equation 3.3 (f_0) indicates how strongly a nitrogen atom acts as an obstacle to dislocation movement, and is a sum of the effect of lattice distortion, δ, due to the misfit of the solute atoms and the modulus of elasticity change, η, with changing solute atom concentration. The effect of these parameters on (f_0) is described by Equation 3.4.

$$f_0^2 = \delta^2 + \beta^2 \eta^2$$

Equation 3.4

When measured indirectly from X-ray measurements (f_0) is found to be 0.2 for nitrogen in a CrMn steels which makes it an obstacle force to dislocations ten times stronger than typical values for substitutional atoms. These formulae can therefore explain some of the strengthening effects ascribed to nitrogen.

The increase in athermal flow stress of a nitrogen rich austenitic steel with increasing nitrogen content has been attributed[34] to the short range ordering between N in solid solution and Cr. The planar slip prevalent in high nitrogen steels implies that nitrogen clustering is not responsible for the increase in athermal flow stress. An increase in the thermal component of the flow stress with an increase in nitrogen content is also noted by Byrnes[34] and ascribed to the modulus interactions between lattice disturbances in the immediate vicinity of the nitrogen atoms and slip dislocations.

3.4.2. Strain Age Hardening

Strain ageing works on the premise that interstitial atoms, when sufficiently motivated, will migrate to dislocations in the material and thereby pin these dislocations. When the strain fields caused by interstitial atoms and the strain field from a dislocation interact there is a net reduction in the total strain energy. A suitable driving force such as cold work followed by a heat treatment will result in interstitial concentrations or atmospheres in the vicinity of the dislocations. These atmospheres are sometimes referred to as Suzuki atmospheres. The dislocations are consequently locked in position by the interstitial atoms and the stress required to move the dislocations is substantially raised.

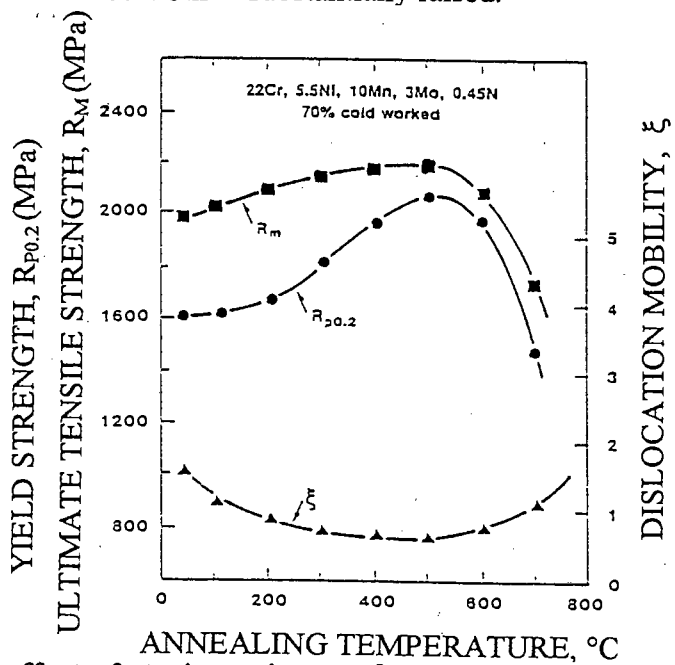

Figure 3.7: The effect of strain ageing on the properties of a nitrogen alloyed stainless steel. (after ref. 35)

In a nitrogen alloyed steel strain age hardening can occur at nitrogen levels as low as 0.001-0.002 wt%N. Strain ageing is therefore an option to be considered when seeking to improve the strength of a steel. Nitrogen is more effective at strain ageing than carbon due to its greater residual solubility near room temperature[1]. Figure 3.7 shows the effect of a strain ageing heat treatment on the properties of a nitrogen alloyed stainless steel. The term ζ reflects the mobility of dislocations. It can be seen from the graph that there is a decrease in strength at ageing temperatures above 600°C. This is because at these temperatures the nitrogen dissolves out of solution, in the form of precipitates, and is no longer available to pin the dislocations. The graph also indicates that the highest strength is obtained at about 500°C for this particular alloy. We can expect the alloy composition to have an effect on the temperature at which peak hardness is reached. The amount of cold work accommodated by the material prior to the heat treatment will affect both the speed and the amount of nitrogen migration, and will consequently influence the properties of the material.

3.4.3. Grain Boundary Hardening

The yield strength of nitrogen alloyed austenitic stainless steels has been found to behave according to the Hall - Petch relationship, as shown in Equation 3.5[9] and Figure 3.8, with the nitrogen content affecting the value of k_y, the hardening coefficient. However, Varin has found that for low nitrogen concentrations, between 0.065wt%N and 0.013wt%N, k_y is independent of nitrogen concentration. Norström[23] and Degallaix[36] attribute the change in k_y to an increase in the twinning density. The twinning density increases because of the reduction of stacking fault energy in high nitrogen alloys[9]. Planar slip is expected to increase the grain boundary efficiency as dislocation obstacles. The effect of nitrogen content on k_y is illustrated in Figure 3.8.

$$\sigma_{0.2} = \sigma_y + k_y D^{\frac{-1}{2}}$$

Equation 3.5

$\sigma_{0.2}$ - 0.2% proof stress
σ_y - flow stress for a very large grain
k_y - grain size hardening effect
D - grain size

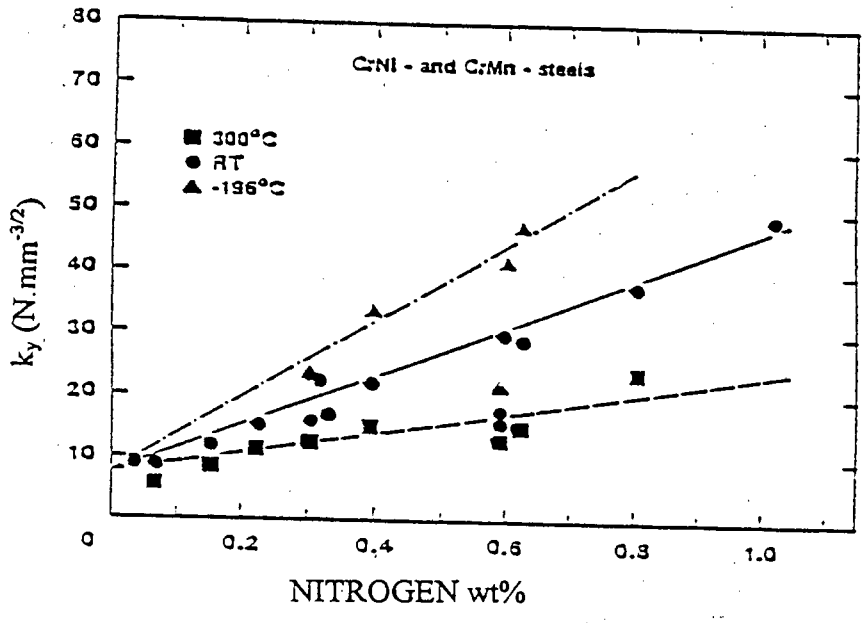

Figure 3.8: The effect of nitrogen and temperature on the Hall-Petch coefficient.

At higher nitrogen contents the grain size hardening effect increases. This is revealed in Figure 3.9 where Uggowitzer *et al* [9] show the effect of both the grain size and the nitrogen content on the yield strength of a range of high nitrogen manganese stainless steels. Norström[23] has demonstrated that the strengthening effect attributed to nitrogen consists of two parts. The one part is grain size dependent and the other grain size independent according to Equation 3.6. The factor [7+(78wt%N)] is used to replace k_y in Equation 3.6 and exhibits the strong dependence of k_y on nitrogen concentration.

$$\sigma_{0.2} = 127.6 + 309.9(wt\%N)^{\frac{1}{2}} + [7 + 78(wt\%N)]D^{\frac{-1}{2}}$$

Equation 3.6

The symbols used in Equation 3.6 are the same as those used in Equation 3.5.

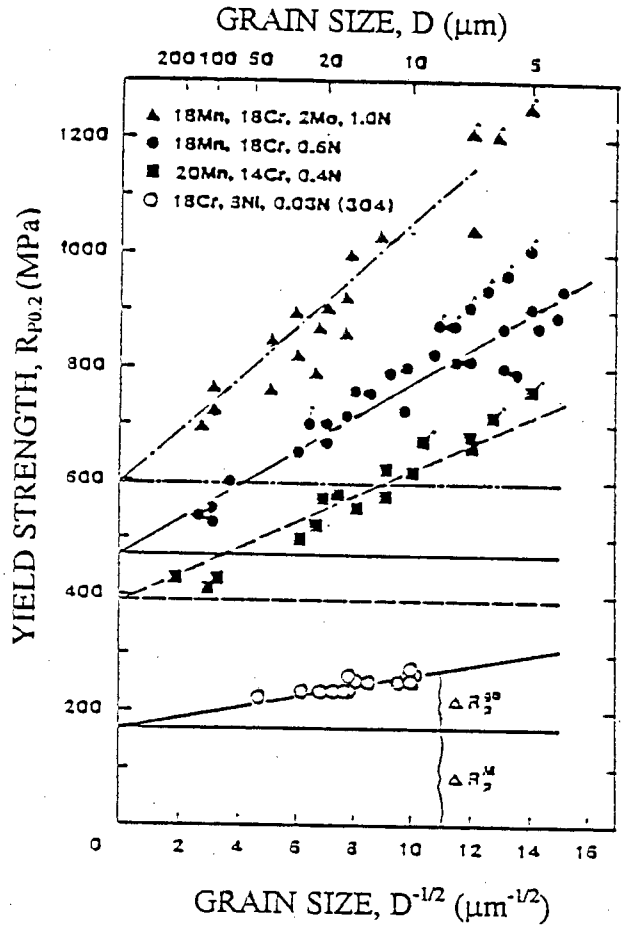

Figure 3.9: The effect of grain size on the yield strength of a high nitrogen steel compared to a low nitrogen steel. (After ref. 9)

3.4.4. Deformation Strengthening / Cold Work

An effective way to increase the yield strength of an austenitic stainless steel is by cold work; however, the cold work could result in a phase change which is deleterious to the properties of the steel. The stress induced phase change from austenite to martensite makes the steel brittle, more prone to stress corrosion, and results in the loss of non-magnetic properties. The martensitic transformation does not occur in the stable high nitrogen stainless steels. The effect of cold work on yield strength is shown in Figure 3.10. It is also clear from this graph that the increase in nitrogen content causes the effect of cold work to become more pronounced, the reason for this is that dynamic recovery is prevented from occurring. The most marked increase in U.T.S. in steels is obtained by wire drawing[37].

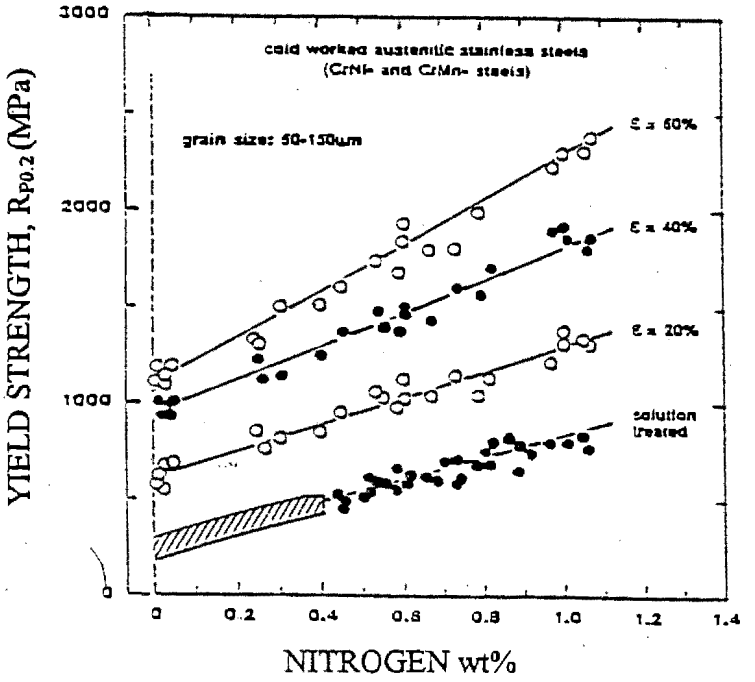

Figure 3.10: The effect of cold work and nitrogen content on the yield strength. (After ref. 9)

3.4.5. Stacking fault energy

The addition of nitrogen to stainless steel is known to reduce the stacking fault energy (SFE). This was shown by Stoltz and Vandersande[38] for a Fe-21Cr-6Ni-9Mn alloy. They concluded that nitrogen only lowers the SFE until 0.25 wt% after which increased additions of nitrogen no longer have any effect on the SFE. In contrast to this Fujikura[39] shows that the SFE continues to decrease with the addition of nitrogen in access of 0.25wt%. The most important consequence of a reduction in SFE is that it causes partial dislocations to be widely separated. This wide partial separation restricts cross slip because the partials first have to rejoin to a single dislocation before cross slip can occur. Planar dislocation movement is therefore encouraged, leading to the formation of low energy dislocation arrays. Müllner *et al*[40] observed two deformation mechanisms in high nitrogen stainless steels. He found a planar glide deformation mechanism to be operating at lower strains and a twinning deformation mechanism to be operating at higher strains. Subsequent to that he concludes that as the nitrogen content is increased form 0.04wt% to 0.53wt% the planarity of glide becomes sharper, the structures become finer and the transition from one deformation mode to the next are shifted to lower strains and higher stresses. A reduction in SFE (i.e. an increase in the nitrogen content) therefore causes the dislocation structure to change from cellular to planar.

The reduction in SFE has important consequences on the mechanical properties, particularly the work hardening rate, of the steel. These consequences are referred to in the relevant sections.

3.4.6. M_{d30} Temperature

If an austenitic stainless steel is metastable it can undergo a strain induced phase transformation from austenite to ferrite. The ease with which this transformation proceeds is dependent on the composition of the alloy. An alloy with high concentrations of austenite forming elements would be reluctant to transform to martensite. One of the methods used to predict the transformability of an austenitic alloy is by using the M_{d30} temperature. This temperature corresponds to the temperature at which 50% of the alloy has transformed to martensite after 30% true strain[41].

It is possible to calculate the M_{d30} temperatures using empirical relations. For the purposes of this thesis the M_{d30} temperatures of the austenitic alloys are calculated using Equation 3.7.

$$M_{d30}\ (°C) = 413 - 462(C+N) - 9.2Si - 8.1Mn - 13.7Cr - 9.5Ni - 18.5\ Mo$$

Equation 3.7[42]

3.4.7. Precipitation Hardening

The alloying of nitrogen in stainless steel with strong nitride forming elements (Ti, Nb, V) can result in the formation, after a suitable heat treatment, of a fine dispersion of nitride precipitates. These precipitates are most likely to form on high energy sites such as dislocations, stacking faults or grain boundaries. For the precipitate to be effective in improving the mechanical properties they have to be small and homogeneously distributed. The optimum size and distribution of precipitates are usually found after a specific heat treatment. A form of precipitation which is in competition to the precipitation discussed above is cellular precipitation. Nitrogen rich stainless steels are found to be prone to cellular precipitation[43 44]. This precipitation is similar to the formation of pearlite, in a C steel, in that there is lamella growth of Cr_2N and transformed austenite matrix from the grain boundaries.

This cellular precipitation is reported by Presser and Silcock[45] and proceeds after precipitation from grain boundaries.

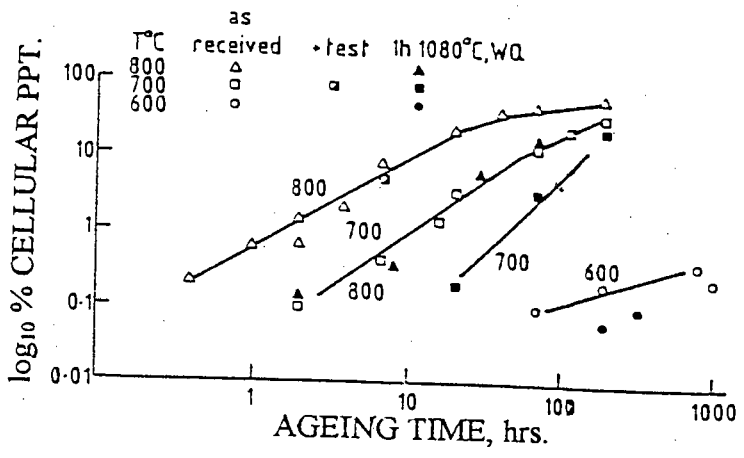

Figure 3.11 Volume fraction of cellular precipitate in an 18Mn-18Cr alloy. [After ref. 45]

Cellular precipitation is visible using optical microscopy but can be clearly identified by the lamella structure in the TEM. The presence of the lamella precipitate can be confirmed by checking the orientation relationship between the Cr_2N and the austenite matrix.

It is shown by Briant[46] that nitrogen segregates to grain boundaries at 600°C, 650°C and 700°C. Other precipitation reactions have been noted to occur in nitrogen rich austenitic stainless steels. These studies have been done predominantly on steels with high nickel contents. Karlson[47] has observed MX (where M is the metal and X either C or N) precipitates of varying stoicheometry and morphology. Ritter[48] has observed Z phase and σ phase precipitation in Nitronic™ stainless steels. Jargelious-Peterson[49] noted laves, T, Π and E phase in a highly alloyed steel. These are intermetallic phases which have complex stochiometry and composition . These phases are not studied in this thesis. None of the workers investigated the mechanical properties or the effect of the precipitates on the corrosion resistance of these alloys.

There have been formulae formulated which attempt to predict the precipitates which may form in a steel. The most interesting is the M_d concept which uses the average energy level of the d-electron orbital of the alloying transition metal to calculate the phase stability or the probability of a particular phase or precipitate forming[50].

3.5. Corrosion Resistance

Although forming a small part of this thesis it is noteworthy to comment on the corrosion resistance of high nitrogen steels. The resistance to corrosion is highly dependent on the exact alloy composition and the type of corrosion. With respect to sensitisation, or microstructural corrosion, it is argued that nitrogen rapidly migrates to the grain boundaries and bonds with Cr to form Cr_2N This results in less Cr being removed from the grain boundaries than if C was bonding with Cr to form $Cr_{23}C_6$. Barbet[51] shows that in an AISI 304 alloy sensitisation is retard with nitrogen contents of less than 0.16 wt% N, but concentrations of 0.16 to 0.25 wt%N promote sensitisation. This change is ascribed to the two different modes of precipitation acting in the two different nitrogen concentration regimes. For low nitrogen concentrations most precipitation occurs on the grain boundaries. But for higher concentrations there is discontinuous nitrogen precipitation (cellular precipitation). It is concluded from this that if cellular precipitation is not allowed to occur, by suitable alloying, then high nitrogen contents would be beneficial to the sensitisation resistance of the steel.

With respect to the effect of nitrogen on the passivity of the steel, nitrogen was found not to have a significant influence on the response of the material to anodic polarisation in 0.5M H_2SO_4 electrolyte[52]. When considering pitting Palit[53] found that nitrogen inhibits stable pit formation either by its effect on the dissolution kinetics or its effect on the repassivation process in the pit, or a combination of these two influences. Llewellyn[11] gives Equation 3.8 to describe a materials tendency to pit, and as shown in the equation nitrogen improves pitting resistance. A low pitting index indicates that an alloy is prone to pitting.

$$\text{pitting index} = (Cr+3Mo+16N), \text{wt\%}$$

Equation 3.8

Oldfield[54] has shown that an increase in the nitrogen content increases a stainless steels resistance to crevice corrosion initiation. This indicates that the steel has good potential in sea water applications.

3.6. Abrasion

Abrasion is a specific category of wear, typically when a hard asperity is in contact with a softer material. The hard particles then cause a loss of material by various modes which depend on the mechanisms operating in the wear system. The wear resistance of a material is not a materials property but rather a property of the wear system and the system is influenced by the size, shape and aspect ratio of the abrasive particles, the mechanical properties of the material and abrasive and the velocity and load applied during wear. There are four commonly observed wear mechanisms, or microevents, by which wear takes place[55]:

(1) shearing at junctions
(2) microcutting
(3) impact
(4) fatigue

These mechanisms are common to all materials, and the relative contribution of each process depends on the material, the abrasive and the system in which it is operating[56]. Krushov and Babichev[57] were the first to point out that there were two possible ways in which an abrasive particle could make contact with the wearing surface. These two models encompass both the brittle and ductile modes of failure.

(1) Formation of plastically deformed groves. (ploughing)
(2) Separation of particles in the form of microchips. (cutting)

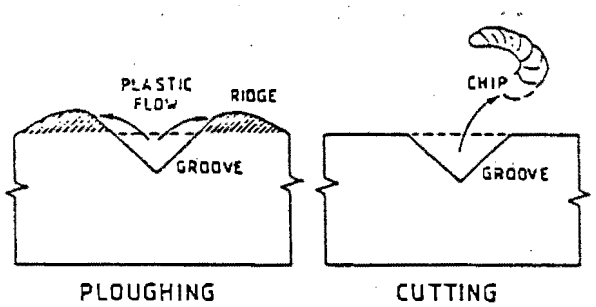

Figure 3.12: Schematic diagram showing the formation of a grove during wear by (1) ploughing and (2) cutting.

Most metals wear by a combination of the two mechanisms. Although first proposed in the 1950s the models are still relevant when considering wear modes. In Figure 3.12 the shaded area represents the region that has been plastically deformed and this is the work hardened material that is still attached to the bulk. The next abrasive strike, which results in strain above the amount that the material can accommodate, will result in loss of material from the surface. This is described by Ludema[58] in terms of material loss by low cycle fatigue. Suh[59] ascribes the wear to delamination and Zum Gahr[60] to microcracking.

Thus when designing a material or considering a material for wear resistant applications careful account has to be made of the system in which the material is expected to operate.
Despite this heavy dependence on the system, various attempts have been made to correlate materials properties with wear resistance. The first, and most obvious, correlation was made between wear resistance and hardness[61]. Barker[62] has taken a number of wear resistance results and plotted them against hardness (Figure 3.13) and, to a certain extent, these results show that the wear resistance can be correlated to the hardness for different classes of materials, but that there is virtually no use of hardness when comparing the same class of material.

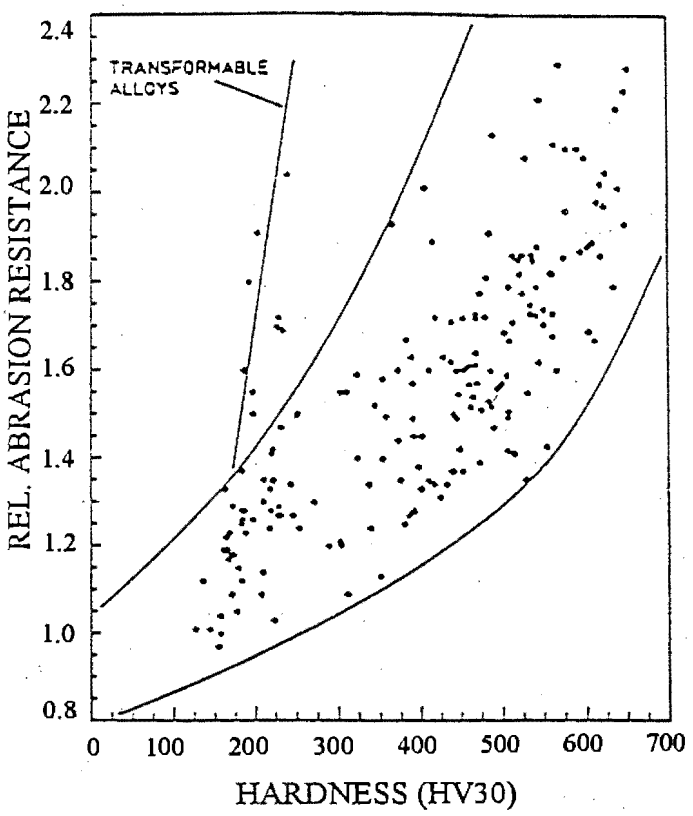

Figure 3.13: Combined plot of all materials tested at the Department of Materials Engineering U.C.T to September 1985. (After ref. 62)

The shortcoming of using hardness to determine the wear rate is especially apparent when the alloy under consideration contains impurities, solutes, precipitates or more complicated microstructures. Rigney and Glasser[63] overcame these limitations to some extent by plotting wear rates versus hardness by considering three different material loss mechanisms as shown in Figure 3.14.

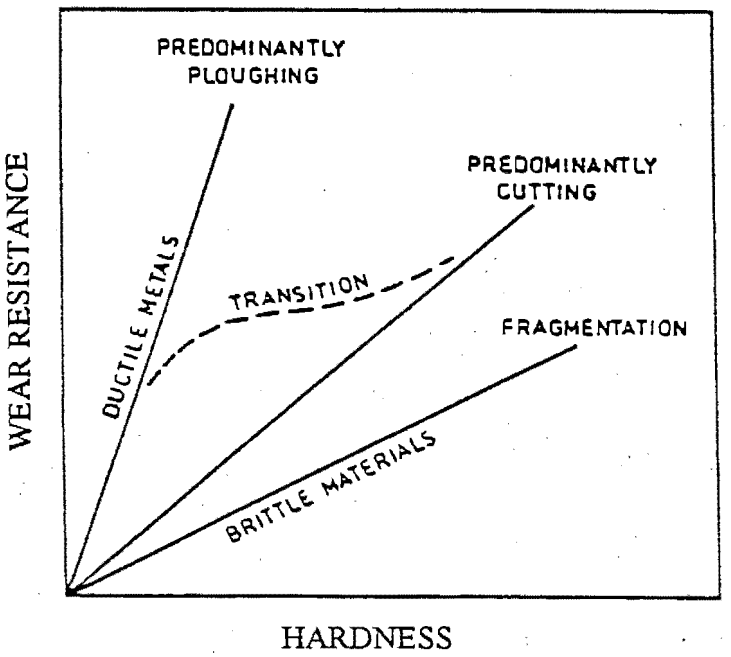

Figure 3.14: A relationship between hardness and wear rate can be predicted when considering the various modes of wear.

The abrasion resistance has been coupled to other materials properties and some of these are discussed below.

It has been argued that the surface hardness of the abraded material is sufficient to describe the wear resistance of a material[64]. Contrary to this Garrison and Garriga[65] argue that a knowledge of the surface hardness is insufficient to predict abrasion resistance.

Another yardstick to consider when judging a materials abrasion resistance is its work hardening rate (WHR). The work hardening rate of a material has been defined in section 3.3.2. Ball[66] extols the importance of WHR in the wear process by making reference to the stress strain curves of a material and the cumulative effect on the plastic deformation of a material caused by successive abrasive strikes. He also alludes to the importance of absorbing energy by plastic deformation from the strike of an abrasive particle. The WHR has been used by Allen *et al* [67] to compare the potential abrasion resistance of a class of materials, i.e.

austenitic stainless steels. Moore *et al* [68] argue that since the wear rate depends on the ultimate tensile strength, which consequently depends on the maximum dislocation density, wear is related to the WHR. They continue this line by saying that work hardening and dislocation multiplication would have to continue further if fracture was to be prevented. Because of its effect on the mechanical properties work has also been performed on the influence of prior cold work on the wear rate. Avery[69] has found that there is no benefit to be derived from prior cold work while Allen *et al* [67] have found that cold work was detrimental to an austenitic stainless steels wear resistance.

Returning to the field of study of this thesis, stainless steels, and in particular austenitic stainless steels, have been well studied with regard to their abrasion resistance. Allen *et al*[67]. show that out of a range of stainless steels, austenitics have the best abrasion resistance. They explain this in terms of the high strains that the material can accommodate before there is material loss. This accommodation of strain, in a metastable austenite, is due to the transformation of the f.c.c. austenitic to b.c.t. martensite.

Research aimed specifically at the abrasion resistance of high nitrogen steel has been conducted by Hawk *et al*[70]. For the alloys under investigation they have found that nitrogen has a beneficial effect on the abrasive wear prior to heat treatment and precipitate formation and that precipitate formation results in a further improvement in the abrasive wear resistance. Campillo Illanes *et al*[71] have shown that the running in wear of nitrogen stainless steels is high, but that the steady state wear rate decreases with increasing nitrogen content. Finally Wei *et al*[72] have shown that in a nitrogen implanted AISI 304 stainless steel the wear resistance is improved by nitride formation.

3.7. Abrasion-Corrosion

Many industrial applications of materials involve the simultaneous exposure of a material to an abrasive *and* corrosive environment. Work in the field of abrasion-corrosion is relatively scarce[73]. The reason for this is the difficulty in devising a rig which can give the researcher valid information such as the relative contribution of the different wear processes to the total material loss caused by wear.

Electrochemical techniques have been used to determine the effect of abrasion on the corrosion of steel pipes through which a variety of slurries are pumped[74]. The adverse influence of the particles in solution were discussed in terms of the destruction of the passivating layer.

El-Kouss *et al*[75] used a tumble mill in which the ball specimens were placed together with an abrasive sand and sea water mixture. The results from this test lead them to the conclusion that the wear resistance of steels in wet sand is predominantly determined by their chemical composition and microstructure rather than their normal corrosion resistance. The wear component is thus the dominant contributing factor in material loss. Dunn[76], using a grinding ball mill in wet conditions, points out that wear is a combination of abrasive, corrosive and impact mechanisms operating together. It was indicated that abrasion and corrosion operating concurrently increased the net combined effects beyond the addition of the loss rate attributed to each separate material loss action. Noël[77] showed that an abraded surface has a higher corrosion rate than a smooth surface. He proposes that abrasion would create a highly deformed and active surface of which the ridges are anodic and thus prone to corrosion. In this regard he noted that the more frequent is the intermittent abrasion, in the cyclic abrasion-corrosion test, the greater would be the volume loss due to corrosion.

3.8. Cavitation

3.8.1. Mechanisms of Cavitation

Cavitation is often defined as the growth and collapse of vapour cavities or bubbles due to local pressure fluctuations in a liquid[78]. When there is a local decrease in pressure in a liquid, below the vapour pressure of the liquid, bubbles will form in that area of the liquid. When the pressure rises the bubble will collapse causing a stress wave or jet of liquid which can cause plastic deformation at the solid surface. This process is shown in Figure 3.15. Cavitation occurs in virtually all hydrodynamic systems, e.g. pumps, marine propellers, hydraulic turbines and hydrofoils. The collapsing bubble and resulting pressure wave and water jet can exert stress pulses in the magnitude of a few hundred MPa to a few thousand MPa[78]. The damage causing component is debated to be either the shock wave generated by the symmetrical collapse of the cavity, as originally proposed by Rayleigh[79] and developed by others, or liquid jet impingement, first suggested by Kornfeld and Suvorov[80]. The damage is most likely to be caused by a synergistic effect of the two, with the relative contribution being dependent on the distance of the bubble from the surface of the material and the radius of the bubble[78].

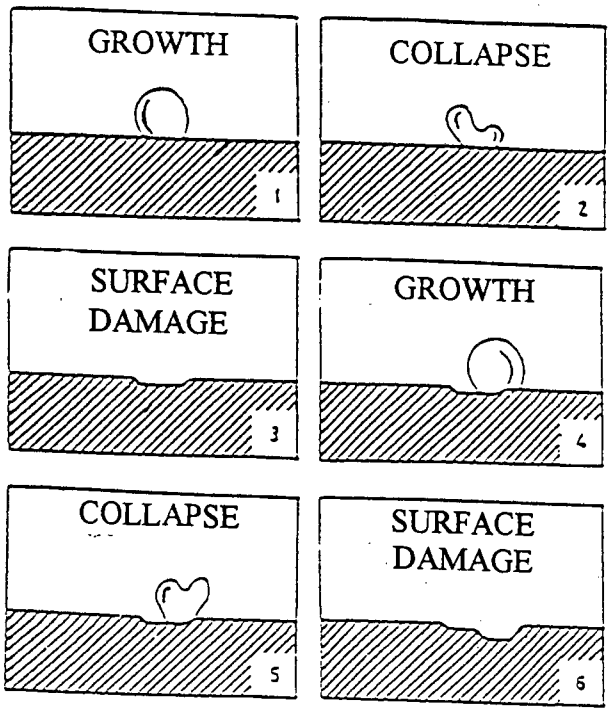

Figure 3.15: A schematic representation of the process of cavitation. Cyclic variation in the water pressure near a solid surface cause the nucleation, growth and asymmetrical collapse of bubbles.

3.8.2. Material Considerations

As with abrasion there is a continual quest to try and relate the rate of cavitation to a material property. Some of the work done in this area is shown in this section.

1. *Hardness.* Similar materials usually show an increase in cavitation resistance with increase in hardness[78]. This has been shown by many researchers but contradicted by Vaidya and Preece[81] who found an increase in cavitation erosion resistance with decreasing hardness in aluminium.

2. *Strain energy.* This value represents the area under the materials stress-strain curve and depicts the materials ability to absorb energy. Good correlation with cavitation was found by some workers [82 83] while others [84 85 86] found bad or no correlation.

3. *Fatigue limit.* Karami[78] argues that cavitation erosion is caused by a form of micro-fatigue failure and to this extent Richman[87] has shown that the cavitation erosion resistance is related to the fatigue strength. They have applied their theory successfully to a number of metals with different hardnesses. Ashmed[88], in his analysis of the cavitation erosion of a AISI 304 stainless steel, has shown that it fails by fatigue and fatigue resistance is therefore a good indication of cavitation resistance.

4. *Work hardening rate, SFE and phase transformations.* Richman[87] has shown that there is a direct correlation between cavitation resistance and SFE. Karami[78] proposes that Stellite 6B has good cavitation resistance due to its ability to transform to strain induced martensite. This is contradicted by Woodford[89] who suggests that the increase in resistance is due to SFE and the material's planar slip mode of deformation which delays the development of localised stresses required to initiate fracture. Heathcock[90] argues that austenitic stainless steels have good cavitation resistance because the work hardening rate causes changes in the mechanical properties due to mechanical twinning and precipitation of ε h.c.p. phases. Vaidya[81] does not observe any transformation in h.c.p. cobalt but ascribes its strength to mechanical twinning which affects strain energy accumulation and encourages strain relaxation.

Heathcock[91] reports that martensitic steels have the highest cavitation erosion resistance followed by austenitic steels and then lastly ferritic steels. The martensitic steels owe their cavitation erosion resistance to the homogeneous distribution of deformation and shorter distances dislocations are able to move through the fine martensite platelets. Amongst the

austenitic steels Hadfields manganese steel shows the highest erosion resistance followed by AISI 304 and AISI 316. Hadfields has a high cavitation resistance due to its low SFE and its high WHR, but shows little sign of martensitic transformation. AISI 304 performs better under cavitation than AISI 316 because of its higher inclination to transform from austenite to martensite. Zilla and Hogardy,[92] studying a metastable Cr-Mn austenitic steel, suggest that its strength lies in partial transformation to martensite at the surface and the base metal remaining austenitic to absorb the strain. A complete transformation to martensite is expected to reduce the cavitation resistance as there would be less austenitic base metal available to accommodate the cavitation induced strain.

4. EXPERIMENTAL METHODS

4.1 Materials

The initial range of materials investigated in this study was quite wide, encompassing a number of alloys with varying N, Mn, Cr, and Cu contents. These alloys were laboratory produced and were of bad and inhomogeneous properties. This inhomogeneity was most apparent in the microstructure and was also revealed in the preliminary wear test results. These experimental steels were excluded from the study due to their bad and unpredictable characteristics. The composition of the experimental steel that was finally used in the study is given in Table 4.1. and is designated 852. This steel, which had good homogeneous properties, was produced as a 50t heat and a section of this material was used in the tests. The steel falls into the category of a high nitrogen steel because of its nitrogen content of 0.63wt% N. The microstructure of this steel is shown in Figure 5.5.

Alloy	Cr	Mn	N	Ni	Mo	V	C	P	Si	S
852	19	10	0.63	0.83	0.16	-	0.03	-	0.03	-
811 (ppt.)	20	14	0.65	2.4	0.7	0.4	-	-	-	-
304	18.3	1.2	-	9.3	-	-	0.05	0.02	0.02	-
316	16.5	1.5	-	10.3	2.15	-	0.05	0.02	0.5	-
Hadfields	-	10	-	-	-	-	1.2	-	-	-
Mild Steel	-	0.7	-	-	-	-	0.2	0.05	0.3	0.05

Table 4.1: The composition of the alloys used in this thesis (in wt %).

The other experimental steel studied was a vanadium micro-alloyed stainless steel which had precipitation hardening potential. The precipitation behaviour of the steel was studied and this was related to the tribology of the steel. This steel is referred to as the vanadium micro-alloyed steel and is given the designation 811. The composition of this alloy is revealed in

Table 4.1. There are a number of precipitate reactions which could take place. These are the formation of vanadium nitrides, chromium nitrides and molybdenum nitrides. The formation of these nitrides has been discussed in the literature review section.

4.2. Cold Work

In addition to 852 being tested in the annealed condition tests were also conducted on cold worked material. The austenitic stainless steel alloy, 852, was cold to 16%, 30%, 48% and 66% cold deformation.

4.3. Heat Treatment

Each of the deformed alloys mentioned above were placed in a vacuum furnace at 400°C for 2 hours. This treatment was used to promote strain age hardening.
The vanadium micro-alloyed steel was first solution treated at 1250°C for 12 hours. Thereafter the heat treatments were performed at 700°C and 900°C for 0.5 hrs, 1 hr, 2 hrs, 4 hrs and 8 hrs respectively.

All heat treatments were conducted in an argon atmosphere. The samples were placed in a vacuum furnace and the furnace was pumped down to vacuum and purged with argon. The heat treatment cycle was commenced by heating the specimens at 900°C per hour until the desired temperature was achieved. The samples were oil quenched after the correct ageing time. This heat treatment procedure was followed when preparing all of the specimen.

4.4. Metallography

4.4.1. Optical microscopy

Light microscopy was performed in either the conventional bright field mode or using Nomarski interference contrast. In preparation for the light microscopy the specimens were ground and final mechanical polishing was accomplished using 0.25 μm diamond paste. The specimens were then prepared in a 10% oxalic acid in distilled water solution. The electrolytic etch was conducted at 10V for 30 seconds.

4.4.2. Scanning electron microscopy

All specimens were thoroughly cleaned in alcohol and arklone before being investigated in a Cambridge S200 scanning electron microscope (SEM) to which a Tracor EDAX system was attached for semi-quantitative element analysis. Operating conditions were set at an accelerating voltage of 20 kV and all images were acquired using the secondary electron detector.

4.4.3. Transmission electron microscopy

Thin foils for use in the transmission electron microscope were made-up by first grinding the material to 400 μm thickness which is the correct thickness for punching. The thin discs (3 mm in diameter) were then ground down to 100 μm thickness. They were then jet polished in a Struers Tenupol to perforation at -15°C, 35V and a moderate (3) flow rate. The polishing solution used was a 5% perchloric acid in ethanol mixture.

A JEOL 200CX microscope operating at 200 kV was used to study the thin foils. A double tilt specimen holder was used to obtain the correct imaging conditions. Both bright and dark field imaging techniques were used to study stacking faults, twinning, dislocations and precipitation.

4.5 Tensile Tests

The tensile tests were performed on the alloy 852 at room temperature. Three specimens were tested to ensure reproducibility. A computer interfaced Zwick 1484 universal testing machine with an extensometer arm extension was used for all the tests. The tests were performed at an initial strain rate of $1x10^{-3}s^{-1}$. The specimen geometry used is shown in Figure 4.1.

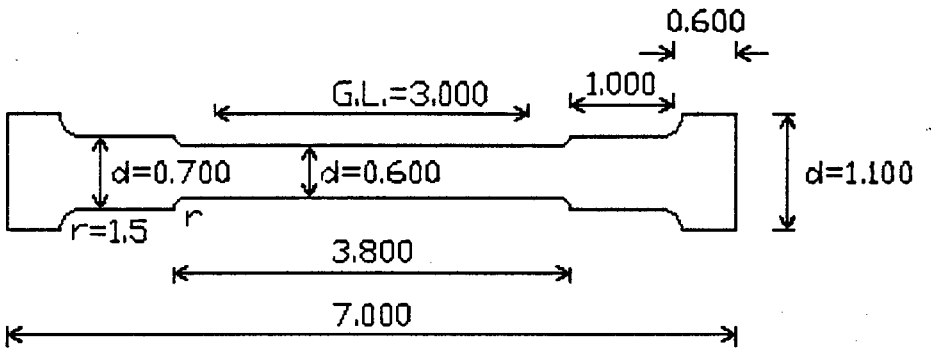

Figure 4.1: The tensile test specimen geometry. G.L. is the gauge length, d the diameter and r the radius of curvature. All the measurements are in millimetres.

The resulting load versus extension data obtained from the tensile testing machine was converted to true stress versus true strain data using Quatro Pro spreadsheet facilities. The graphs of the engineering stress versus engineering strain curves can then be drawn using this data. The work hardening rate was obtained by plotting the slope of the true stress vs. true strain curve against true strain.

4.6 Hardness and Microhardness Measurements

Macro hardness tests were performed with a Vickers diamond pyramid indenter, with a load of 30 kgf on a polished surface. At least five hardness indentations were made and an average taken.

Microhardness was measured using a Shimadzu microhardness tester. A Vickers diamond pyramid indenter with 0.2 kgf, applied for 10 sec., was used. At least ten indentations were performed and from this an average of the microhardness was calculated.

4.7. X-Ray Diffraction (XRD)

Although the high nitrogen stainless steel was expected to be stable from the results of relevant calculation, XRD was used to assess whether or not any phase transformation had taken place during cold deformation or cavitation erosion.

4.7.1. Preparation, Instrumentation and Analysis

The cold worked specimens were polished on 1 μm diamond paste before being tested. The cavitation eroded specimens were placed directly into the XRD after being cavitated for 12 hours. The Data was collected using a computer interfaced Philips XRD instrument. A molybdenum (Mo) x-ray tube was used because of its greater depth of penetration compared to the penetration depth of copper X-rays. Divergence and scatter slits of 1 mm width were inserted. A zirconium β-filter was inserted between the tube and the specimen to ensure that only K_α radiation reached the specimen. A graphite monochromator was used to record the data with increased resolution of the K_α doublet. The voltage and current were set at 44 kV and 34 mA respectively. A count time of 10 sec and a step interval of 0.1° (2θ) was used. The samples were then scanned over a 2θ range of 30°, from 18° to 48°. The samples were mounted in a specially produced specimen holder which could accommodate the 10 mm x 10 mm specimen geometry.

The test was not performed to calculate the exact quantity of transformed material but rather to determine whether or not there was any transformation taking place. The peaks of the spectra generated were compared to the values in Table 4.2 to establish whether any transformation had taken place.

Reflections	Bragg Angle (2θ)
200 γ (fcc)	11.39
220 γ (fcc)	16.32
311 γ (fcc)	19.21
200 α' (bct)	14.35
211 α' (bct)	17.73
310 α' (bct)	22.98
$10\bar{1}1$ ε (hcp)	10.65
$10\bar{1}2$ ε (hcp)	13.65

Table 4.2: Bragg angles for the reflections from different planes of fcc, bct and hcp phases in stainless steel using MoKα radiation.

4.8. The Abrasion Test

The abrasion tests were of the pin-on-abrasive type and were performed on a converted Rockwell belt sander which is shown in Figure 4.2.

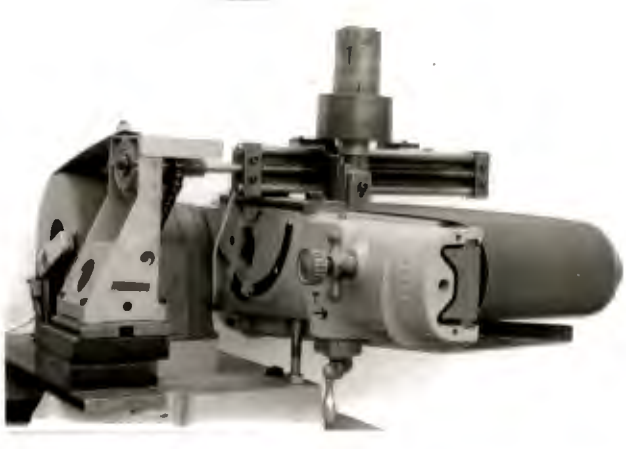

Figure 4.2: The converted Rockwell belt sander used for abrasion testing.

The belt runs at a constant velocity while the machine has been geared to move the specimen across the abrasive belt at a constant transverse velocity; the specimen is thus always being worn against fresh abrasive. The specimen is held firmly in place by the specimen holder. Prior to any testing the material is first 'run-in' until a steady state material loss regime has been achieved. The specimen is then weighed to an accuracy of 0.1 mg. After each 3m abrasion run the specimen is weighed and the mass loss is then converted to a volume loss. The conditions under which the abrasive test were performed are shown in Table 4.3.

Specimen Size	10 mm x 10 mm cross-section
Abrasion Speed (forward)	260 $mm.s^{-1}$
Abrasion Speed (transverse)	2.2 $mm.s^{-1}$
Load	32.1 N
Abrasive Particles	80 grit alumina on an abrasive belt
Abrasive Path Length	4 x 3 m

Table 4.3: The parameters of the abrasion test.

A mild steel (070M20) specimen is included in each test run and is used to calculate the relative abrasion resistance (R.A.R.). The R.A.R. is defined in Equation 4.1.

$$\text{R.A.R.} = \frac{\text{Volume loss per meter of abrasion of the standard material (mild steel)}}{\text{Volume loss per meter of abrasion of the test material}}$$

Equation 4.1

Mild steel will therefore have a R.A.R. value of 1. A material with a R.A.R. value greater than 1 will have better abrasion resistance than mild steel while a value less than 1 will indicate worse abrasion resistance.

4.9 The Abrasion Corrosion test

4.9.1 Abrasion

The abrasion part of the test makes use of the same apparatus as is described in the section on abrasion. The only difference between the abrasion component of the abrasion-corrosion test and the abrasion test is that in the abrasion-corrosion test the abrasion distance is 1m.

4.9.2 Corrosion

The corrosion section of the abrasion-corrosion test was designed to mimic the consequence of a liquid corrosive medium flowing over an abraded surface. The test rig for the corrosion component of the abrasion-corrosion test is shown in Figure 4.3.

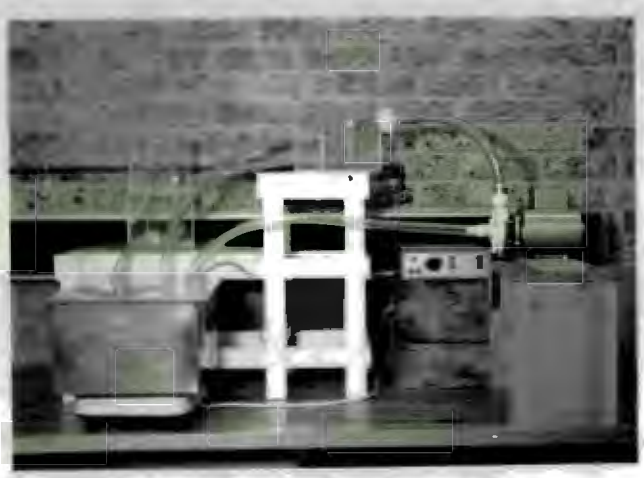

Figure 4.3: The corrosion test rig.

There are a number of features concerning the test rig which are emphasised in this section.

1. The corrosive medium used is a synthetic mine water which is formulated after an analysis of mine water from a mine in the Transvaal[77].

2. The synthetic mine water is aerated as it flows over the specimen. This implies that there is always oxygen available in the liquid for corrosion reactions.

3. The level in the surge tank is kept constant by an overflow pipe which returns excess water back to the reservoir. This produces a constant flow of the corrosive medium.

4. The corrosion test plate holds all nine specimens, one of which is the mild steel standard. The specimens are staggered so that the water flows over only one of the specimens. A flow regulator on the test plate eliminates any turbulence.

5. A thermo-regulator is used to maintain the water at a constant temperature.

Specimen Size	10 mm x 10 mm cross-section
Abrasion Speed (forward)	260 $mm.s^{-1}$
Abrasion Speed (transverse)	2.2 $mm.s^{-1}$
Load	32.1 N
Abrasive Particles	80 grit alumina
Abrasive Path Length	4 x 1 m
Synthetic mine water	518 ppm Total Dissolved Solids (TDS)
Soluble Salt $Na_2SO_4.10H_2O$	2.400 g/l and 343 ppm
$CaCl_2$	0.485 g/l and 175 ppm
pH at start	6.5 to 7.0
Temperature of water	30°C
Duration of corrosion	4 x 22 hrs

Table 4.4: Conditions for the Abrasive Corrosive Wear Test

The relative abrasive-corrosive wear rate (R.W.R.) is defined as the volume loss of a standard material (mild steel) divided by the volume loss of the test material. The volume loss considered is that resulting from both the abrasive component of the test and the corrosive component. Each cycle of abrasion-corrosion represents 1m of abrasion and 22 hours of

corrosion. A single test constitutes four abrasion-corrosion cycles. The wear rates can be computed from the slope of the cumulative volume loss plotted against abrasion distance and corrosion time. The relative abrasive-corrosive wear rate is defined in Equation 4.2.

$$\text{R.A.R.} = \frac{\text{Volume loss per meter of abrasion of the standard material (mild steel)}}{\text{Volume loss per meter of abrasion of the test material}}$$

Equation 4.2

This equation is analogous to the one used to calculate the relative abrasion resistance in the dry abrasion test.

Before being placed in the corrosion chamber the specimens were coated with a lacquer on the five unabraded sides to prevent unwanted corrosion. The lacquer coating was removed with acetone after the corrosion cycle was complete.

The bulk of the corrosion product which remained on the specimens after the corrosion cycle was cleaned off by ultrasonic agitation in a 10 % aqueous solution of di-ammonium hydrogen citrate ($C_6H_{14}N_2O_7$). This proved to be a very mild acid which helped loosen the oxide product without etching away the underlying steel matrix.

4.10. Cavitation

A cavitation environment was reproduced by using an ultrasonic drill. The drill was originally supplied by KLN Ultraschall Gesellschaft of Germany and then assembled by Heathcock [91]. An important feature of the cavitation rig, in contrast to other experimental cavitation rigs, is that this rig accommodates the specimen below a vertically mounted ultrasonic drill. A schematic diagram of the cavitation rig is shown in Figure 4.4.

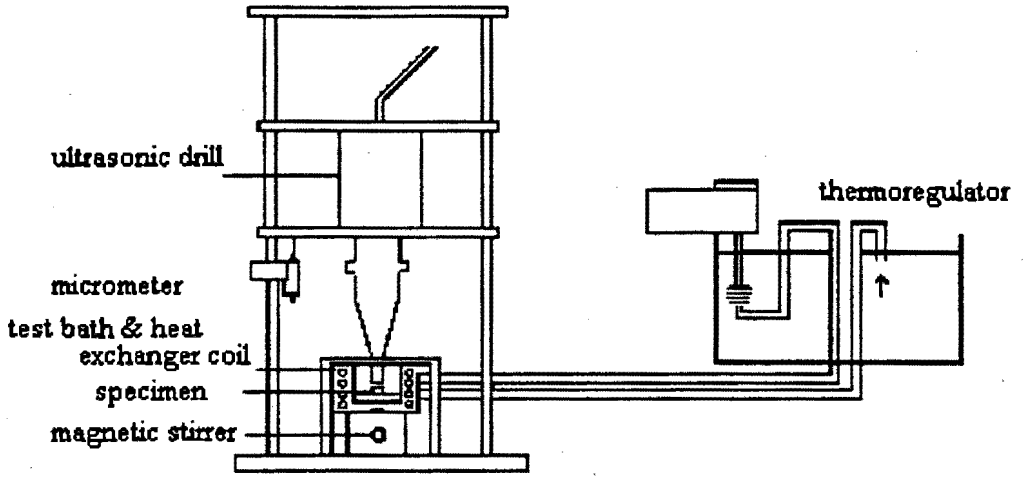

Figure 4.4: The vibratory cavitation erosion test apparatus.

The Ultrasonic drill is mounted vertically above the test specimen. The height is controlled by an appropriately positioned micrometer. The specimen and drill tip are contained in a test bath filled with distilled water The temperature of the water in the test bath is controlled by a heat exchanger coil through which water from a temperature regulated reservoir is pumped. To ensure that there is no localised heating of the distilled water in the test bath during cavitation testing the water is continually stirred by a magnetic stirrer. The test conditions are given in Table 4.5

Drill tip frequency	20 kHz
Distance between drill tip and specimen	0.35 mm
Temperature	25°C
Specimen Geometry	13 mm x 13 mm blocks
Specimen preparation	final polish using 1 μm diamond paste

Table 4.5: The test conditions used for the cavitation test.

Because of the heat expansion of the drill horn the rig was always allowed to warm up for an hour prior to starting the test. During cavitation the specimen was removed from the sample

holder and weighed every hour. The test was concluded after 12 hours of cavitation erosion. The volume loss was then calculated. When the cumulative volume loss is plotted against the cavitation time a distinctive cavitation erosion curve emerges. The curve can be divided into two stages. The first stage is the incubation period during which there is little material loss The second stage is that of steady state erosion where there is a constant rate of material removal from the surface of the eroded specimen. The two stages are shown in the curve in Figure 4.5. The steady state erosion rate is obtained from the slope of the curve in the steady state erosion regime. The incubation time (t_0) is defined as the point where the steady state line intersects the x-axis.

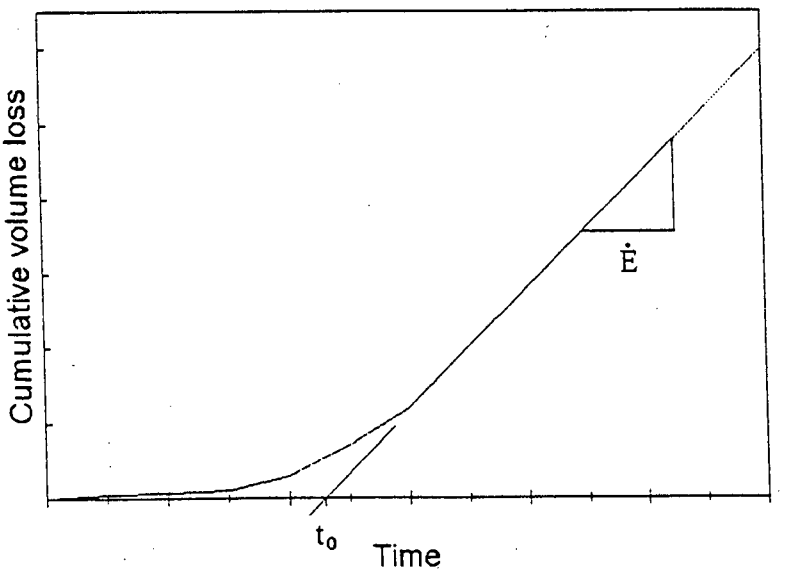

Figure 4.5: A representation of the type of graph obtained when plotting the cumulative volume loss against cavitation erosion time. The incubation time (t_0) and the steady state erosion rate Ė are indicated on the graph.

5. RESULTS

5.1. Microstructure

The microstructure of the alloys tested in their annealed, cold worked and heat treated states are revealed in the following section. The standard alloys AISI 316, AISI 304, Hadfields manganese steel and mild steel will be presented first and then the high nitrogen stainless steel in the annealed condition and in the cold worked conditions will be presented. The microstructure of the vanadium micro-alloyed steel in its various stages of heat treatment will be shown.

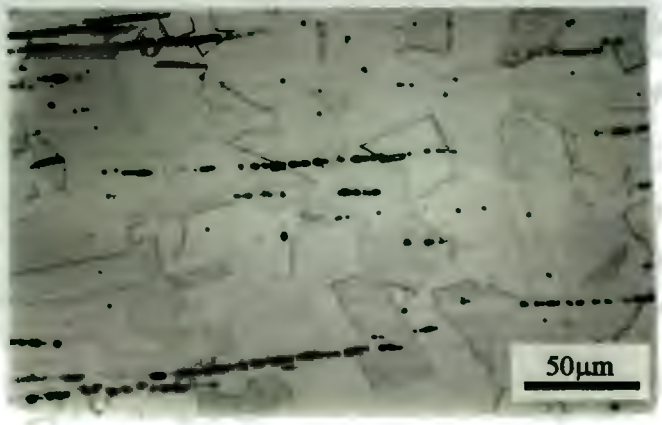

Figure 5.1: AISI 316 consists of austenite, which is reflected by the white area in the micrograph, and retained δ-ferrite which is revealed by the blacks specks in the micrograph.

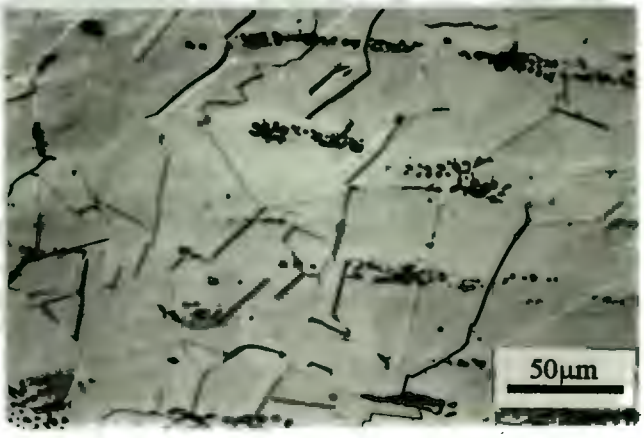

Figure 5.2: AISI 304 is also austenitic, as is seen by the white areas displaying annealing twins, with the dark specks of retained δ-ferrite also present.

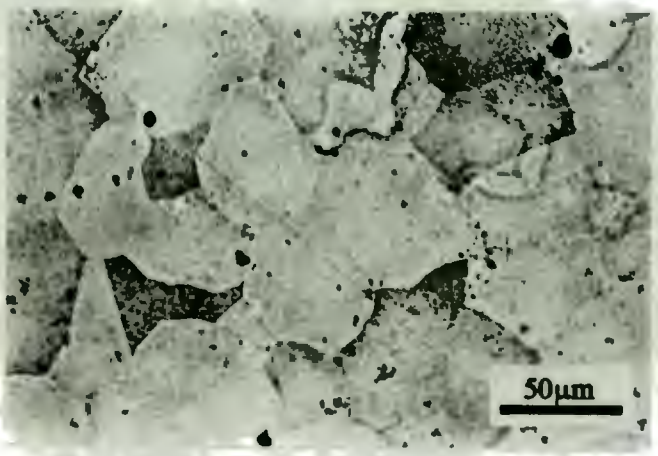

Figure 5.3: Hadfields manganese steel consists of large austenite grains which are about 40 μm in diameter. The are also many impurities present as can be seen by the black specks in the micrograph.

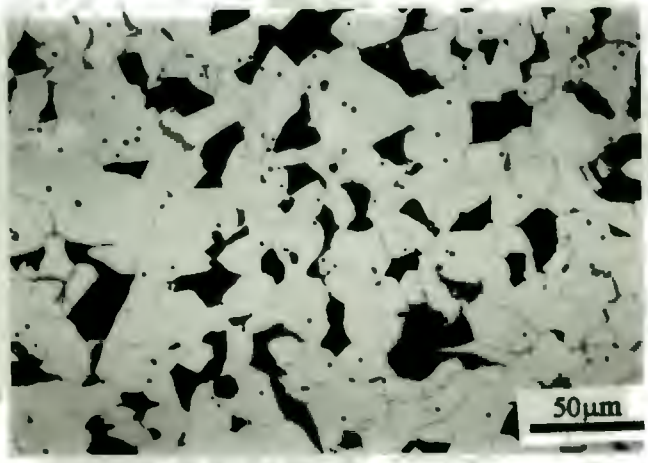

Figure 5.4: Mild Steel is made up of white ferrite grains and dark areas of pearlite.

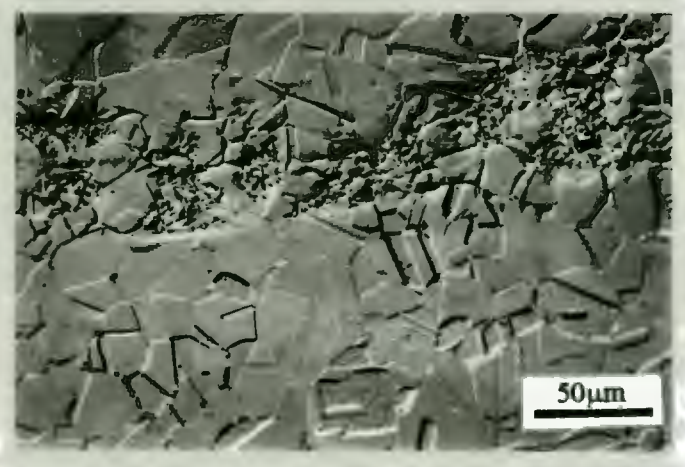

Figure 5.5: The high nitrogen stainless steel 852 in the annealed condition. The grain size is about 20 μm. The dark areas reveal the presence of about 5% δ ferrite.

5.1.1 The effect of cold deformation on the microstructure of annealed 852.

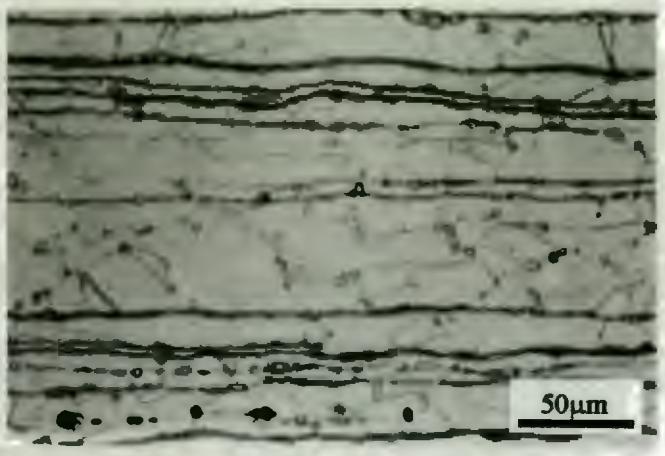

Figure 5.6: 852 after 16% cold reduction. The austenite grains are evident between the lines of ferrite.

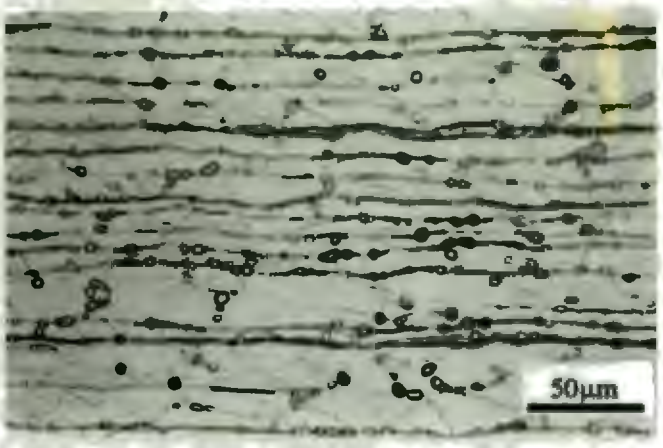

Figure 5.7: 852 after 30% cold reduction. The lines of ferrite are closer together and the austenite grains are still evident.

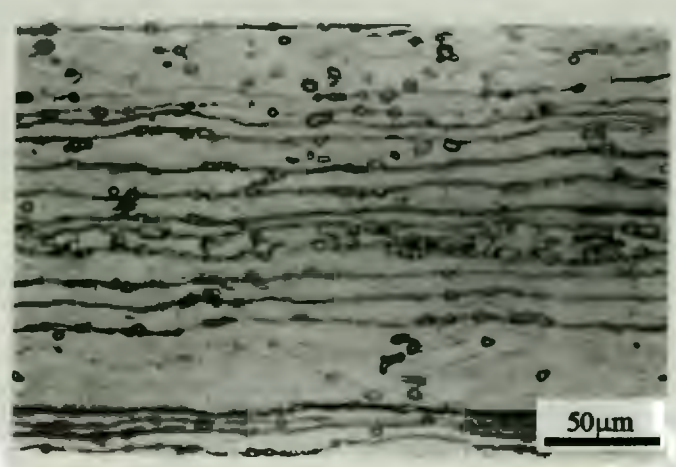

Figure 5.8: 852 after 48% cold reduction. The deformed austenite can be seen between the ferrite bands.

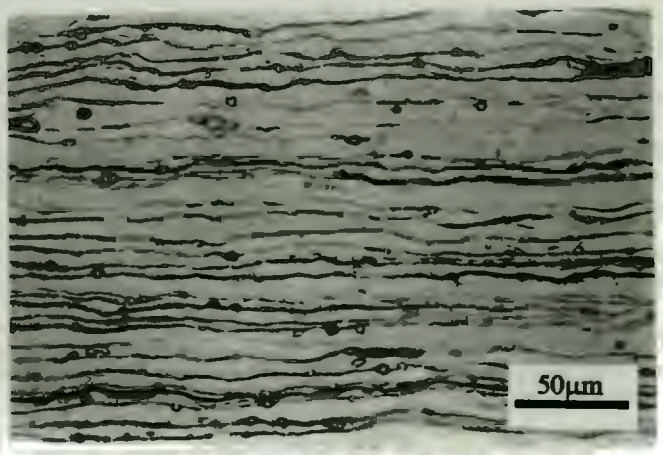

Figure 5.9: 852 after 66% reduction. The deformation induced slip lines can be seen in the austenite but the overwhelmingly noticeable feature is the bands of ferrite.

5.1.2 Microstructure of the vanadium micro-alloyed steel aged at 700°C.

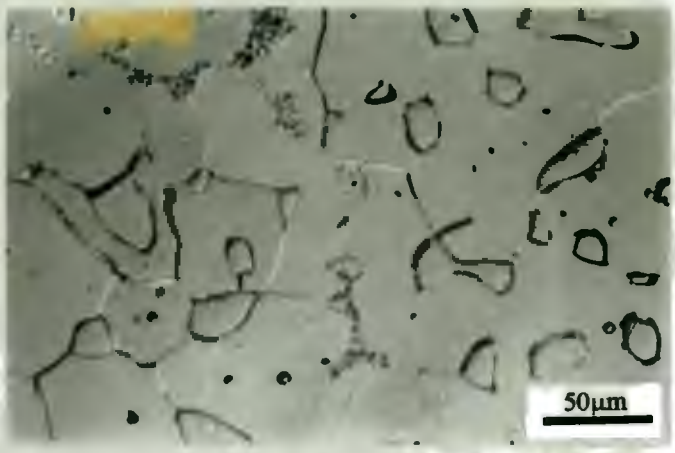

Figure 5.10: Alloy 811 after homogenising at 1250°C for 8 hours. The rounded grains represent the ferrite areas and the remaining material is austenite.

Figure 5.11: 811 after 0.5 hours at 700°C. There is a darkening of the grain boundaries which reveals the beginning of cellular precipitate formation.

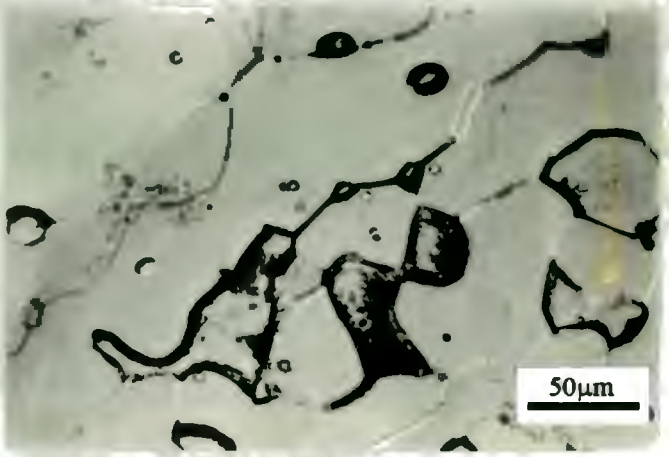

Figure 5.12: 811 after 1 hour at 700°C. The lamellae of Cr_2N and the transformed material is growing into the untransformed grains. At 700°C the cellular precipitation only grows into the ferrite grains and the austenite grains are left unaffected.

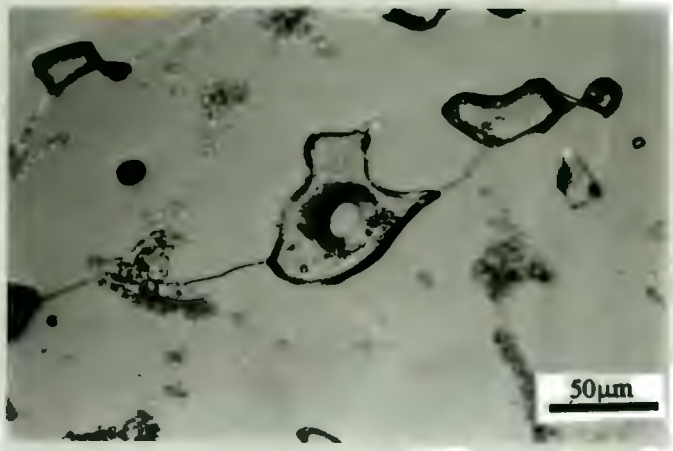

Figure 5.13: 811 after 2 hours at 700°C. Larger areas are now taken up by the precipitates. The austenite remains unaffected.

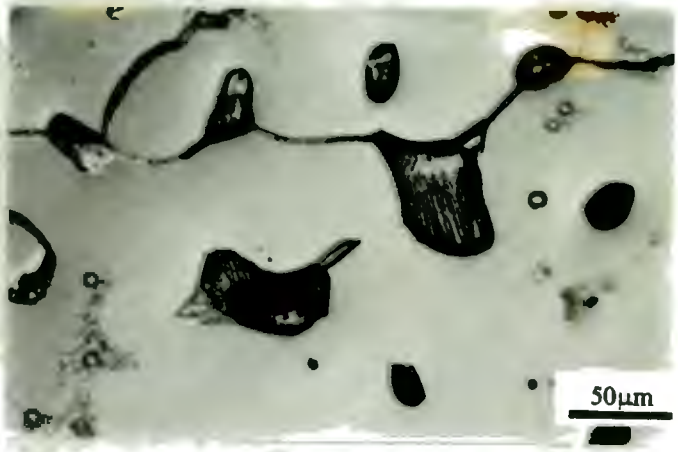

Figure 5.14: 811 after 4 hours at 700°C. The cellular precipitate is threatening to fill entire ferrite grains.

Figure 5.15: 811 after 8 hours at 700°C. Entire ferrite grains are filled with cellular precipitate. It is expected that the precipitation would occur in the ferrite first because nitrogen is less soluble in ferrite than it is in austenite and the formation of cellular precipitates involves the migration of nitrogen out of the matrix.

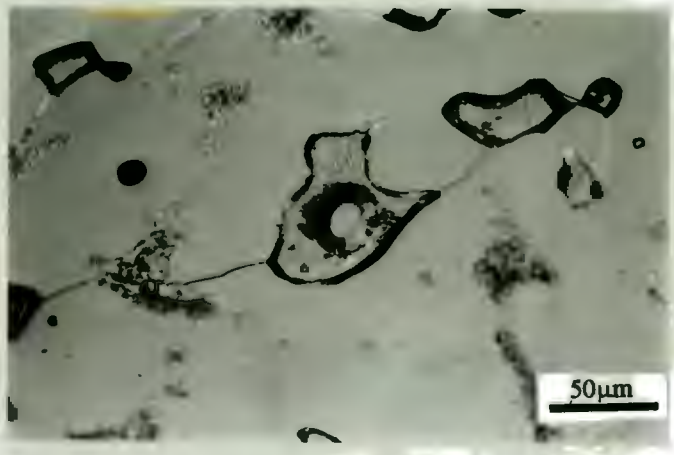

Figure 5.13: 811 after 2 hours at 700°C. Larger areas are now taken up by the precipitates. The austenite remains unaffected.

Figure 5.14: 811 after 4 hours at 700°C. The cellular precipitate is threatening to fill entire ferrite grains.

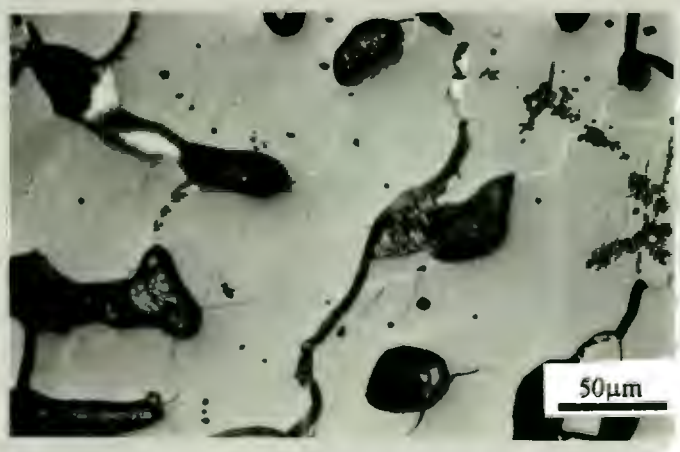

Figure 5.15: 811 after 8 hours at 700°C. Entire ferrite grains are filled with cellular precipitate. It is expected that the precipitation would occur in the ferrite first because nitrogen is less soluble in ferrite than it is in austenite and the formation of cellular precipitates involves the migration of nitrogen out of the matrix.

5.1.3 Microstructure of the vanadium micro-alloyed steel aged at 900°C.

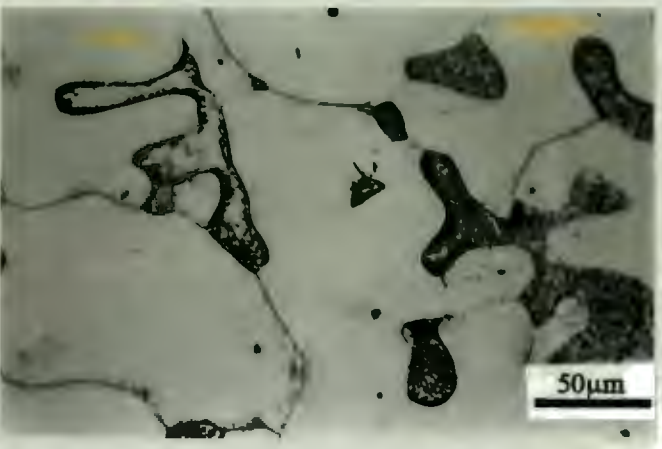

Figure 5.16: 811 after 0.5 hours at 900°C. Some grain boundaries show the initial stages of precipitation. The initial precipitation occurs from the grain boundaries into the ferrite grains.

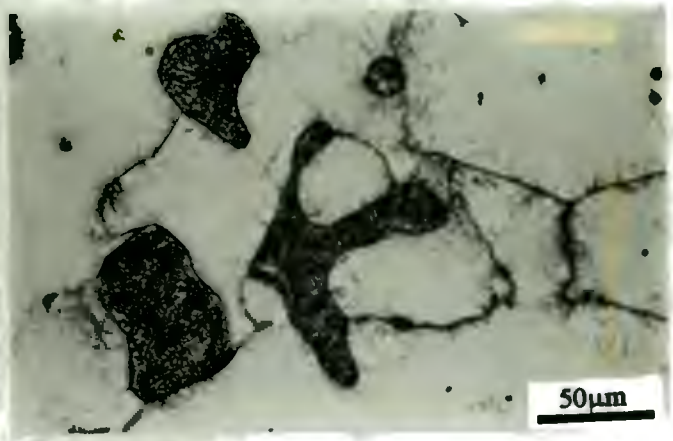

Figure 5.17: 811 after 1 hour at 900°C. In the ferrite grains the cellular precipitation is close to complete, whilst precipitation continues in the austenite grains. The precipitation in the austenite grains have either a plate or needle like morphology.

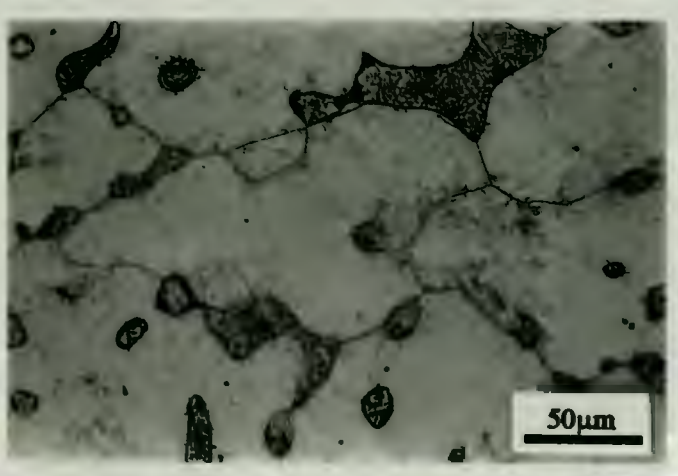

Figure 5.18: 811 after 2 hours at 900°C. The is evidence of recrystallization and grain growth as well as a continuation of the precipitation.

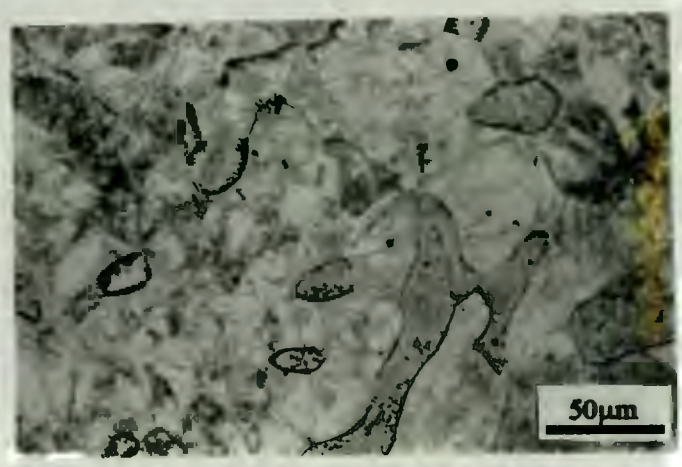

Figure 5.19: 811 after 4 hours at 900°C. Further grain growth and precipitation. There is no evidence of the formation of vanadium precipitates and further work is necessary to determine whether these precipitates do form.

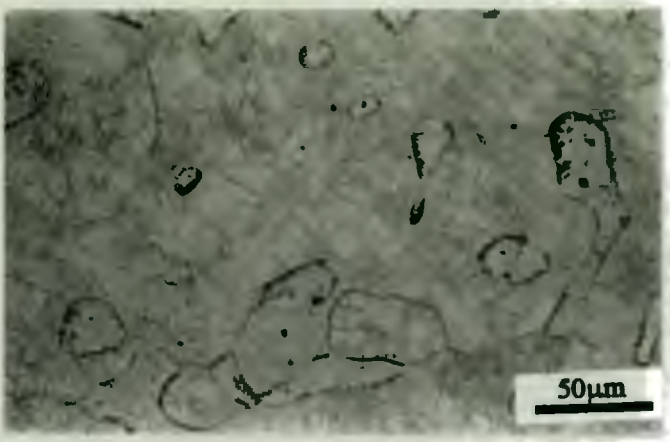

Figure 5.20: 811 after 8 hours at 900°C. There is grain growth within some of the grains.

5.2. M_{d30} Values

Alloy	M_{d30} (°C) from equation 3.7
852	-244.3
AISI 304	40.8
AISI 316	9.5
Hadfields	-326.4

Table 5.1: The M_{d30} values of the stainless steels tested in this thesis.

The M_{d30} values given here are obtained by using equation 3.7 which was derived from alloys with specific compositions. The equations used for calculating M_{d30} are highly dependant on the composition of the alloy and small deviations from the composition for which the equation was originally designed can lead to errors in the M_{d30} value. It must therefore be made clear

that the values in the table above are only for comparative purposes. Hadfields manganese steel has the lowest M_{d30} value, which implies that it will be the least likely to transform to martensite. The high nitrogen stainless steel has a very low M_{d30} temperature and this indicates that it will not readily transform. It will require high shear rates to oblige this alloy to transform to martensite. The next lowest value is that of AISI 316 and then AISI 304. This suggests that AISI 304 transforms from austenite to martensite easier than AISI 316.

5.3. Hardness Tests

The results obtained from hardness tests on the materials in the annealed condition are presented in Table 5.2.

Alloy	Hardness (VH)
Mild Steel	190
AISI 304	199
AISI 316	208
Hadfields Manganese Steel	328
852 (high nitrogen-manganese steel)	321
811 (vanadium micro-alloyed steel)	230

Table 5.2: The Hardness of the alloys used in this study in the annealed state.

The mild steel used for reference purposes in the abrasion test has the lowest surface hardness, followed by AISI 304, then AISI 316 the vanadium micro-alloyed steel alloy, 811. Hadfields manganese steel, and 852 all have very similar Vickers hardness values.

The hardness of the cold worked high nitrogen stainless steels have been tested and the results are presented in Figure 5.21.

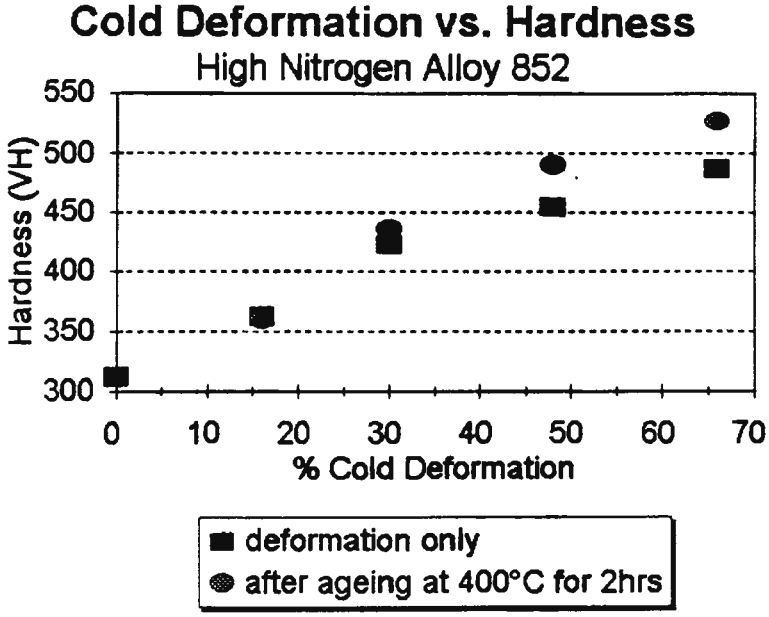

Figure 5.21: The effect of cold deformation and strain ageing on the hardness of the high nitrogen stainless steel 852.

5.3.1 Ageing Time

The effect of ageing time on the hardness of the vanadium micro-alloyed steel is not as pronounced as expected. Figure 5.22 shows the effect of heat treating for various times at 700°C and Figure 5.23 shows the effect on hardness after ageing at 900°C.

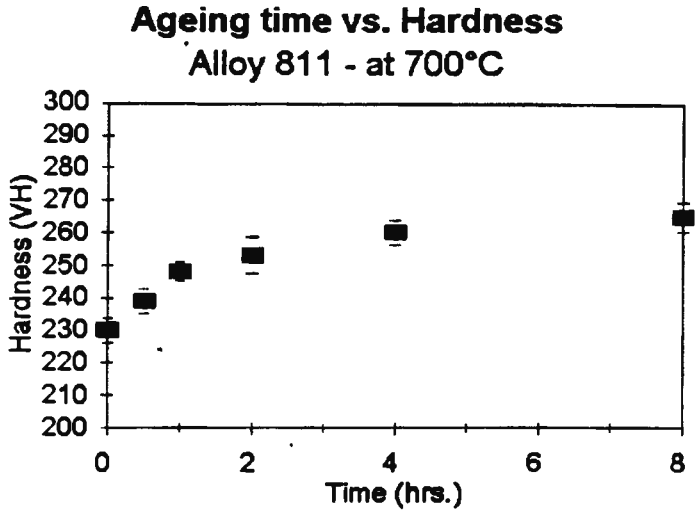

Figure 5.22: The effect of ageing at 700°C on the hardness of the vanadium micro-alloyed steel. There is a gradual increase in the hardness until the maximum hardness is reached after 8 hours of ageing. This corresponds to the stage, after 8 hours, where the ferrite grains are completely transformed to cellular precipitate.

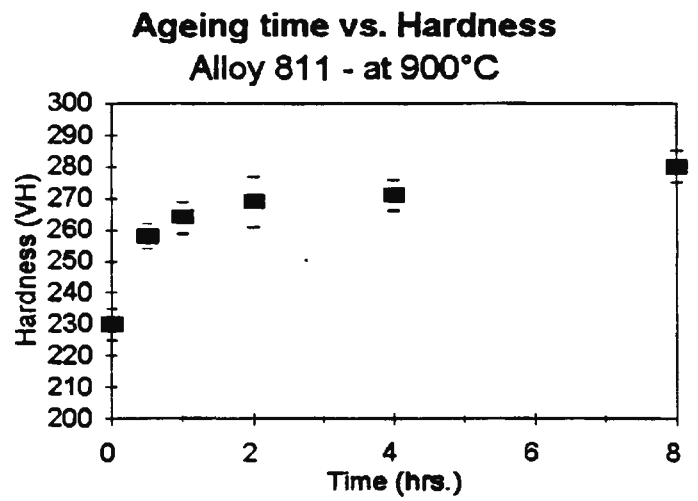

Figure 5.23: The effect of ageing at 900°C on the hardness of the vanadium micro-alloyed steel. There is a rapid rise in the hardness in the first two hours of ageing. When comparing this to the microstructure this is also the time during which the ferrite grains transform to cellular precipitate. After 2 hours of ageing the hardness levels off. When comparing these results with the microstructure the formation of the precipitates within the austenite do not contribute to the hardness.

There is only a 13% increase in hardness after ageing at 700°C for 8 hours and a 20% increase in hardness after ageing at 900°C for 8 hours. The peak hardness is achieved after 4 hours of ageing at 700°C and after 2 hours when ageing at 900°C.

5.4 Tensile Tests

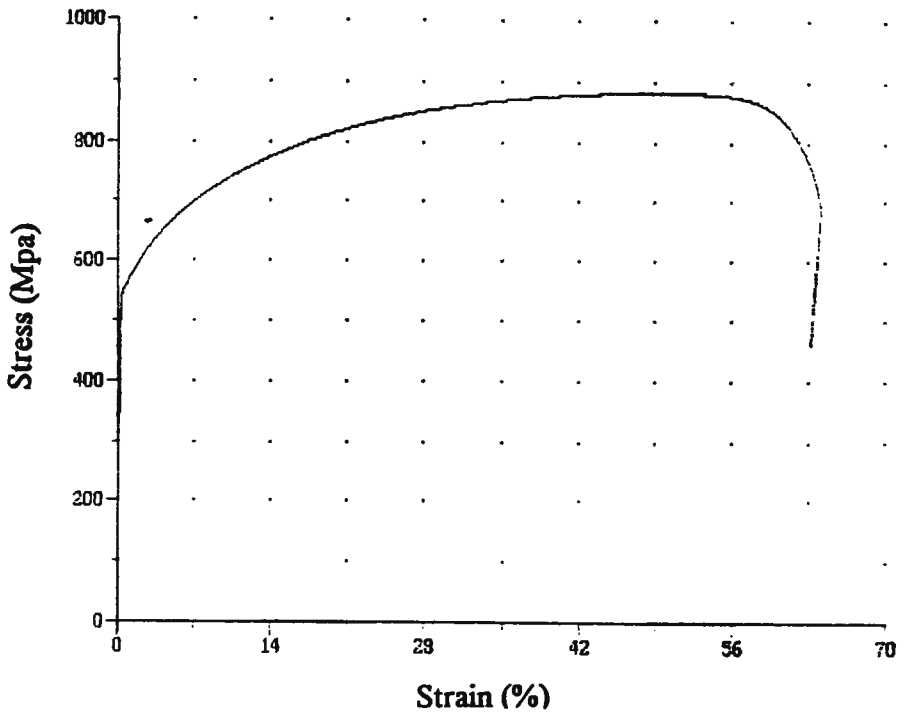

Figure 5.24: The stress-strain curve of the high nitrogen alloy 852.

The stress vs. strain curve reveals that the high nitrogen stainless steel in the annealed state has a yield strength of 550 MPa and a tensile strength of 880 MPa. There is 41% uniform elongation.

5.4.1 Work Hardening Rate

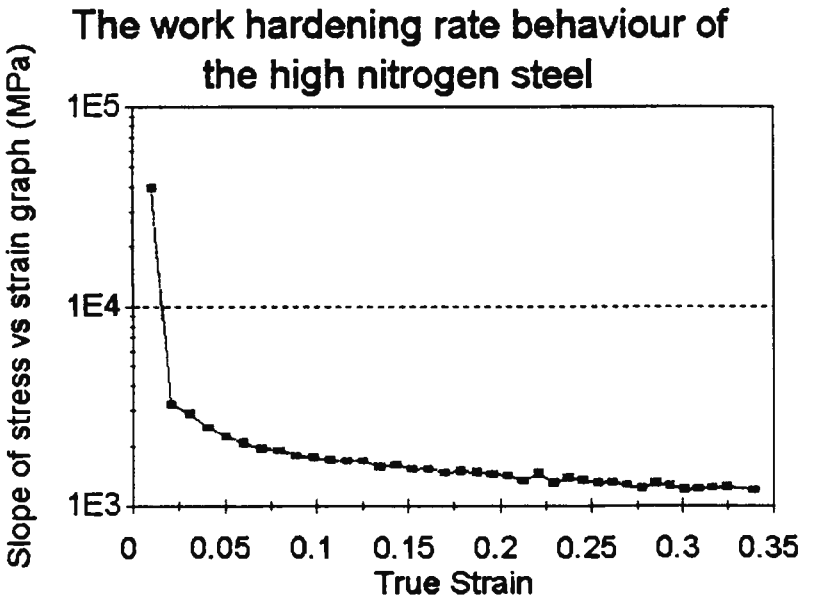

Figure 5.25: The work hardening rate behaviour of 852.

There is a rapid decrease in the WHR until before a strain of 0.05 after which there is a gradual parabolic decrease with the rate becoming constant at a strain of 0.3. Note that the decrease in the WHR is constant with no sharp rises or peaks in the curve. This is indicative of a stable austenitic stainless steel.

5.5 Abrasion

The results presented below are those obtained from tests performed on the dry abrasion rig as described in section 4.8.

Alloy	Volume loss per meter of abrasion (mm^3)	Relative Abrasion Resistance (R.A.R)
Mild Steel	1.32	1.00
AISI 304	1.14	1.15
AISI 316	0.97	1.36
Hadfields Manganese Steel	0.68	1.94
852	0.86	1.53
811	0.76	1.74

Table 5.3: The volume loss per meter of abrasion and the relative abrasion resistance (R.A.R.) of the steels tested.

The results presented in Table 5.3 show the abrasion resistance of the steels tested. Mild steel has the worst abrasion resistance. The stainless steel AISI 304 ranks as the next worst followed by AISI 316. The high nitrogen stainless steel, 852, and the vanadium micro-alloyed steel, 811, perform better than the other stainless steels, AISI 316 and AISI 304. The best performer, in dry abrasion conditions, is Hadfields manganese steel.

The effect of cold work on the abrasion resistance of the high nitrogen alloy 852 has also been tested. The influence of cold work and strain ageing on the rate of material loss is shown in Figure 5.26.

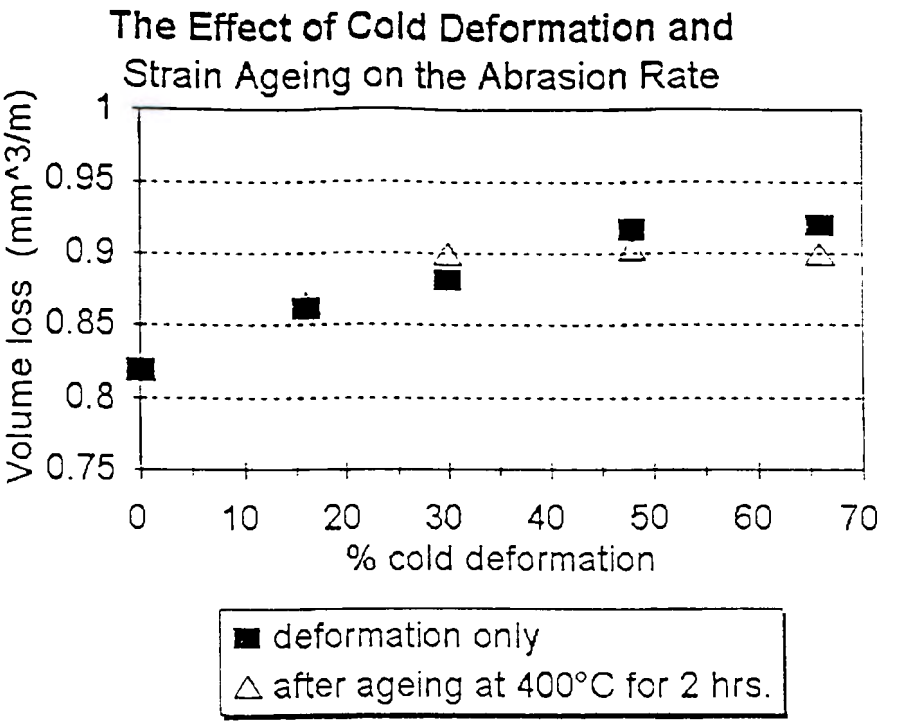

Figure 5.26: The effect of cold work and strain ageing on the abrasion resistance of the high nitrogen stainless steel.

An investigation of the wear surfaces of these differently cold worked materials shows that there is essentially no difference in the mode of wear for each of the cold worked states. Strain ageing has no measurable effect on the abrasion resistance of this material. The wear mode is also very similar. SEM micrographs of the wear surfaces of these steels are shown in Figure 5.27 to Figure 5.29.

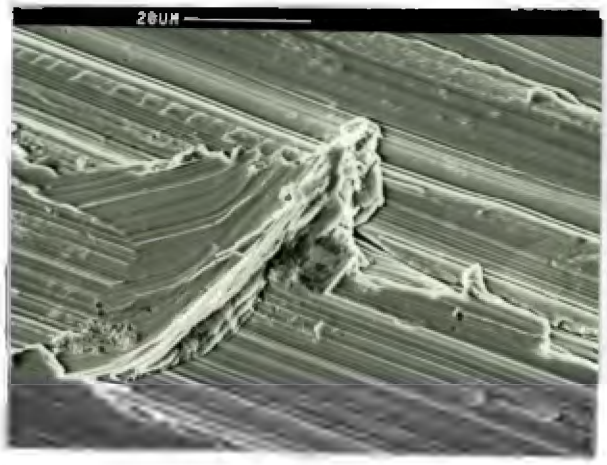

Figure 5.27: The wear surface of annealed 852. This micrograph shows a more ductile form of material deformation than in the following micrographs. This swaf is in the work hardened state and will be lost during subsequent abrasion.

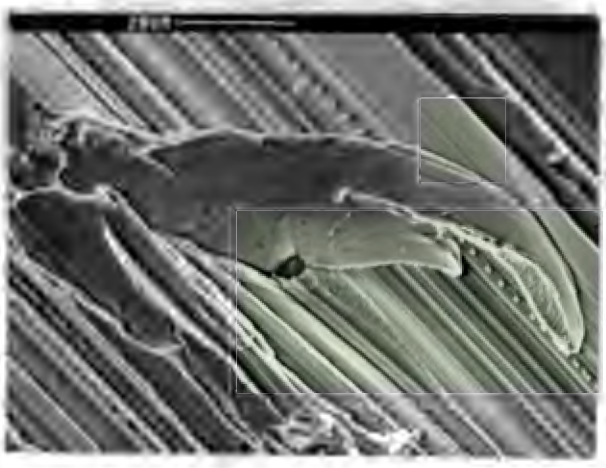

Figure 5.28: The wear surface of 852 cold rolled to 66% reduction exhibiting work hardened lips on the edges of the wear path.

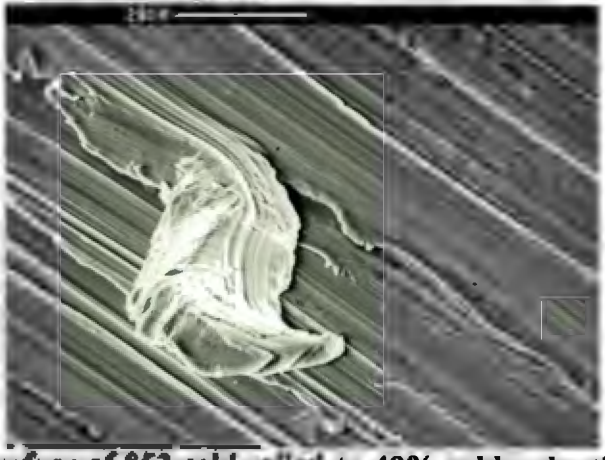

Figure 5.29: The wear surface of 852 cold rolled to 48% cold reduction and then strain aged at 400°C for 2 hours. The wear topography is very similar to the topography presented in the previous two micrographs.

The abrasion resistance of the vanadium micro-alloyed steel is shown in Figure 5.30 and Figure 5.31. Figure 5.30 shows the effect of a heat treatment at 700°C on the abrasion resistance while Figure 5.31 shows the effect of a heat treatment at 900°C. The heat treatment time is shown on the x-axis. Considering a 5% error on all the abrasion results the heat treatment at 700°C has no effect on the abrasion resistance of the material. After ageing at 900°C there is a slight decrease in the ability of the material to resist abrasion. When comparing these results to those obtained for hardness in Figure 1.23 it is apparent that very little comparisons can be drawn between the change in hardness and the abrasion resistance.

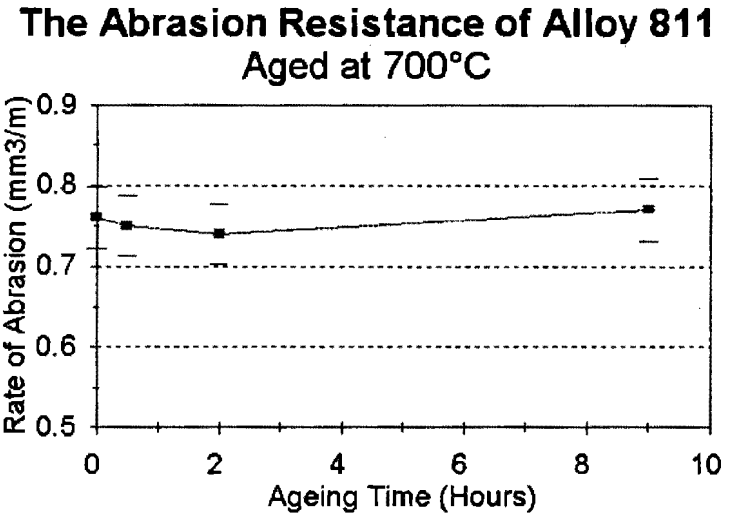

Figure 5.30: The abrasion resistance of alloy 811 aged at 700°C.

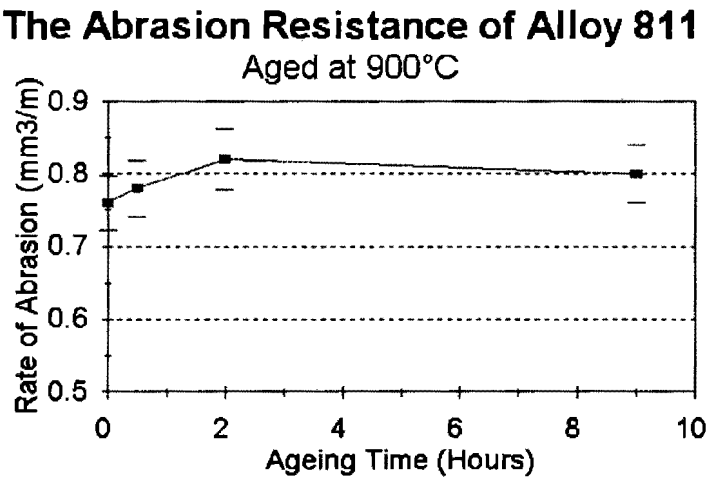

Figure 5.31: The abrasion resistance of alloy 811 aged at 900°C.

The wear surfaces of the vanadium micro-alloyed steels all exhibit very similar features and it is difficult to ascribe any differences in the wear rates to any different mode of material loss. The micrographs below show the post wear topography of the vanadium micro-alloyed steel after the heat treatments.

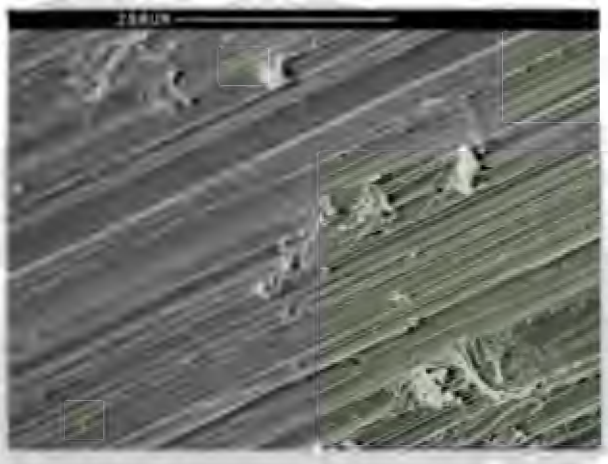

Figure 5.32: The wear surface of homogenised 811, showing the usual characteristics of abrasion wear surfaces, namely wear tracks and plastically deformed shear lips.

Figure 5.33: The wear surface of 811 aged at 700°C for ½ an hour. There is very little difference in the appearance compared with the previous micrograph. This micrograph shows the shear lips being removed from the bulk material.

Figure 5.34: The wear surface of 811 aged at 700°C for 2 hours. Again, there is little difference in the wear surface. This micrograph shows the embedding of an abrasive particle.

Figure 5.35: The wear surface of 811 aged at 700°C for 8 hours. This micrograph shows the removal of a shear lip.

As is evident from the above four micrographs, there is no distinguishable difference in the topography of the wear surface. All the micrographs show the removal of material at the leading edge of the abrasive track, and also show the work hardened shear lips which are removed in the course of further abrasion.

Fig ıre 5.36: The wear surface of 811 aged at 900°C for ½ an hour. This micrograph presents a good example of the work hardened shear lips.

Figure 5.37: The wear surface of 811 aged at 900°C for 2 hours. Work hardened lips of material being removed from the surface.

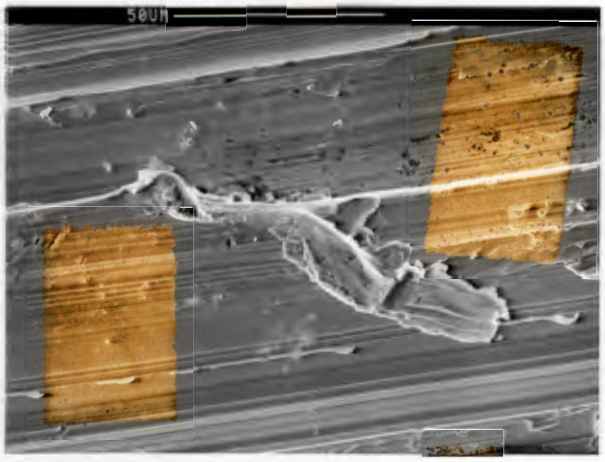

Figure 5.38: The wear surface of 811 aged at 900°C for 8 hours.

The series of micrographs shown above indicates that ageing at 900°C also results in no difference in the wear topography of the aged vanadium micro-alloyed steel.

5.6 Abrasion Corrosion

The standard abrasion-corrosion test described in the section discussing the experimental methods was performed on mild steel, Hadfields manganese steel, AISI 304, AISI 316 and the high nitrogen steel, 852. The test was not conducted on 852 which had been cold worked and strain aged nor on the aged vanadium micro-alloyed steel. It was decided that because the test was not sensitive enough to record the differences between AISI 304, AISI 316 and 852 it would not be able to give any meaningful information on the effect of cold work, strain ageing or precipitation hardening. The graphs below indicate the contributory effect of abrasion and corrosion to the material loss.

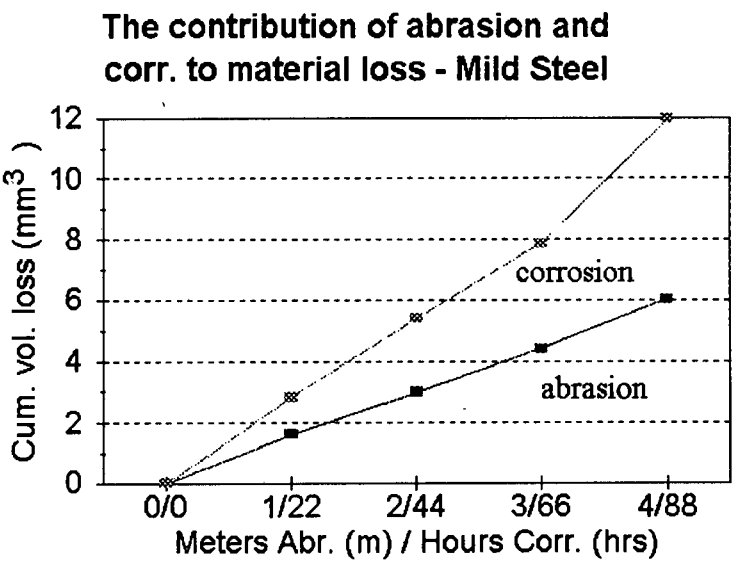

Figure 5.39: The abrasion-corrosion of mild steel.

Figure 5.39 shows the contribution of abrasion and corrosion to the total material loss of mild steel. It is evident that the contribution of corrosion is as great as the contribution of abrasion.

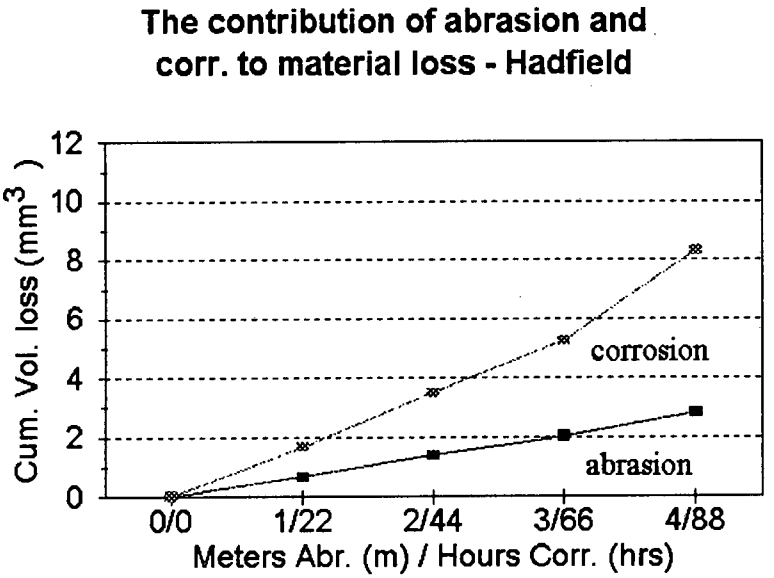

Figure 5.40: The abrasion-corrosion of Hadfields manganese steel.

Hadfields manganese steel shows greatly superior abrasion resistance when compared with mild steel, but the contribution of corrosion to the wear resistance results in the material having poor abrasion corrosion resistance.

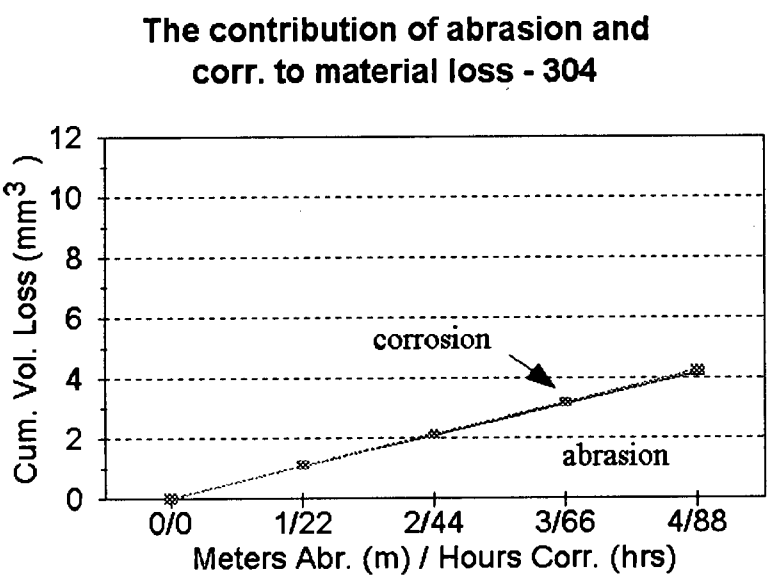

Figure 5.41: The abrasion-corrosion of AISI 304.

Figure 5.41 shows that the only contribution to material loss in AISI 304 is due to the abrasion. The corrosive effect is so mild that it shows virtually no effect on the total material loss.

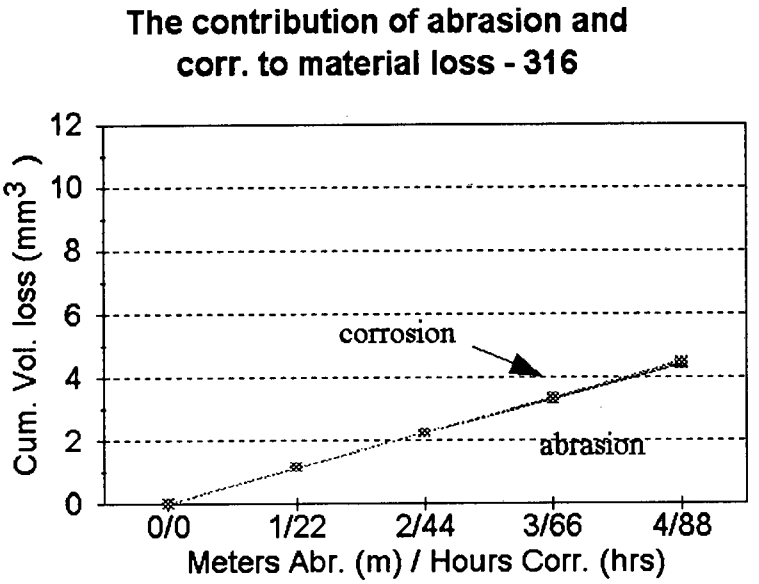

Figure 5.42: The abrasion-corrosion of AISI 316.

AISI 316 has very similar abrasion-corrosion results as that of AISI 304, this is essentially because they are both stainless steel and are therefore barely affected by the mild corrosive environment and they also have very similar dry abrasion resistance.

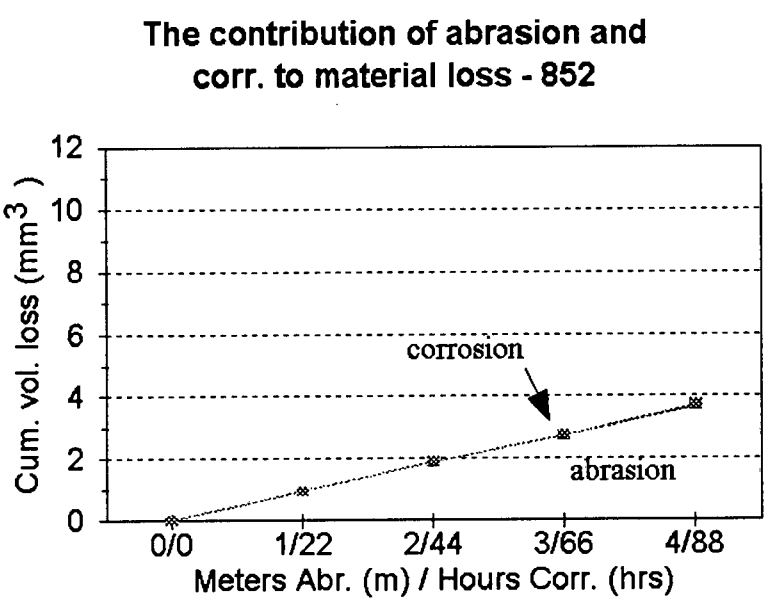

Figure 5.43: The abrasion-corrosion of 852.

Corrosion also has a very negligible effect on the material loss of 852. The greatest contribution to material loss is from abrasion. The abrasion-corrosion resistance is better than that of AISI 316 and AISI 304, in line with the results obtained for dry abrasion.

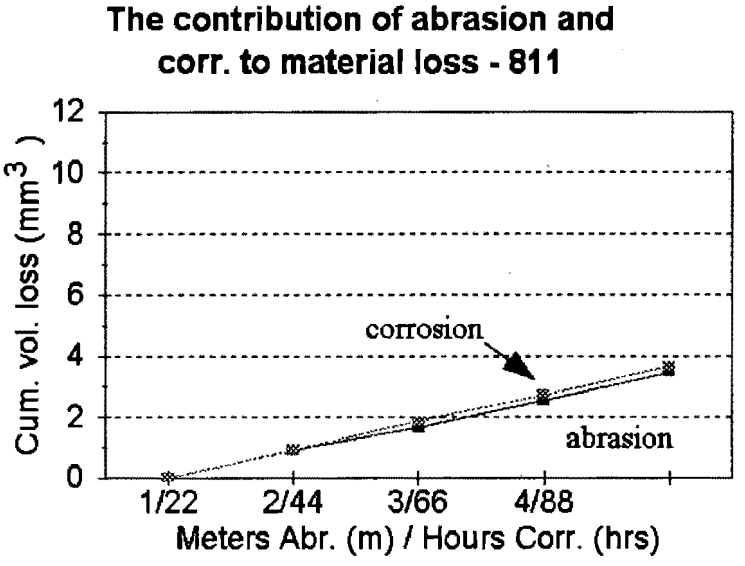

Figure 5.44: The abrasion-corrosion of 811.

The abrasion -corrosion results of the vanadium micro-alloyed steel show that it has the same abrasion-corrosion resistance as the high nitrogen stainless steel 852.

Table 5.4 gives a clear indication of the effect of corrosion on the wear of steels. Where Hadfields manganese steel was twice as good as mild steel under abrasion conditions it is only about 1½ times better when the effects of corrosion are taken into account. This is in stark contrast to the stainless steels, and most especially 852, which increase their resistance to wear relative to mild steel. Alloy 852 is three times more resistant to abrasive-corrosive wear than mild steel.

Alloy	Volume loss due to abrasion and corrosion (mm^3)	Relative Wear Resistance (R.W.R.)
Mild Steel	2.89	1.00
AISI 304	1.06	2.73
AISI 316	1.11	2.60
Hadfields Manganese Steel	2.02	1.43
852	0.92	3.14
811	0.92	3.14

Table 5.4: The volume loss due to abrasion and corrosion and the relative wear resistance (R.W.R.) of the materials tested.

It is interesting to note the effect of the corrosion on the rate of abrasion. Table 5.5 shows the abrasion rates of the materials tested when the abrasion was interrupted by corrosion as in the abrasion-corrosion test. This data shows that not only does the corrosion cause material loss but a cycle of corrosion increases the material loss due to abrasion once the corrosion cycle is complete.

Alloy	Volume loss per meter of abrasion (mm^3)	Relative Abrasion Resistance when abrasion is interrupted by corrosion (R.A.R)	Relative Abrasion Resistance without corrosion (R.A.R)
Mild Steel	1.48	1.00	1.00
AISI 304	1.04	1.42	1.15
AISI 316	1.10	1.35	1.36
Hadfields	0.70	2.11	1.94
852	0.91	1.63	1.53
811	0.85	1.74	1.74

Table 5.5: The volume loss per meter of abrasion and the R.A.R. after the material has been subject to the corrosion component of the abrasion corrosion test. The values obtained for abrasion without any influence of corrosion, as presented in Table 5.3, are included in the last column for comparison.

5.7 Cavitation

The cavitation resistance of the materials tested are shown in Table 5.6 below. The values obtained for the incubation period and steady state erosion rate are obtained as outlined in section 4.10.

Alloy	Incubation Period (hrs.)	Steady State Cavitation Rate (mm^3/hr)
Hadfields Manganese Steel	2.17	0.10
AISI 304	4.31	0.09
AISI 316	1.79	0.32
852	4.82	0.05
811	3.60	0.05

Table 5.6: The incubation period and steady state cavitation rate of the materials tested.

Hadfields manganese steel performs particularly well when compared with AISI 316 stainless steel both in terms of the incubation period and the erosion rate. The stainless steels AISI 304 and AISI 316 have markedly different incubation periods and erosion rates. This is surprising considering their similarities. The differences in performance will be explained in the discussion section in section 6. The high nitrogen stainless steel 852 has the best cavitation erosion resistance. The reasons for this will be outlined in the discussion section.

SEM micrographs of the eroded surface show the salient features with respect to the mode of cavitation erosion.

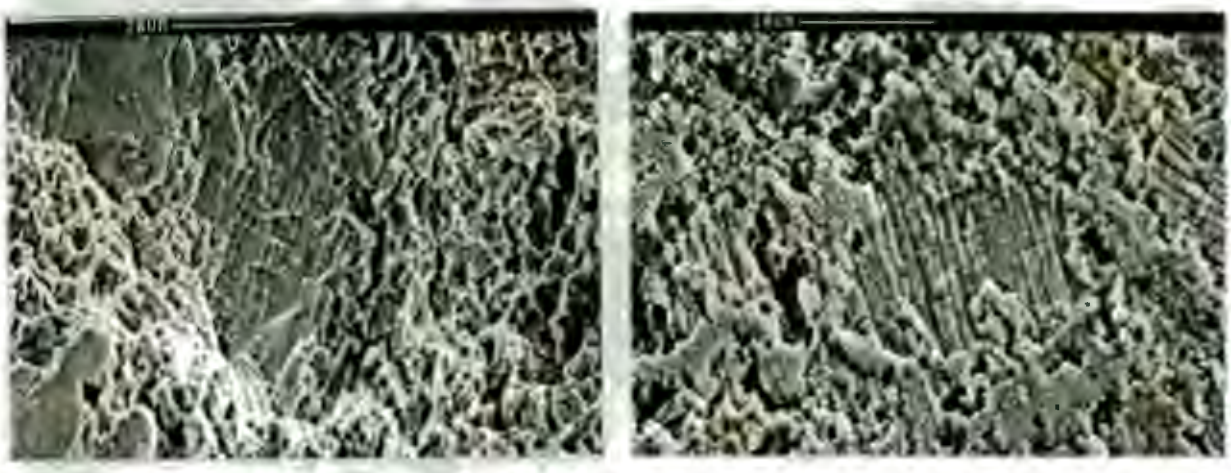

(a) (b)

Figure 5.45: The cavitation eroded surface of Hadfields manganese steel after 12 hours of cavitation. Micrograph (a) shows evidence of slip lines at the top left of the micrograph. Micrograph (b) shows parallel sets of slip lines and the subsequent erosion of these lines. Micrograph (b) was taken from the edge of the cavitated area.

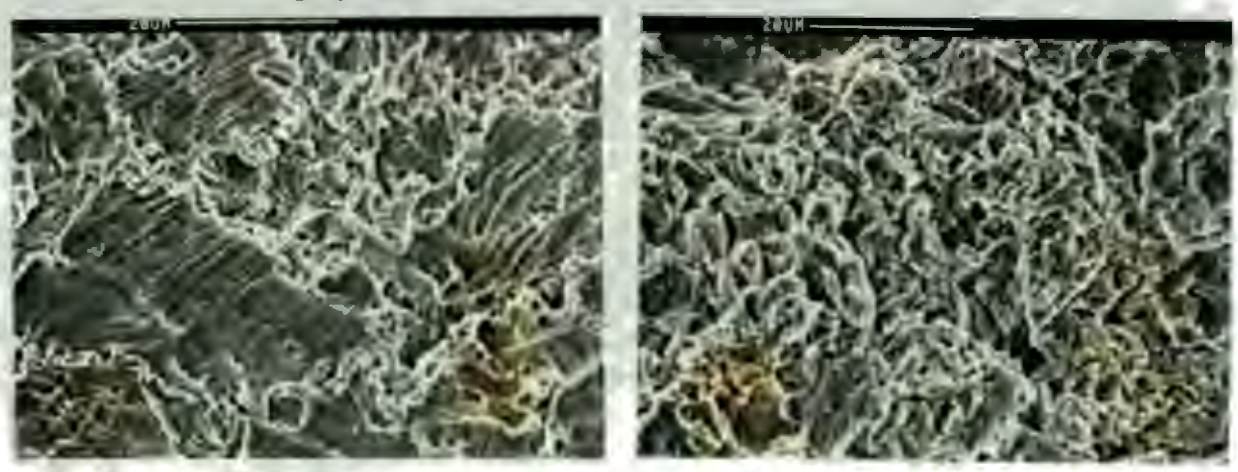

(a) (b)

Figure 5.46: The cavitation eroded surface of AISI 304 after 12 hours of cavitation. Micrograph (a) shows an area near the edge of the eroded area where slip lines have been formed and material eroded. Micrograph (b) shows a section in the middle of the eroded area with dimpling of the surface and the removal of the material by the joining of sub-surface cracks.

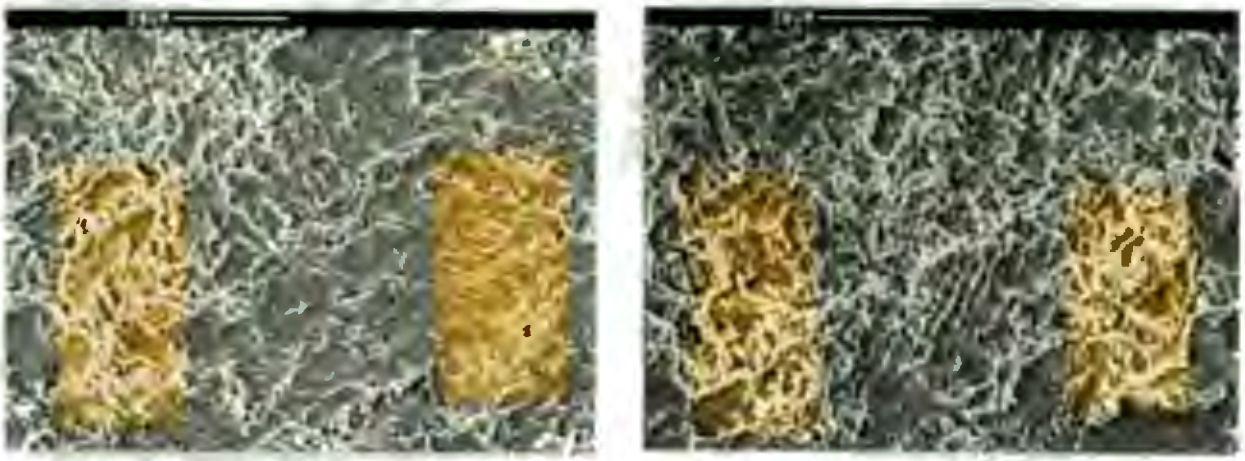

(a) (b)

Figure 5.47: The cavitation eroded surface of AISI 316 after 12 hours showing the formation of slip lines, (a), and the dimpling effect and removal of material, (b).

Figure 5.48: The cavitation eroded surface of 852 after 12 hours of cavitation erosion. There is evidence of small cracks propagating between the dimples. The joining of these cracks cause material loss.

5.8. Cavitation Erosion as a Function of Cold Work

The effect of cold work on the cavitation erosion of the high nitrogen austenitic stainless steel was investigated. The results obtained from the four cold rolled states are presented in Table 5.7.

The deformed material was strain aged and an increase in the steady state cavitation erosion rate is shown in Table 5.6 and Figure 5.49. The material with between 16% and 48% cold deformation shows the largest improvement in the cavitation erosion resistance after strain ageing. The strain ageing of material deformed by less than 16% or more than 48% has little effect on the cavitation erosion resistance.

% cold deformation of Alloy 852	Incubation Period (hrs.)	Steady State Cavitation Rate (mm^3/hr)	Steady State Cavitation Rate after Strain Ageing (mm^3/hr)
0%	4.8	0.050	0.050
16%	4.8	0.034	0.026
30%	5.0	0.024	0.019
48%	5.8	0.018	0.016
66%	6.0	0.008	0.007

Table 5.7: This table shows the effect of cold deformation and strain ageing on the incubation period and the steady state cavitation erosion rate of the high nitrogen stainless steel.

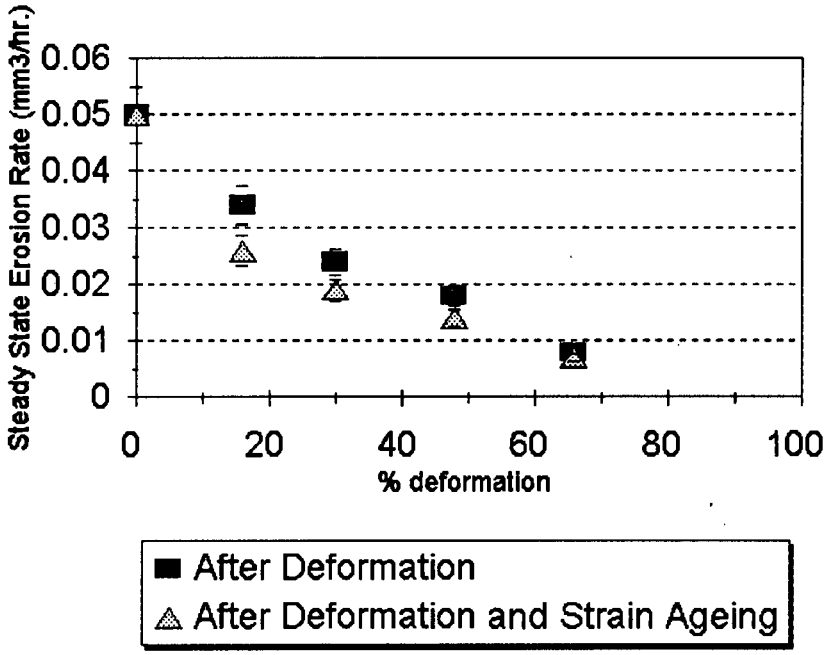

Figure 5.49: The effect of cold deformation and strain ageing on the steady state cavitation rate of alloy 852

5.8.1 Investigation of the cavitation mechanism

A series of SEM micrographs were taken to track the progress of the cavitation erosion in the annealed and cold worked 852. Micrographs of the eroded material are taken at set intervals with the time indicated below each micrograph. The cavitation of the annealed 852 and 852 with 16% and 66% prior cold deformation is investigated. The intermediate cold deformation stages (30% and 48%) are found to display intermediate topographical features and are therefore not presented. The cavitation of 852 with 30% and 48% cold deformation will nonetheless be discussed in the discussion section. The SEM micrographs reveal the erosion mechanisms operating at different times and at different stages in annealed and cold worked 852.

5.8.1.1 Cavitation of annealed 852

Figure 5.50: Annealed 852 cavitated for 10 minutes. There is evidence of the surface becoming uneven and the grain boundaries becoming raised.

Figure 5.51: After the annealed 852 has been cavitated for ½ an hour the grain boundaries are raised further.

Figure 5.52: The annealed 852 cavitated for 1 hour shows the removal of material from the grain boundaries and evidence of slip lines within the grains.

Figure 5.53: Annealed 852 cavitated for 1½ hours has larger pieces of material removed from the grain boundaries.

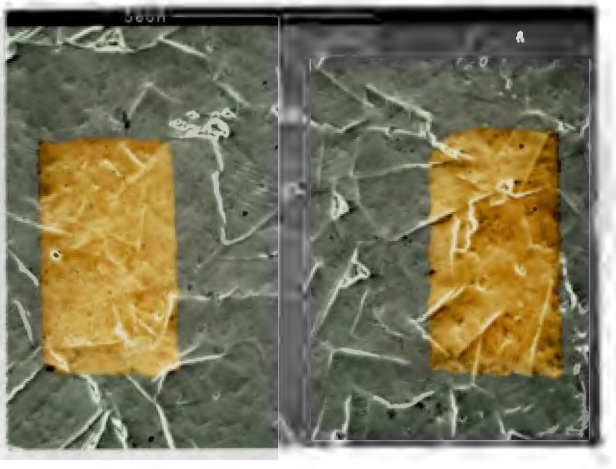

Figure 5.54: Annealed 852 cavitated for 2 hours has more material removed from the grain boundaries. The slip lines within the grain boundaries become more predominant.

(a) (b)

Figure 5.55: Annealed 852 cavitated for 3 hours, (a) shows the process of fatigue whereby the material is removed from the grain boundaries. The fatigue striations can be seen where the material has been removed. Micrograph (b) shows slip and grain boundary material removal.

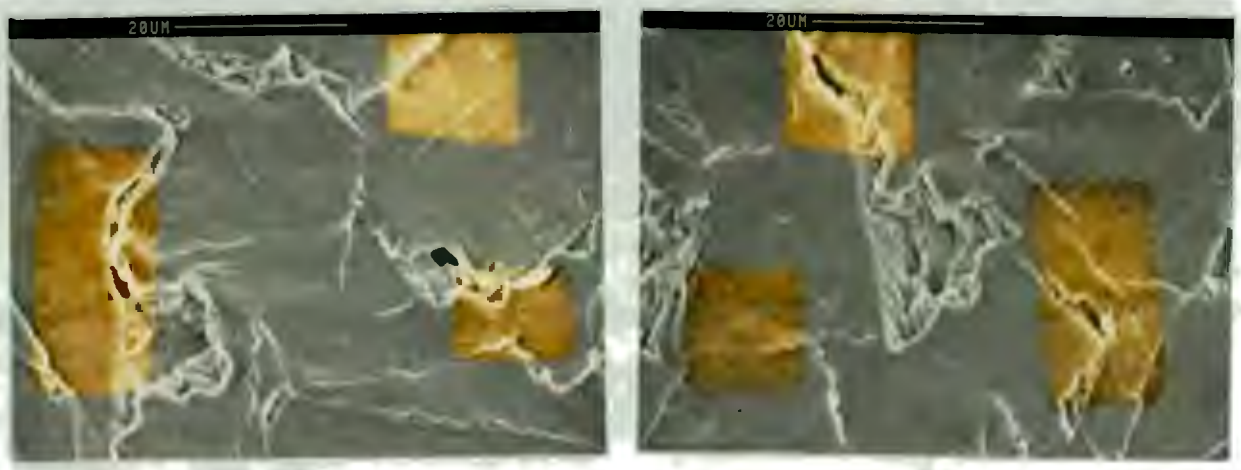

(a) (b)

Figure 5.56: Annealed 852 cavitated for 4 hours has further large scale removal of material from the grain boundaries (a), and the removal of material to a smaller extent from the slip lines within the grains (b).

Figure 5.57: Annealed 852 cavitated for 5 hours shows extensive material removal at grain boundaries and within the grains.

It is at this stage, after about 5 hours, that the cavitation progresses to the steady state regime and the surface becomes progressively more worn and irregular. The topography of the eroded surface after 12 hours of cavitation is shown in the micrograph in Figure 5.48.

5.8.1.2 Cavitation of 852 with 16% cold deformation

Figure 5.58: 852 with 16% cold reduction and cavitated for 0.5 hours, there is the removal of some of the harder ferrite phase but no other material is eroded or displaced.

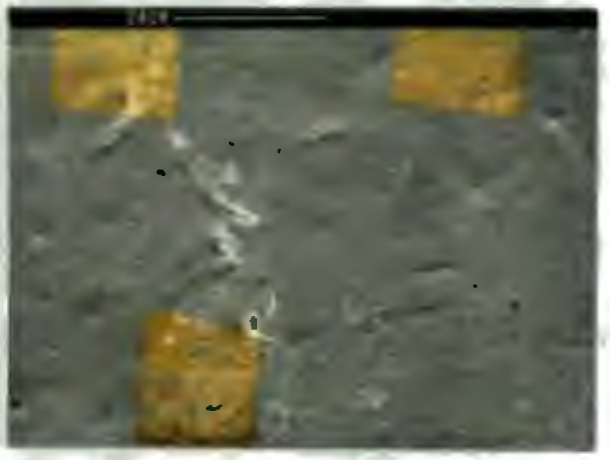

Figure 5.59: 852 with 16% cold reduction and cavitated for 1 hour. The erosion of ferrite is seen in the micrograph. Slip lines are manifest within the grains.

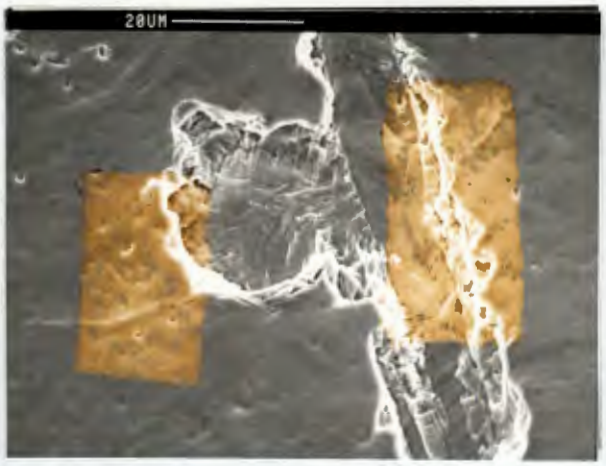

Figure 5.60: 852 with 16% cold reduction and cavitated for 1½ hours. The long darker piece is the ferrite area where material was first removed. The rounded cavity shows the area where material has been removed by fatigue.

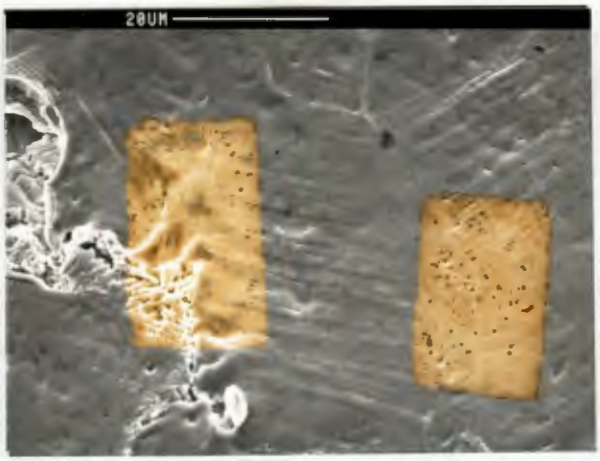

Figure 5.61: 852 with 16% cold reduction and cavitated for 2 hours. The area of ferrite is to the left of the micrograph whilst the rest of the micrograph shows slip lines.

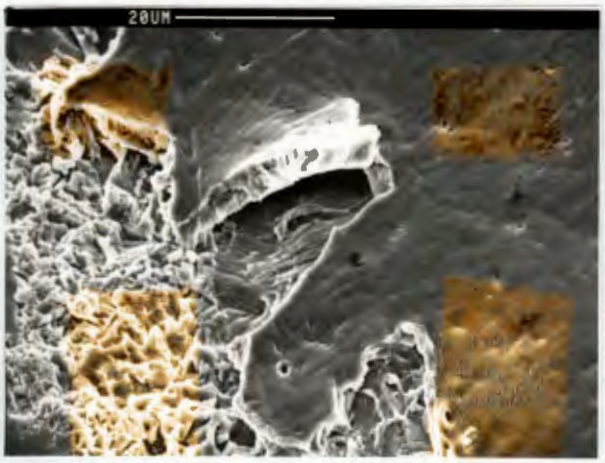

Figure 5.62: 852 with 16% cold reduction and cavitated for 3 hours. An area of material being removed by the propagation of a crack into the material. This crack is propagated by the cyclic stress of the bubbles imploding. The crack has been initiated at the ferrite-austenite interface.

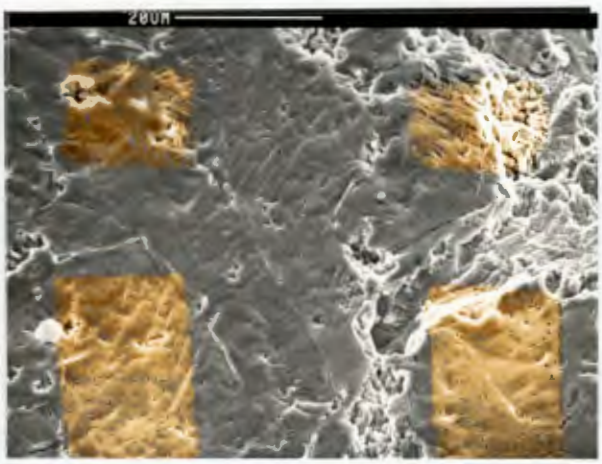

Figure 5.63: 852 with 16% cold reduction and cavitated for 4 hours. There are some areas of ferrite where material has been removed while the other areas are showing slip and erosion at the grain boundaries.

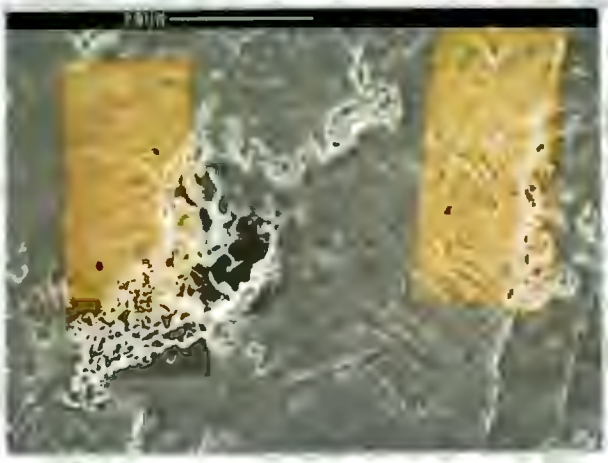

Figure 5.64: 852 with 16% cold reduction and cavitated for 5 hours. The ferrite areas are eroded and there is severe slip within the grains. There is material loss from the grain boundaries.

Figure 5.65: 852 with 16% cold reduction and cavitated for 6 hours. The onset of the steady state, as evidenced by large scale dimpling and an irregular surface.

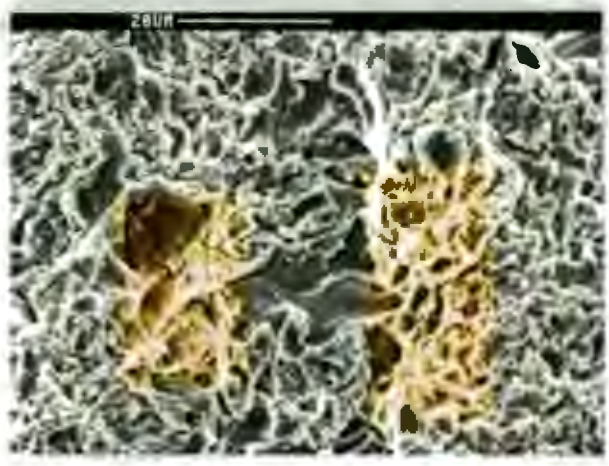

Figure 5.66: 852 with 16% cold reduction and cavitated for 12 hours. The same features as can be seen in the annealed material cavitated for 12 hours. There is an irregular dimpled surface and material is lost by the propagation of micro-cracks into the surface of the material.

5.8.1.3 Cavitation of 852 with 66% cold deformation

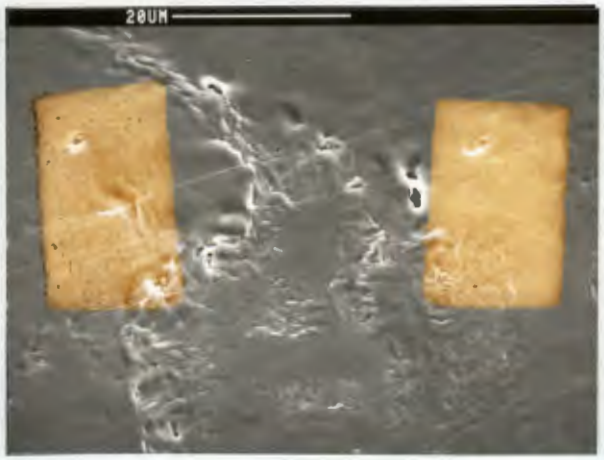

Figure 5.67: 852 with 66% cold reduction and cavitated for 1 hour. The small scale erosion and loss of the brittle ferrite phase is apparent.

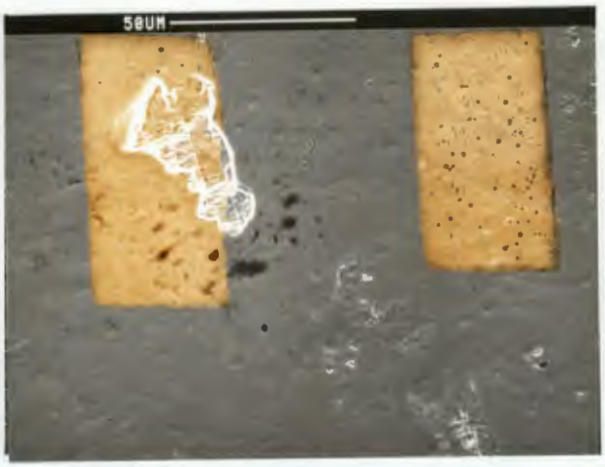

Figure 5.68: 852 with 66% cold reduction and cavitated for 1½ hours. This micrograph illustrates the continued erosion of ferrite and the removal of the adjacent austenitic material.

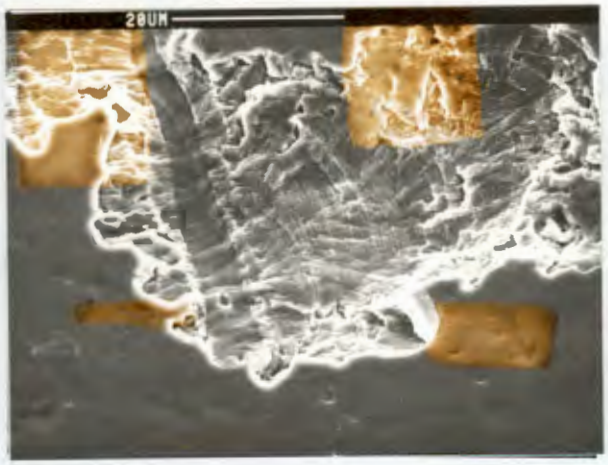

Figure 5.69: 852 with 66% cold reduction and cavitated for 2 hours. There are fatigue striations from areas where material has been lost.

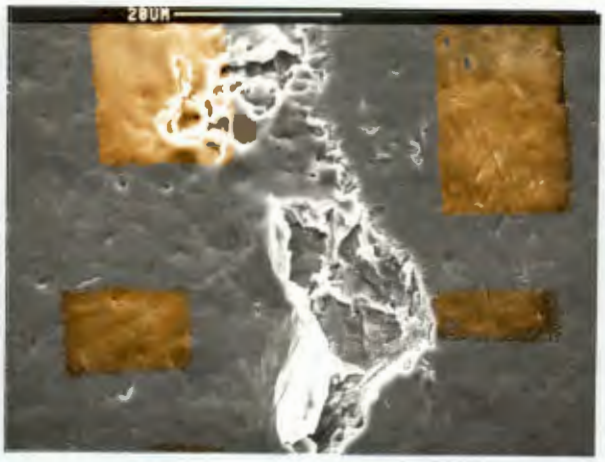

Figure 5.70: 852 with 66% cold reduction and cavitated for 3 hours.

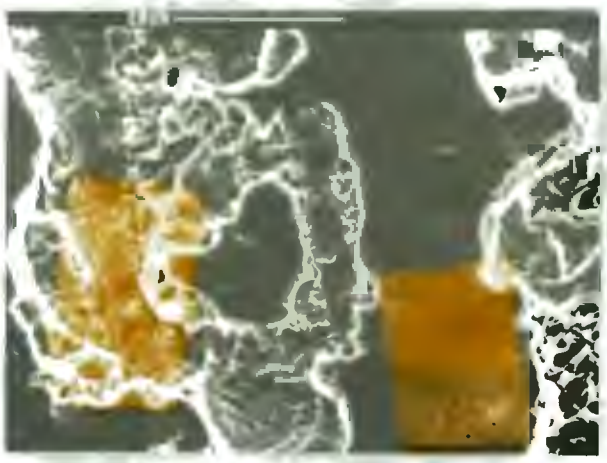

Figure 5.71: 852 with 66% cold reduction and cavitated for 4 hours. Material loss results in ferrite areas becoming connected.

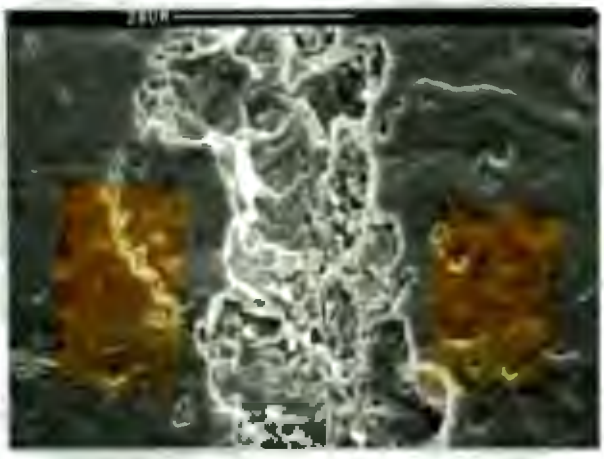

Figure 5.72: 852 with 66% cold reduction and cavitated for 5 hours.

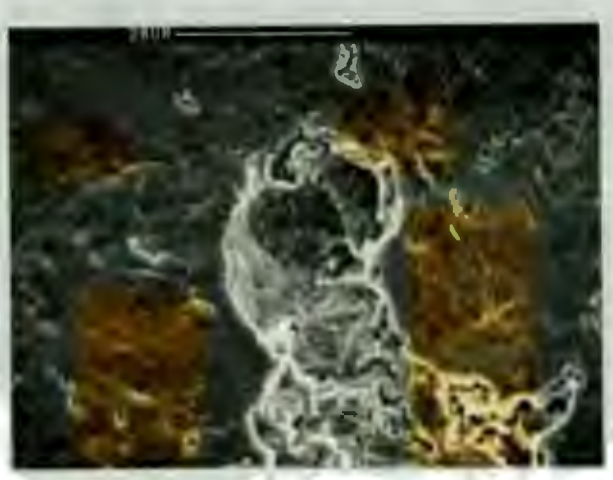

Figure 5.73: 852 with 66% cold reduction and cavitated for 6 hours. Some evidence of restricted slip within the grain boundaries is evident.

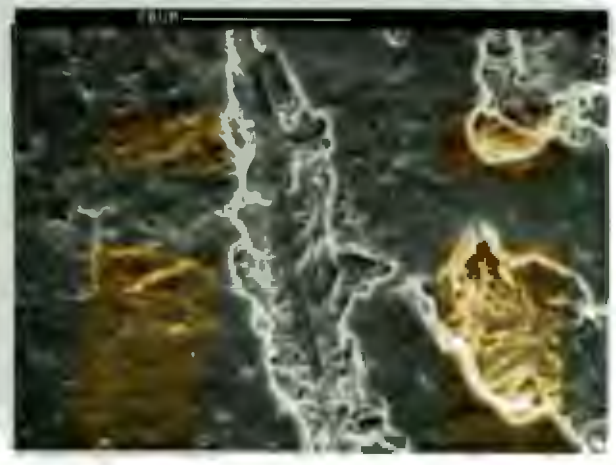

Figure 5.74: 852 with 66% cold reduction and cavitated for 7 hours.

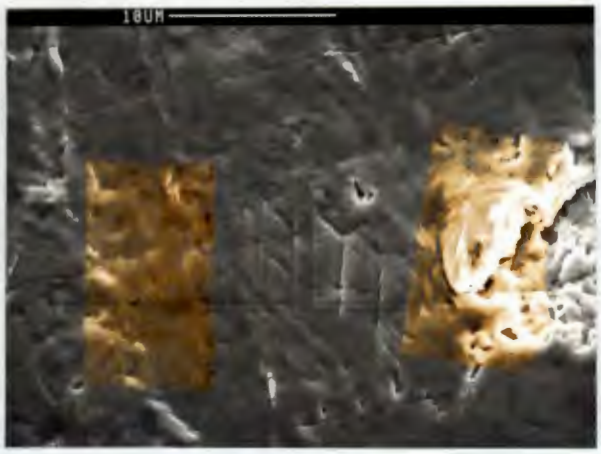

Figure 5.75: 852 with 66% cold reduction and cavitated for 8 hours. There is extensive slip occurring within the grain boundaries.

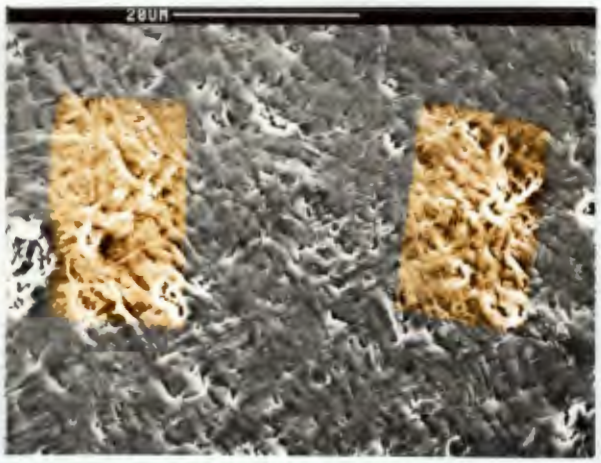

Figure 5.76: 852 with 66% cold reduction and cavitated for 9 hours. The previously uneroded surface is now completely dimpled and pock marked.

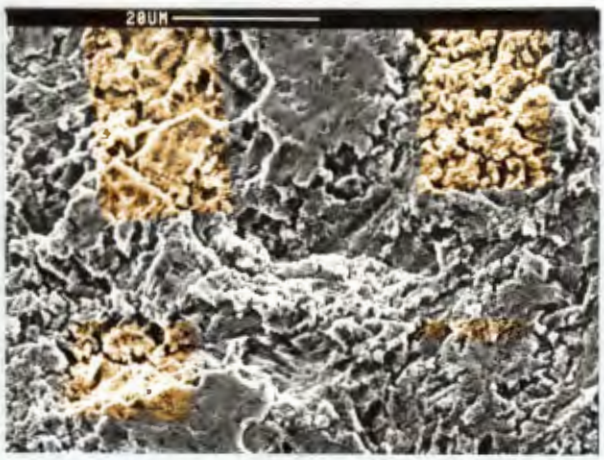

Figure 5.77: 852 with 66% cold reduction and cavitated for 12 hours. The surface looks very similar to the other cold worked states after 12 hours of cavitation.

5.9 X-Ray Diffraction

XRD was performed on the cavitated specimens to investigate whether any phase transformation took place after cold deformation and after cavitation. Each of the cold rolled specimens were scanned before cavitation and then again after cavitation. In this way it is possible to measure the amount of martensite present after rolling and before cavitation. The scan after cavitation then reveals the amount of transformed material after cavitation. The graphs of intensity against 2θ angle are presented in this section. These graphs give a qualitative representation of the change in microstructure. No quantitative calculations have been executed. It must also be remembered when looking at these graphs that the texture effects have not been considered as only a qualitative appreciation of the amount of martensite present is required.

5.9.1 XRD of annealed 852

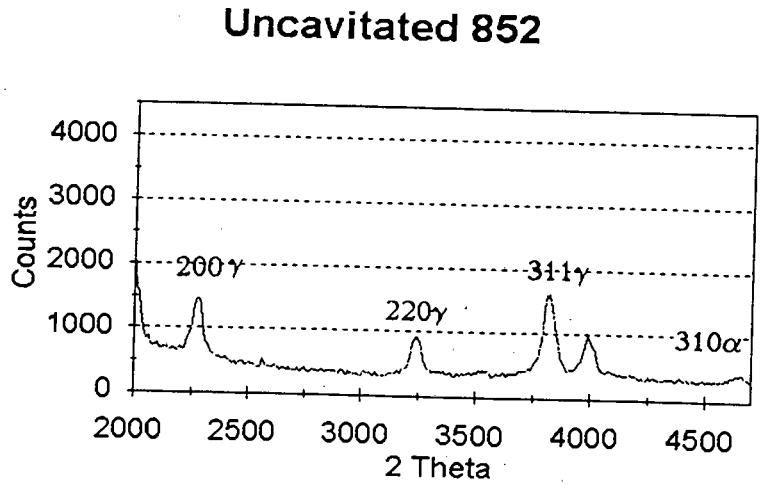

Figure 5.78: An XRD trace of uncavitated annealed 852.

In Figure 5.78 of uncavitated annealed 852 there is no trace of martensite. There is a small peak at the 2θ angle of 45.96° which is indicative of the presence of the 310α'

bcc martensite plane. This peak is very small with respect to the austenite peaks and it is therefore no confirmation of martensite.

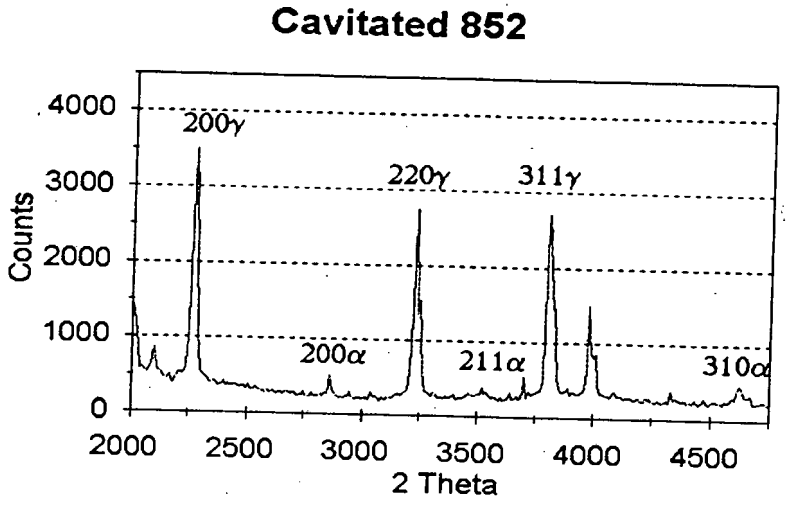

Figure 5.79: An XRD trace of cavitated annealed 852.

From Figure 5.79 there is clear evidence of a small transformation of austenite to martensite in annealed 852. This apparent transformation is very slight and could be attributed to the ferrite or the orientation of the specimen in the XRD chamber.

5.9.2 XRD of 852 with 16% cold deformation

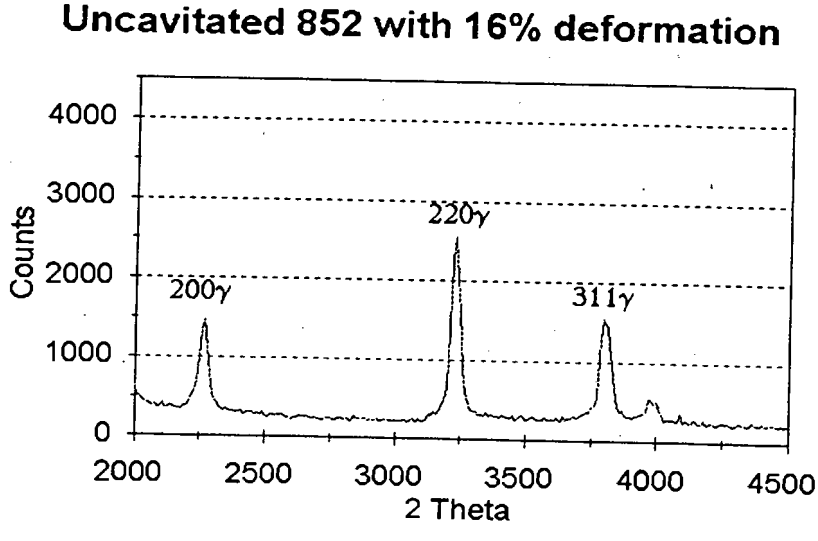

Figure 5.80: An XRD trace of uncavitated 852 after 16% deformation.

Figure 5.80 shows that with cold deformation of 16% there is no transformation to martensite.

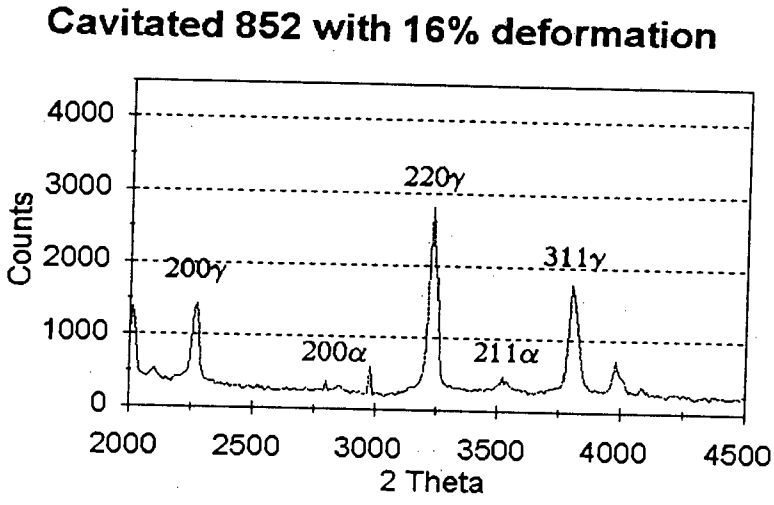

Figure 5.81: An XRD trace of cavitated 852 after 16% deformation.

After cavitation of 852 with 16% deformation there are signs of a transformation to martensite as indicated by the 200α' and 211α' peaks.

5.9.3 XRD of 852 with 30% cold deformation

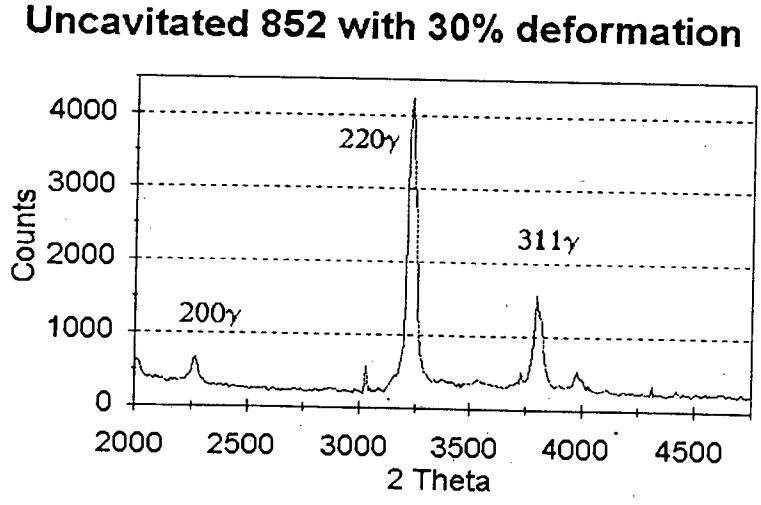

Figure 5.82: An XRD trace of uncavitated 852 after 30% deformation.

The trace of uncavitated 852 with 30% deformation shows no signs of martensite.

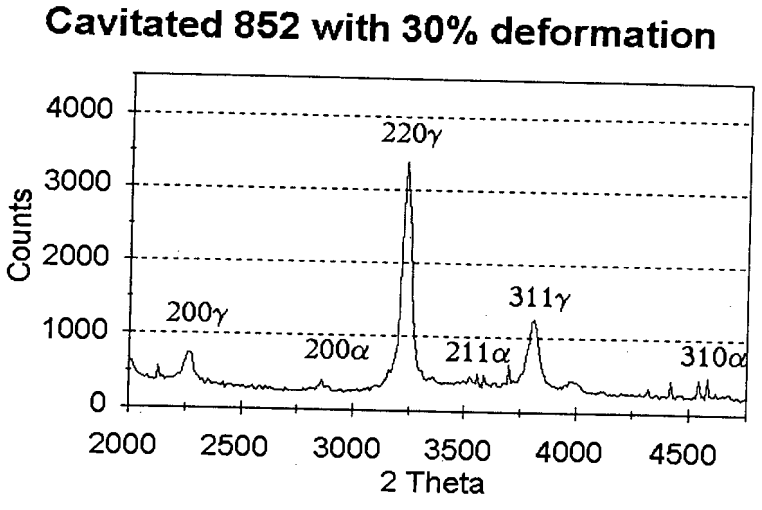

Figure 5.83: An XRD trace of cavitated 852 after 30% deformation.

After cavitating the 852 accommodating 30% deformation there is again partial evidence of a slight phase transformation. A transformation of this magnitude would have a small effect on the cavitation resistance of the material.

5.9.4. XRD of 852 with 48% cold deformation

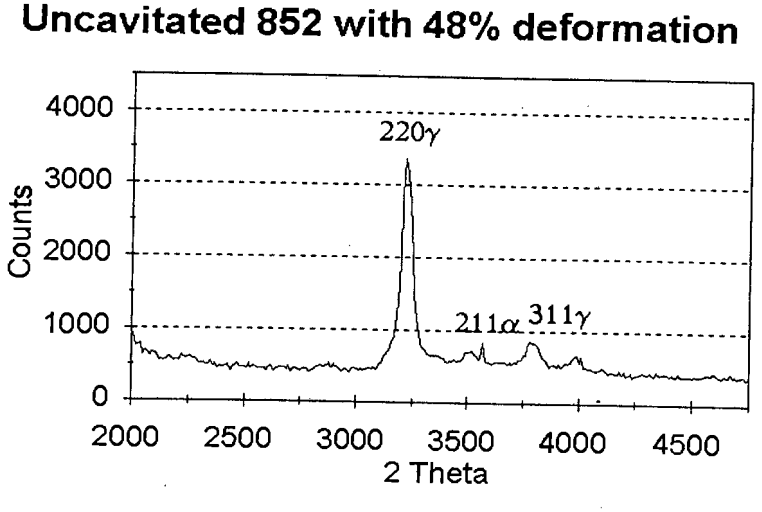

Figure 5.84: An XRD trace of uncavitated 852 after 48% deformation.

Figure 5.85 reveals that after a 48% cold reduction there is a small amount of martensite present. This is exposed by the 211α' bcc martensite plane.

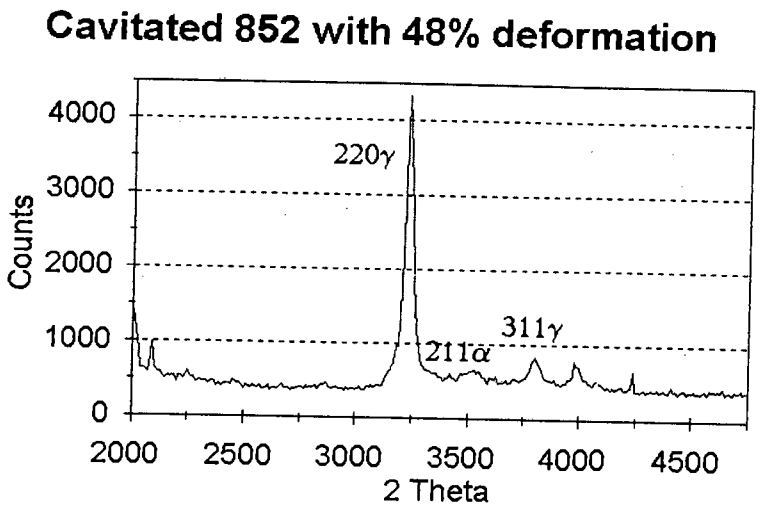

Figure 5.85: An XRD trace of cavitated 852 after 48% deformation.

There is little change in the shape of the spectrum after cavitation, except for the slight intensity increase in the 211α' bcc martensite peak.

5.9.5. XRD of 852 with 16% cold deformation

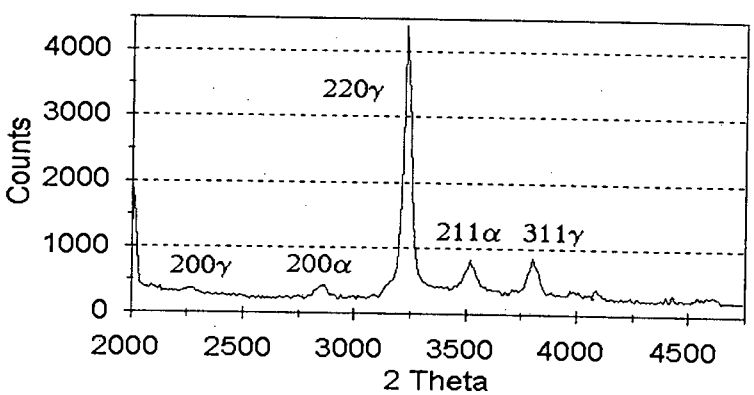

Figure 5.86: An XRD trace of uncavitated 852 after 66% deformation.

Figure 5.86 shows an increase in the amount of martensite present. This is borne out by the increase in intensity of all three of the distinctive martensite peaks. From this XRD plot it is evident that after 66% deformation there is a transformation to martensite.

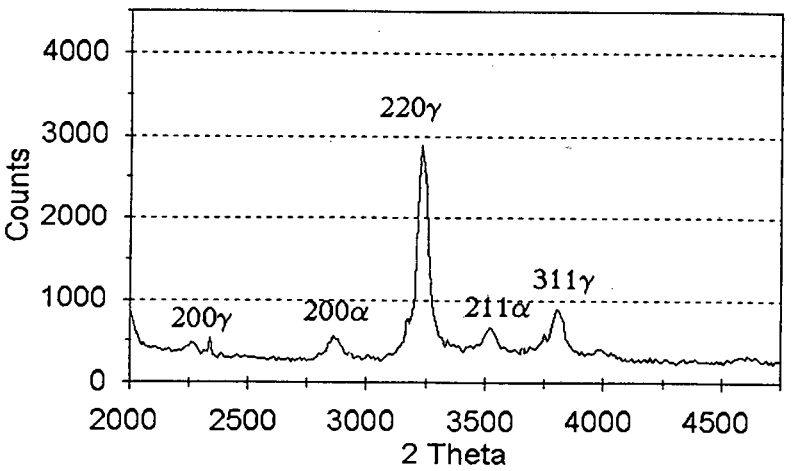

Figure 5.87: An XRD trace of cavitated 852 after 66% deformation.

There is no large change in the structure of the material after cavitation of the most highly deformed material. The majority of the martensite present is the same martensite that was present before cavitation.

5.10 Transmission Electron Microscopy (TEM)

TEM was performed to obtain a qualitative check on the dislocation structure occurring in the annealed and cold worked high nitrogen steel. The dislocation structure is compared by imaging thin film specimens taken from the annealed and cold rolled specimens.

Figure 5.88: TEM micrograph of annealed 852, showing a twin and partial dislocations as would be expected in a low SFE alloy like 852.

Figure 5.89: TEM micrograph of cold rolled 852 to 16% reduction, with the triangular dislocation sub-cell structure indicating planar slip.

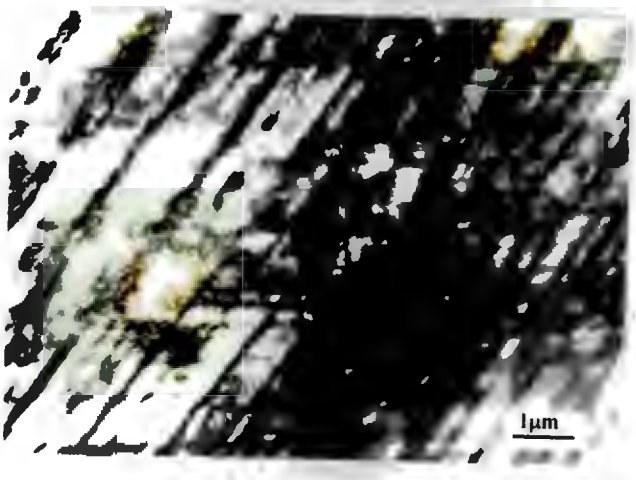

Figure 5.90: TEM micrograph of cold rolled 852 to 30% reduction, with a greater amount of planar slip.

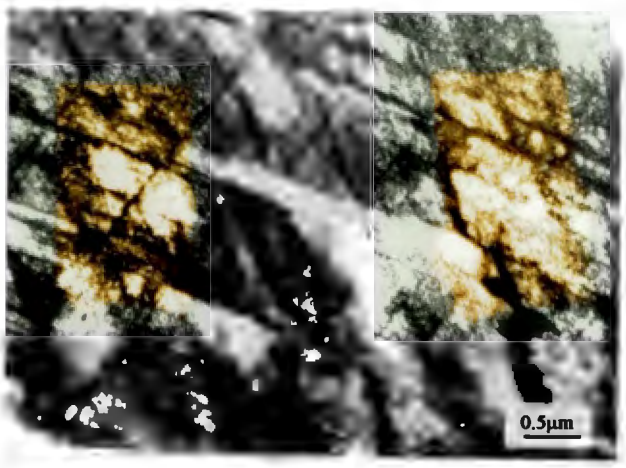

Figure 5.91: TEM micrograph of cold rolled 852 to 48% cold reduction showing further planar slip and a much higher dislocation density.

5.11 Cavitation of a Vanadium Micro-alloyed Steel

Temperature (°C)	Ageing Time (hrs.)	Incubation Time (hrs.)	Steady State Erosion Rate (mm^3hr^{-1})
700	0	3.6	0.05
	0.5	4	0.04
	2	4.5	0.03
	8	4.4	0.03
900	0	3.6	0.05
	0.5	4.8	0.05
	2	4.5	0.05
	8	4.3	0.06

Table 5.8: The incubation time and steady state erosion rates of the vanadium micro-alloyed steel aged at 700°C and 900°C for different times.

In Figure 5.92 we see that the incubation time increases with ageing time at 700°C, this is in contrast to the behaviour at 900°C where there is an increase in the incubation time after 0.5 hours followed by a decrease. The steady state erosion rate decreases when the material is aged at 700°C but remains constant when aged at 900°C.

5.11.1. The effect of ageing time and temperature on the incubation time of the vanadium micro-alloyed steel.

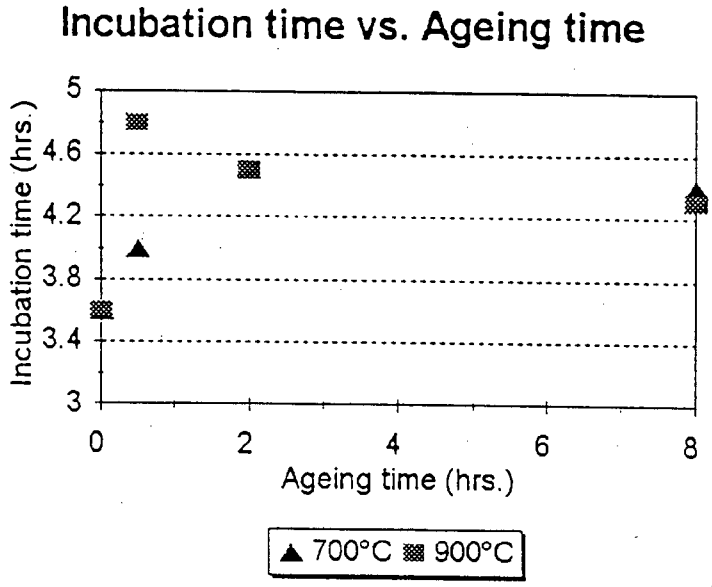

Figure 5.92: The effect of ageing time at 700°C and 900°C on the cavitation erosion incubation time of the vanadium micro-alloyed steel.

There is a rapid increase in the incubation time after ageing at 900°C for half an hour, after which time the incubation time slowly decreases. When ageing at 700°C the incubation time increases and then levels off after 2 hours of ageing. Both ageing treatments result in the material having the same incubation time after 8 hours of ageing. This behaviour can be correlated to the microstructural evolution. At 700°C the ferrite grains were completely transformed to cellular precipitate after ageing for 8 hours. It is also after 8 hours of ageing at 700°C that the material has the longest incubation time. At 900°C the ferrite has been completely transformed to cellular precipitate after 2 hours of ageing and this is also when the material has the longest incubation time.

5.11.2. The effect of ageing time and temperature on the steady state erosion rate of the vanadium micro-alloyed steel.

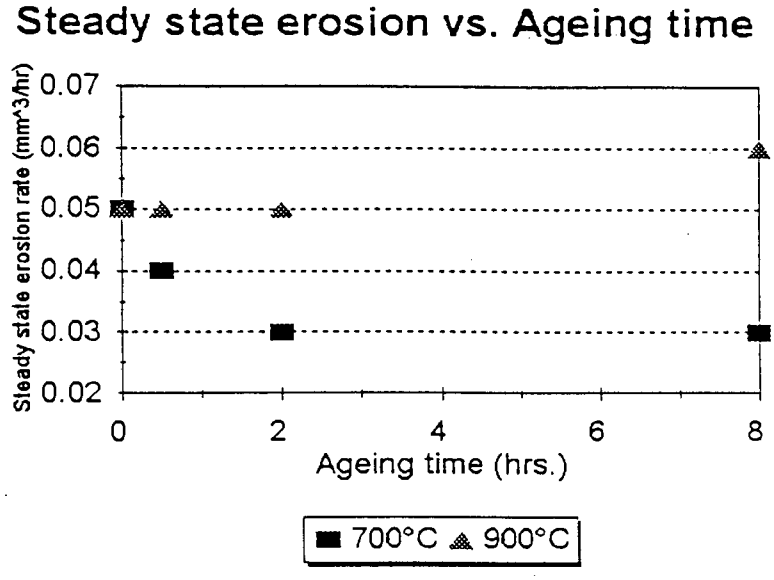

Figure 5.93: The effect of ageing time on the steady state erosion rate of the vanadium micro-alloyed steel.

After ageing at 700°C the material has improved cavitation erosion resistance, this improvement levels out after ageing for times longer than 2 hours. The material aged at 900°C shows a slight increase in the erosion resistance which then remains constant until being aged for longer than 2 hours after which the erosion rate increases. The formation of cellular precipitates in the ferrite grains at 700°C apparently improves the steady state erosion rate. Ageing at 900°C has no effect on the steady state erosion rate until the alloy has been aged for longer than 2 hours. This could be related to grain growth and an increase in the grain boundary density after ageing for longer than 2 hours at 900°C.

6. DISCUSSION

This thesis investigates the tribological behaviour of a stable high nitrogen manganese austenitic stainless steel and the effect of different thermal and mechanical treatments on the wear of this steel as well as the wear behaviour of vanadium micro-alloyed steel. These tests were done with comparison to Hadfields manganese steel, AISI 304 and AISI 316.

Section 3.3, which reviews the relevant literature, details how the mechanical properties of a stainless steel are affected by the addition of nitrogen. The results section indicates that there is indeed a corresponding improvement in the abrasion, abrasion-corrosion and cavitation erosion resistance of the steel. This section explains and expands on the improvements that are noted in the results section.

6.1. Abrasion

From the literature [55, 58, 59, 60] it is clear that little progress has been made in correlating the mechanical properties to the abrasion resistance. The main reason for this is that abrasion is a function of the abrasion system and not the material being abraded. The comparisons we make in this thesis between the different materials are all made from results obtained on the same abrasion system. The other materials parameters which are important are *inter alia* hardness (of abrasive and material), yield strength and work hardening rate. All materials, depending on these factors, respond differently to the effect of an abrasive. The results that were obtained from the work done for this thesis when comparing 852 with AISI 304, AISI 316 and Hadfields manganese steel are shown in section 5.5.

This discussion will explain why Hadfields manganese steel has superior abrasion resistance followed by 852 and then AISI 304 and AISI 316. It has been proposed that a material owes it abrasion resistance to its surface hardness.[58] In the case of comparing 852 with Hadfields manganese steel this would only be partially true since there is no great difference between the surface hardness of the two alloys although there is a marked difference in the abrasion resistance.

It is proposed in this thesis that for a material to have a high abrasion resistance a combination of two energy absorbing mechanisms are necessary; namely a stress induced transformation from austenite to martensite and a high work hardening rate. It is therefore considered that Hadfields manganese steel owes its abrasion resistance to both a partial transformation of austenite to martensite and work hardening due to the low stacking fault energy. The high nitrogen alloy 852 has a lower abrasion resistance than Hadfields manganese steel. The reason for this is that alloy 852 absorbs all the energy from the abrasion process by slip and work hardening. There is no evidence of a martensitic transformation to aid in the abrasion resistance process. This lack of transformation was not measured directly but was assumed from the shape of the work hardening rate vs. strain curve presented in Figure 5.25, which reveals no transformation indicative peaks in the curve, and from the XRD results in section 5.9. These XRD results were recorded from cavitation eroded specimen and even though the stress strain configuration is different there is no sign of the martensitic transformation.

When in an abrasive environment AISI 304 undergoes a considerable amount of $\gamma \rightarrow \alpha'$ shear transformation. This shear transformation would be able to accommodate high stresses but cannot accommodate the high strains associated with abrasion; it therefore has worse abrasion resistance than AISI 316 which does not transform to as great an extent and is therefore able to accommodate the higher strains. From these observations an abrasion resistant material must have a low stacking fault energy i.e. a high work hardening rate and the ability to undergo a small amount of $\gamma \rightarrow \alpha'$ shear transformation.

The model of Krushev and Babichev can be applied to the abrasive wear of the steels tested in that there is the formation of plastically deformed lips and the separation of work hardened particles in the form of microchips [51]. This is borne out by the SEM micrographs of the wear surface (Section 5.5) It is clear from these micrographs that the differences in the abrasive wear results of the steels can in no way be ascribed to differences in the wear topography as imaged on the SEM. All the micrographs of the wear surfaces show very similar features with the implication that the mode of failure is the same.

The cold worked material alloy 852 showed a steady decrease in the abrasion resistance with an increase in the hardness caused by an increasing amount of prior cold deformation. This apparent contradiction is explained by the model presented above in that the abrasion resistance of the material lies in its ability to absorb energy and to work harden. The shear lips and sub-surface areas in the annealed material are able to accommodate more strain than in the deformed material. The deformed material will therefore loss material more readily under abrasion conditions than the annealed material. When in contact with previously deformed material the abrasive is still going to penetrate the material, i.e. the stress imposed by the abrasive strike will always be above the yield stress of the material, so the material, where possible will plastically deform and work harden. The amount of strain the abraded material can accommodate will depend on the amount of cold work the material has accommodated prior to abrasion. When a material is abraded in the annealed state it is able to accommodate far more abrasion than a cold worked material. Thus is the abrasion resistance related to the inverse of the amount of prior cold deformation.

The vanadium micro-alloyed steel shows good abrasion resistance in the homogenised state. Its relative abrasion resistance lies between that of Hadfields manganese steel and alloy 852. The SFE of the alloy is expected to be low. This is assumed after considering the literature reviewed in section 3.4.5 which reveals that an increase in nitrogen content causes a decrease in the SFE and therefore an increase in the work hardening rate. The austenite structure is expected to be stable considering the stabalizing effect of the high nitrogen and the nickel contents. It is therefore considered that no transformation will occur in this alloy under abrasionconditions. The graphs in Figure 5.30 and Figure 5.31 show how the abrasion resistance of the alloy changes as a function of the ageing time and hardness. There is virtually no improvement noted despite there being a change in the hardness as shown in Figure 5.22 and Figure 5.23. This implies that the ageing process induces microstructural changes which improve the hardness but have no effect on the abrasion resistance. The microstructures in Figure 5.10 and Figure 5.20 indicate that ageing at 700°C and 900°C causes an increase in the amount of cellular precipitation present. Under static loading, as in hrdness tests, the cellular precipitation improves the properties, but under dynamic abrasion conditions the cellular precipitate has no effect. No evidence of any preferential removal of cellular precipitates was observed on the SEM micrographs in Figure 5.32 to Figures 5.38 of

the wear surfaces. Considering the high stresses and strains imposed by the abrasion process it is assumed that the abrasive would plough through both the precipitate and the matrix and an increase in the amount of precipitate present would not reduce the material loss. Further investigation will be necessary to obtain a better understanding of the effect of ageing on both the precipitation reactions and the abrasion resistance. A TEM study was performed on the aged vanadium micro-alloyed steel but the imaging of precipitates proved to be elusive and the TEM study produced no concrete results.

6.2. Abrasion-Corrosion

The abrasion-corrosion test was used to arrive at a comparison between the abrasive-corrosive wear of the materials. It transpired that only comparisons between the different materials could be made as the test was not sensitive enough to distinguish between the same material in different conditions. It was not possible to measure any accurate differences between the various cold worked and heat treated materials. The test results are all quoted as wear resistance relative to mild steel as the results can then be compared to those obtained by other workers. The results obtained indicate that alloy 852 is 3.14 times better than mild steel while AISI 304 and AISI 316 have similar abrasion-corrosion resistance at 2.73 and 2.60 times better than mild steel. The poorest performer was Hadfields manganese steel at 1.43 times better than mild steel. The value of 2.73 for AISI 304 compares well with the value of 2.88 obtained by Barker [56]. Barker obtains values in the order of 3.14 and higher for a number of other wear resistant steels. The steels for which Barker obtained these values are high alloy martensitic steels with added heat treatments. The high nitrogen alloy has the benefit of being in the as received condition with no complicated heat treatment required to improve the properties. It also remains fully austenitic and should consequently remain non-magnetic.

It is now pertinent to discuss the value of a corrosive resistant steel in an abrasive environment. The corrosive medium used in the abrasion-corrosion test was a very mild acid with a pH of 6.5 to 7.0 at the start of a test. The solution was obtained after an analysis of mine water found in a Transvaal gold mine [71]; it is therefore highly probable that most earth

working equipment is exposed to corrosive water of this nature when used in mines. It is also probable that the water in specific areas is more corrosive than that used in this test solution or that the metal gets exposed to the corrosive medium for longer periods of time depending upon the application. In such a situation it would be highly inadvisable to use an exclusively wear resistant steel. This is highlighted by the results obtained for Hadfields manganese steel. In pure abrasion conditions the volume loss is 0.70 $mm^3.m^{-1}$, but when the abrasion is interrupted by corrosion the volume loss increases to 2.02 $mm^3.m^{-1}$. This is in sharp contrast to the results obtained for alloy 852 where the volume loss due to abrasion was 0.91 $mm^3.m^{-1}$ and then increased marginally to 0.92 $mm^3.m^{-1}$ when subjected to intermittent corrosion. It is believed that this very small change in the volume loss could be due to the removal of abraded swafs of material by the flow of the corrosive medium over the abraded surface.

The corrosion resistance of alloy 852 can be ascribed to the high chromium content which causes a passive layer to form at the abraded surface. This is illustrated by the fact that the stainless steel maintains its shiny, 'rust' free surface during the corrosion cycle. On the other hand the abraded surface of Hadfields manganese steel becomes highly 'rusted' and discoloured after a short period of abrasion. This iron oxide is then removed from the surface upon subsequent abrasion.

The stainless steels AISI 304 and AISI 316 have slightly higher volumes losses, i.e. lower abrasion-corrosion resistance, than alloy 852. This is due to the differences in the abrasion resistance. The graphs in 5.41 and Figure 5.43 show that the corrosion component has very little influence on the volume loss.

6.3. Cavitation

The cavitation erosion process is the process which received the most attention in the thesis and the effect of cavitation erosion rate of a high nitrogen manganese austenitic stainless steel will be discussed in this section. The effect of cold deformation is discussed and a model which represents this cavitation process is presented. The improvement in the cavitation resistance due to strain ageing treatments are also considered.

The relative cavitation erosion resistance of the high nitrogen manganese austenitic stainless steel is considered first. The cavitation erosion rate of the high nitrogen manganese austenitic stainless steel is compared with that of Hadfields manganese steel, AISI 304 and AISI 316. The results listed in Table 5.6 indicate that the high nitrogen stainless steels, both the stable austenitic steel alloy 852 and the vanaduium micro-alloyed steel, alloy 811, have the best cavitation erosion resistance with respect to both the incubation period and the steady state cavitation rate. The next best performer is AISI 304, then Hadfields manganese steel and finally AISI 316. The performance of the high nitrogen manganese austenitic sr\tainless steel and the vanadium micro-alloyed steel is compared to Hadfields manganese steel, AISI 304 and AISI 316 in terms of the cavitation erosion resistance.

It has been reported by other workers that Hadfields manganese steel has the best cavitation erosion resistance of all the austenitic steels tested[87]. This is ascribed to Hadfields manganese steel having a higher work hardening rate than AISI 304[88]. The results of this thesis indicate that alloy 852 has better cavitation erosion resistance than Hadfields manganese steel. There are two factors that we believe could account for this, firstly, the exact alloy composition of the Hadfields manganese steel used could be different to that used by other reaserchers and, secondly, the state in which the material is tested could be different. Hadfields manganese steel has a low incubation period and a steady state erosion rate marginally worse than that of AISI 304. It is also possible that Hadfields manganese steel could corrode in the water in the cavitation test bath and this would add to the cumulative material loss of Hadfields manganese steel as it has no inherent corrosion reisitance. This

factor would not be a concern when testing stainless steel but would certainly be relevant when testing steels with no chromium content.

The large differences in the cavitation erosion resistance of AISI 304 and AISI 316 are ascribed to the differences in the transformation behaviour of the two alloys. The mechanical properties of the two steels are similar but their cavitation erosion properties are different. In AISI 304 cavitation produces a considerable transformation of γ (austenite) to α' (martensite). This transformation is not present to such a large extent in AISI 316[89]. The M_{d30} temperatures also allude to the fact that AISI 316 is more prone to transformation than AISI 304. The energy caused by the cavitation process is used to transform the austenite to martensite in the AISI 304 steel and this occurs to a lesser extent in AISI 316 resulting in more energy being available to cause material loss.

The following section explains the good cavitation erosion resistance of the high nitrogen stainless steel. One of the first factor to consider when assessing cavitation erosion resistance is the work hardening rate. The work hardening rate of the alloy can be ascribed to either the $\gamma \rightarrow \alpha$' transformation of the material or to the stacking fault energy (slip behaviour) of the material. The transformability of the alloy is dealt with first. A good but limited measure of a steels propensity to transform is its M_{d30} temperature. The calculated M_{d30} temperature of alloy 852 is considerably lower than that of any of the other alloys tested. The M_{d30} temperatures of the alloys tested are presented in section 5.2, in the results section These results imply that alloy 852 will undergo no stress induced martensitic transformation. This has been verified by the XRD data obtained from this alloy. The XRD traces shown in Figure 5.95 to Figure 5.104 reveal that after 66% deformation (prior cold work) there is virtually no increase in the amount of martensite present. The shape of the slope of the stress strain curve vs the strain (Figure 5.25) has no peak which is characteristic of the formation of martensite. The high cavitation erosion resistance can therefore not be ascribed to the $\gamma \rightarrow \alpha$' transformation.

The other possible explanation for the good cavitation erosion resistance is the SFE and the way in which the SFE affects the movement of dislocations. The SFE of the high nitrogen

alloy 852 is lower than that of the other materials tested. Although no measurements have been made of the SFE of this alloy (852) the literature does attest to nitrogen lowering the SFE[35, 36]. As a consequence of the low SFE the partial dislocations are widely separated. This wide partial dislocation separation encourages planar glide, or slip, of dislocations and inhibits cross slip. As the strain in the material increases the dislocation density becomes greater and these dislocations act as barriers to further dislocation movement. The dislocations are also unable to cross slip and so cannot bypass the dislocation barriers. The TEM micrographs in the results section indicate the change in the dislocation structure with increased deformation. As the amount of cold work increases the planar array of dislocations become more dense. In the case of alloy 852 the high cavitation erosion resistance is ascribed to the SFE and not the transformation from $\gamma \rightarrow \alpha'$.

6.3.1. Cavitation Model

The model presented in the next section will discuss the progression of cavitation erosion with time. A schematic model has been constructed after a careful study of the SEM micrographs in the results section of this thesis. The initial state of the material is shown in Figure 6.1. The distinctive austenite grains with their annealing twins are clear. The rounded grains are the areas of ferrite. This surface would be flat when viewed under the SEM as it has not been etched and there are no topographical features.

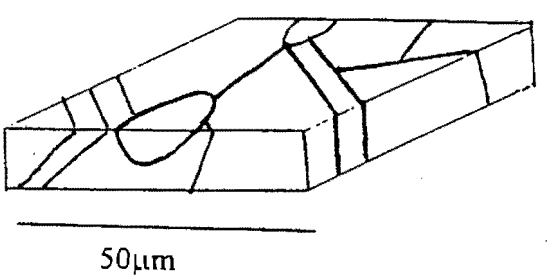

Figure 6.1: The surface of 852 before cavitation showing the austenite and ferrite grains.

As cavitation commences the material accommodates the strain by slip along the allowed slip planes in the fcc lattice. This slip can progress until it is stopped by crystallographic irregularities which are, in this case, the grain boundaries. Figure 6.2 shows the grain boundaries which are slightly raised from accommodating the slip after 30 minutes of cavitation. The slip lines on the surface are also evident. The ferrite areas are the first to be removed as this schematic illustrates.

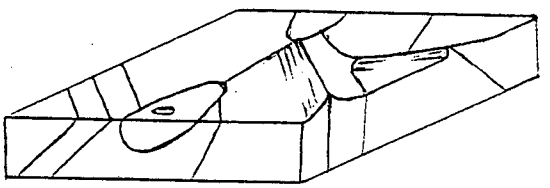

Figure 6.2: The surface after 30 minutes of cavitation. There is raised material at the grain boundaries and the ferrite is the first material to be removed.

After 1 hour the raised material protrudes from the surface and becomes exposed to the liquid jets and stress pulses of the cavitation process. There is small scale removal of material from the grain boundaries whilst the other grain boundaries accommodate slip and are raised. This is illustrated in figure 6.3. The ferrite continues to be removed at a greater rate than the austenite. The reason for this is that the ferrite has a bct structure as opposed to the fcc structure of austenite. This difference in crystal structure leads to differences in response to the stress imposed by cavitation and to a weakening at the phase interface.

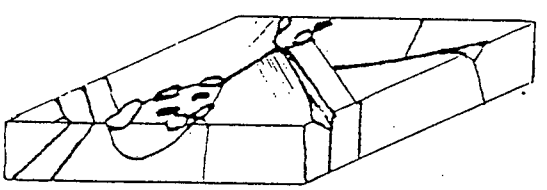

Figure 6.3: More material removed from the grain boundaries after 1 hour of cavitation. Ferrite gets removed at a greater rate.

After 90 minutes of cavitation erosion all the grain boundaries are raised and there is material loss from most of the grain boundaries. This stage is shown in figure 6.4. This material loss is due to fatigue. The cavitation process, as detailed in the schematics above, causes the grain boundaries to be raised. The imploding bubbles results in stress waves or jets of liquid with most of the stress being directed parallel to the surface. The raised grain boundaries are then subjected to a greater force than the flat surface. The removal of the raised grain boundary material is then caused by a fatigue process. The cyclic stresses which cause the fatigue are due to the cyclic implosion of bubbles. The fatigue process proceeds according to that outlined by Suresh [26] and is shown in section 3.3.3. The first step would be the creation of irreversible changes in the microstructure. In the case of cavitation erosion this would be the slip of dislocations. The second step is the formation of macroscopic defects (cracks) and these are evident on the SEM micrographs of cavitated material. This is followed by the subcritical growth of these cracks by the repetitive stress from the cavitation process. The fact that these cracks are growing subcritically is evident from the striations (or clam shell marks) on the surface. These marks are imaged on some of the SEM micrographs (Figure 5.55, Figure 5.60 and Figure 5.70). The exposed ferrite areas continue to be eroded at a greater rate than the austenite areas.

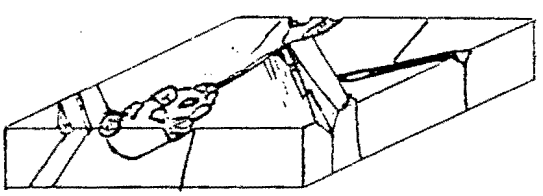

Figure 6.4: All the grain boundaries are raised whilst more material is lost at the grain boundaries and the loss of ferrite material continues. This schematic is a representation of the surface after 90 minutes of cavitation.

After 2 hours virtually all the grain boundaries have lost material (Figure 6.5.). The material loss now also continues within the crevices created by previous material loss. The irregular surface within these crevices are prime sites for trapping the water jets or stress waves from the imploding bubbles and so continue crack growth and material loss within the crevices. Ferrite is still being lost from within the ferrite grains. This rapid loss of ferrite continues until the austenite below the original ferrite grain has been reached. The erosion then slows down but the damage has been done since the surface is now highly irregular and erosion into the austenite can now continue at an accelerated rate.

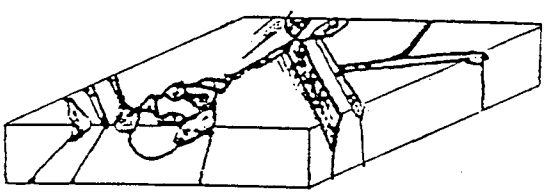

Figure 6.5: There is now material loss from within the crevices at the grain boundaries. Some of the original ferrite has been removed to expose the underlying austenitic. (After 2 hours)

After 3 hours all the ferrite that was originally exposed at the surface has been removed (Figure 6.6.). There is continued erosion from within the crevices at the grain boundaries. Most of the grain boundaries show material loss.

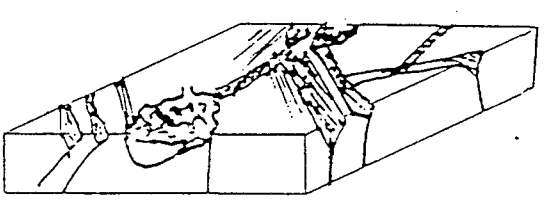

Figure 6.6: All the ferrite at the surface has been removed and material loss at the grain boundaries continues. (After 3 hours)

After 4 hours the majority of the exposed surface has lost material whilst the rest of the exposed surface area has become highly work hardened and topographically irregular (Figure 6.7.). Material starts to be lost from with in the austenite grains. The material loss from the ferrite areas continue.

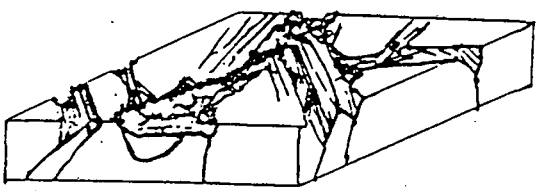

Figure 6.7: Most of the surface has been eroded. The eroded grain boundaries are beginning to meet and expose a greater area to further cavitation. (After 4 hours)

As testified by the incubation time results the steady state starts to set in after 4 hours. After 5 hours almost the entire surface area has been eroded (figure 6.8.). There is no perceivable difference between the initial ferrite areas and the initial austenite areas. The whole eroded surface consists of small dimples and the whole eroded area is highly irregular and therefore encourages erosion by cavitation.

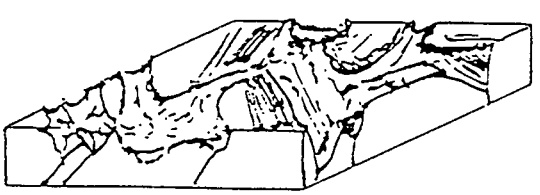

Figure 6.8: Almost the entire surface has been eroded and the steady state has been reached. (After 5 hours)

6.3.2. The Influence of Prior Cold Deformation

The next factor to consider is the effect of cold deformation on the cavitation erosion of the high nitrogen austenitic stainless steel 852. As outlined previously the material was cold worked to 16%, 30%, 48% and 66% cold deformation. Each of the specimens were then tested under cavitation erosion conditions. The results of this test are presented in Table 5.7. It is clear that the material with the highest amount of deformation has the best cavitation erosion resistance. With 66% cold deformation the material has an incubation time 1½ times longer and a steady state erosion rate 6¼ times better than the original annealed material. The incubation time will be dealt with first. As was outlined in the previous section the loss of austenite can only occur if there are raised areas above the surface of the material. For this to occur there needs to be plastic deformation and this deformation can only occur if the stress is high enough to deform the material. When this deformation does occur it is as a consequence of slip and deformation at the grain boundaries. As the TEM micrographs in section 5.10 indicate there is an increase in the slip dislocation density with increasing deformation. The dislocations act as barriers to further dislocation movement. The stress caused by the imploding bubbles at the surface first have to overcome the increased resistance to dislocation movement before deformation can occur. In other words the stress created by the imploding bubbles has to be higher than the yield strength and prior deformation increases the yield strength. The steady state erosion rate is reached when the majority of the surface has been eroded and the material loss is from these areas. The mode of material loss is one of microcracks growing into the crevices left by previously eroded material. The growth of these small cracks into the material is essentially a fatigue process as is shown on a number of the SEM micrographs in the results section. Fatigue is brought on by slip [27, 28] and the inhibition of slip will result in a decrease in the fatigue crack growth rate. The increase in the dislocation density below the surface will reduce the amount of slip and consequently increase the amount of cavitation erosion resistance. As concerns the strain ageing treatments, any process which decreases the mobility of the dislocations will increase the fatigue resistance and also increase the cavitation erosion resistance. This accounts for the decrease in the steady state erosion rate in the strain aged material (Table 5.7).

Finally, when discussing the erosion of this material it is important to remark on the effect of ferrite on the erosion rate. It is clear from the SEM micrographs that the ferrite is the first material to be removed. The reason for this is that ferrite is more brittle than austenite and is therefore less able to accommodate the strains, by plastic deformation, caused by cavitation. The areas from which ferrite has been removed are then more prone to further accelerated cavitation because of the irregular surface. It is thus important to keep the ferrite content as low as possible when attempting to improve cavitation erosion resistance.

The following section gives a schematic representation of the erosion process occurring when the cold worked material is cavitated. The two series of schematics represent the erosion of a material deformed to 30% and erosion of material deformed to 66%.

6.3.2.1. 30% Prior Deformation

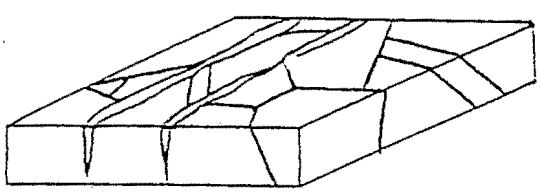

Figure 6.9: The polished surface before cavitation erosion. The ferrite bands can be seen and the austenite annealing twins show some signs of deformation.

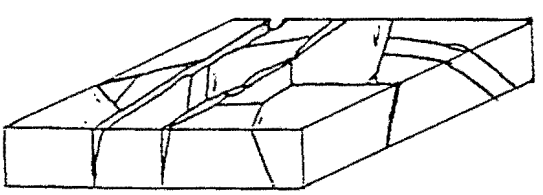

Figure 6.10: After 30 minutes the removal of ferrite is evident and slip is being accommodated by the austenite.

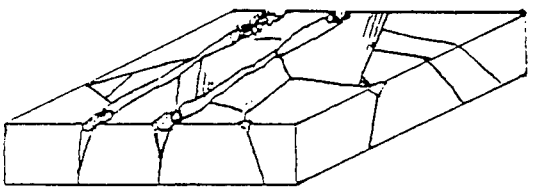

Figure 6.11: After 1 hour there is further erosion of the ferrite.

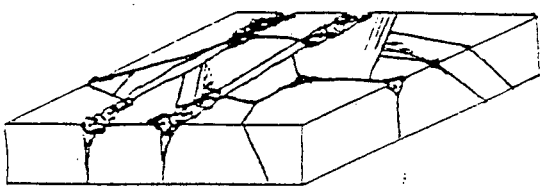

Figure 6.12: A schematic of the cavitated surface after 90 minutes showing further ferrite removal and slip in the austenite grains.

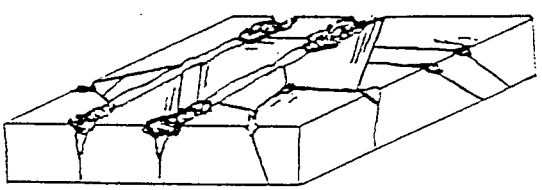

Figure 6.13: After 2 hours the removal of ferrite continues and there is also material being removed from the austenite areas adjacent to the ferrite.

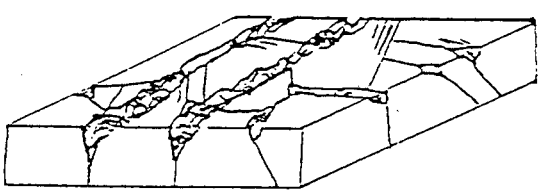

Figure 6.14: After 3 hours. there is severe erosion of the ferrite and the removal of material from the austenite grain boundaries.

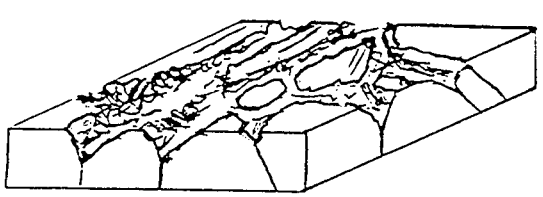

Figure 6.15: After 6 hours there is severe material loss and the entire surface is either deformed or material has been removed.

6.3.2.2. 66% Prior Deformation

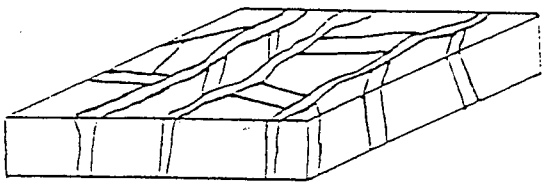

Figure 6.16: An area before cavitation where the ferrite bands are closer and the austenite grains show the accommodation of deformation.

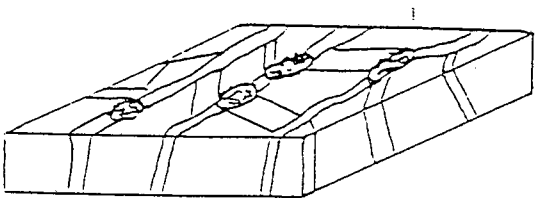

Figure 6.17: After 1 hour this schematic shows that ferrite is the first material to be removed.

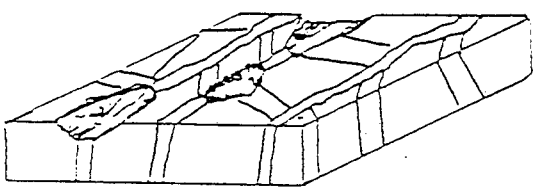

Figure 6.18: After 2 hours there is evidence of material removal adjacent to the removed ferrite.

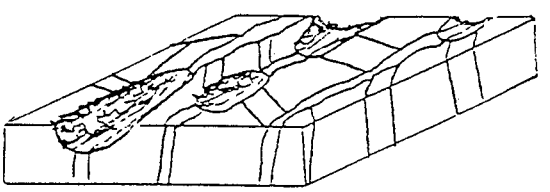

Figure 6.19: The surface after 3 hours of cavitation.

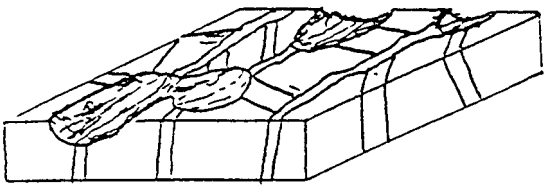

Figure 6.20: A schematic of the surface after 4 hours. There are areas of lost material linking the ferrite bands.

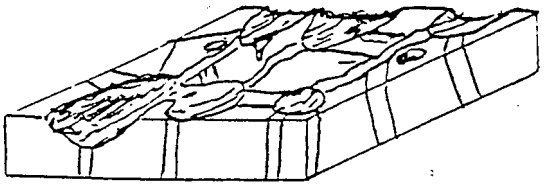

Figure 6.21: After 6 hours of cavitation there are signs of slip in the remaining austenite areas.

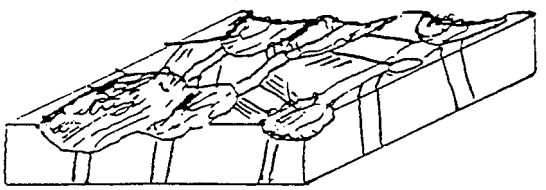

Figure 6.22: The steady state has been reached after 8 hours and there are large areas of eroded surface exposed to cavitation erosion.

6.3.2. The Vanadium Micro-alloyed Steel

The vanadium micro-alloyed steel showed an increase in the incubation time that was similar to the increase in the hardness associated with the precipitate reaction. When ageing at 700°C the longest incubation time is obtained after 2 hours of ageing. For ageing times longer than 2 hours the incubation time is found to decrease gradually. When ageing at 900°C the longest incubation time is obtained after 30 minutes. The incubation time decreases when ageing for longer than 30 minutes at 900°C.

The change in the steady state erosion rate was different to the change in the hardness and the change that was experienced by the incubation time. The steady state erosion rate deteriorated after ageing at 900°C and improvement after ageing at 700°C. The author will contend that the changes in the incubation time and the steady state erosion rate are due to the formation of cellular precipitate.

As concerns the incubation time there is an ageing time after which precipitates becomes so large that they are easily removed due to cavitation erosion at the matrix/precipitate interface. The longest incubation times are obtained when the precipitates are small enough not to expose large amounts of matrix/precipitate interface to cavitation, but large enough to increase the hardness and erosion resistance of the material. The peak cavitation erosion resistance is obtained after ageing at 900°C for 30 minutes at 700°C after 2 hours. With respect to the steady state erosion rate there is a marked improvement in the erosion rate after ageing at 700°C. This behaviour is partially mimicked by the erosion rate of the material aged at 900°C, in that the erosion rate decreases slightly and then increases. These results indicate that an increase in the amount of cellular precipitation causes an increase in the steady state erosion rate. The cellular precipitate is a harder and less ductile phase than the matrix austenite. The precipitate is therefore eroded faster than the austenite and has a detrimental effect on the cavitation erosion resistance.

7. CONCLUSIONS

The conclusions arrived at in this thesis are listed below. They concern the relative wear performance of the steels tested and the effect of thermal and mechanical treatments on the wear behaviour of the high nitrogen stainless steel and the vanadium micro-alloyed steel.

1. Hadfields manganese steel has the best dry abrasion resistance and this has been ascribed to its good work hardening rate. The nitrogen austenitic stainless steel has the next best abrasion resistance and the best abrasion resistance of all the stainless steels tested. This is because of the materials high work hardening rate as a result of its low stacking fault energy, its inability to cross slip and therefore its ability to resist plastic deformation.

2. The high nitrogen austenitic stainless steel displays the best abrasion-corrosion resistance. The abrasion component is good because of the reasons described in the section above. It outperforms Hadfields manganese steel because of Hadfields manganese steel's inability to resist corrosion. The high nitrogen stainless steel has corrosion properties similar to that of AISI 304 and AISI 316. When comparing these steels in terms of their abrasion-corrosion resistance the steels have similar corrosion resistance but alloy 852 has superior abrasion resistance.

3. Under cavitation erosion the high nitrogen stainless steel once again has better erosion resistance properties compared to the other materials. This is because of the materials hardness and work hardening rate being better than that of the other materials. The high nitrogen stainless steel has both a longer incubation time and a slower steady state cavitation rate. One of the reasons for the high nitrogen steel not having even better cavitation erosion resistance is the ferrite content and the fact that the ferrite areas are the first to be eroded. A further improvement can be made by reducing the ferrite content by an appropriately adjusted composition.

4. The vanadium micro-alloy steel has good abrasion resistance in the homogenised state, the abrasion resistance lies between that of Hadfields manganese steel and the high nitrogen alloy 852. Ageing treatments have very little effect on the abrasion resistance of this material. The abrasion corrosion resistance if the precipitation hardened alloy is the same as that for 852. As concerns the cavitation erosion resistance the incubation period lies between that of 852 and Hadfields manganese steel. The steady state erosion rate is the same as that for 852. Ageing heat treatments can increase the incubation period by about an 30%. When aged at 700°C the steady state cavitation erosion rate is decreased by 40 % and when aged at 900°C the steady state erosion rate increases slightly. Further work is needed on optimising the composition of these vanadium micro-alloy steels to obtain precipitation hardened high nitrogen stainless steel.

5. Prior deformation has a pronounced effect on the abrasion of the high nitrogen stainless steel. Increased deformation results in a decrease in the abrasion resistance despite an increase in hardness. It was found that strain ageing at 400°C for 2 hours has no effect on the abrasion resistance.

6. The cavitation erosion resistance is greatly improved by prior cold work. The incubation period increases by 1¼ times with 66% cold deformation and the steady state erosion rate decreases by 7 times with 66% deformation. Strain ageing at 400°C for 2 hours results in a partial improvement in the steady state erosion rate especially after deformation of 16% and 30%.

The conclusions indicate that high nitrogen stainless steel have excellent potential for use in high wear applications. There are a number of other tribological tests that this material can be exposed to and then compared with currently available materials. The tests are particle erosion, sliding wear, slurry erosion and high temperature particle erosion.

8. References

1. Honeycombe R.W.K., Steels Microstructure and Properties, Edward Arnold Publishers Ltd., London, 1981
2. Uggowitzer P. J., Magdowski R.and Spiedel M. O., *Proceedings of Innovation Stainless Steel*, Florence, Italy, Oct. 1993
3. Fagesta Steel Division Catalogue, Fagesta (Pty.) Ltd., Springs, South Africa, 1989
4. Dulieu D. and Nutting J. Metallurgical Developments in High-Alloy Steels., pp. 140-145, *Special Report 86*, The Iron and Steel Institute, 1964.
5. Stainless Steel Buyers Guide, Southern African Stainless Steel Development Association, Rivonia, Sandton, South Africa, 1993
6. Maratray F., *High Carbon Manganese Austenitic Steels*, The International Manganese Institute, Paris, France, 1995
7. Schramm R.E. and Reed R.P., *Metallurgical Transactions A*, Vol 6A, pp. 1345-1351, July 1975
8. Rowlands D.P., Southern African Stainless Steel Development Association, Information Series No. 3, Rivonia, South Africa, April 1990
9. Uggowitzer P. J. and Spiedel M. O., Ultra -High Strength Cr-Mn-N Steels, *Proceedings on International Conference on Stainless Steels*, 1991, Chiba, ISIJ
10. Chandra Holm H, Uggowitzer P.J. and Spiedel M.O., *Scripta Metallurgica*, Vol. 21, pp. 513-518, 1987
11. Llewellyn D.T., *Ironmaking and Steelmaking*, Vol. 20, No. 1, pp. 35-41, 1993
12. Andrews, *Journal of the Iron and Steel Institute*, Vol.184, pp.414, 1956.
13. Espy R. H., *Welding Journal*, Weldability of nitrogen-strengthened stainless steels., Welding Research Supplement, 149s, May, 1982
14. Small W.M. and Pehlke R.D., *Transactions of the Metallurgical Society of AIME*, Vol. 242, pp. 2501-2505 Dec. 1968
15. Turncock P.H. and Pehlke R.D., *Transactions of the Metallurgical Society of AIME*, Vol. 236, pp. 1540-1547, Nov. 1966
16. Rawers J.C. and Kikuchi M., *Journal of Materials Engineering and Performance*, Vol. 2(5), pp. 651-657, Oct 1993
17. Raghavan V., *Metallurgical and Materials Transactions A*, Vol 26A, pp. 237-242, Feb 1995
18. Irvine K.J., Llewellyn D.T. and Pickering F.B., J Iron Steel Inst. Vol 199, P. 153, 1961
19. Holtzgruber W., Proc. Int. Conf., High Nitrogen Steels, The Institute of Metals, pp. 39-48, Lillie, May 1988
20. Rechsteiner A. and Speidel M.O., *Proceedings of Innovation Stainless Steel*, Florence, Italy, Oct. 1993
21. Spiedel M.O., *Proc. Int. Conf. High Nitrogen Steels*, The Institute of Metals, pp. 92-96, Lillie, May 1988
22. Irvine K.J., Gladman T. and Pickering F.B., *Journal of the Iron and Steel Institute*, Vol. 207, pp. 1017-1028, Jul 1969
23. Norström L-A, *Metal Science*, no. 11, pp208-212, June 1977

24. Varin R.A. and Kurzydlowski K.J., *Materials Science and Engineering* A, Vol. 101, pp. 221-226, 1988
25. Rayaprolu R.A. and Hendry A., *Materials Science and Technology*, Vol. 4, pp. 136-145, Feb. 1988
26. Smallman R.E., Modern Physical Metallurgy, Butterworth and Co., pg. 335, 1985
27. Nutting J., The physical metallurgy of alloy steels., *Journal of the Iron and Steel Institute*, Vol. -207, pp. 1017-1028, Jul 1969
28. Cahn R.W., Haasen P. and Kramer E.J. (Eds.), Materials Science and Technology, Pickering F.B. (Ed.), Constitution and Properties of Steels, Vol. 7, pg. 297, VCH Publishers, New York, 1992
29. Cahn R.W., Haasen P. and Kramer E.J. (Eds.), Materials Science and Technology, Mughrabi H. (Ed.), Plastic Deformation and Fracture of Materials, Vol. 6, pg. 513, VCH Publishers, New York, 1992
30. Cahn R.W., Haasen P. and Kramer E.J. (Eds.), Materials Science and Technology, Mughrabi H. (Ed.), Plastic Deformation and Fracture of Materials, Vol. 6, pg. 536, VCH Publishers, New York, 1992
31. Nilsson J.O., *Scripta Metallurgica,* Vol. 17, pp. 593-596, 1983
32. Degallaix S, Dickson J.I. and Foct J., Proc. Int. Conf. High Nitrogen Steels, The Institute of Metals, pp. 380-386, Lillie, May 1988
33. Ledbetter H.M. and Austin M.W., *Materials Science and Technology*, Vol. 3, pp. 101-104, Feb. 1987
34. Byrnes M.L.G., Grujicic M. and Owen W.S., *Acta metall.*, Vol. 35, No. 7, pp. 1853-1862, 1987
35. Gavriljuk V.G., Duz V.A. and Jephimenko S.P., Proc. Conf. High Nitrogen Steels, The Institute of Metals, pp. 447-451, Lillie, May 1988
36. Degallaix S., Foct J. and Hendry A., *Materials Science and Technology*, Vol. 2, pp. 946-950, Sep. 1986
37. Rayaprolu D.B. and Hendry A., *Materials Science and Technology*, Vol. 4, pp. 136-145, Feb. 1988
38. Stoltz R.E. and Vander Sande J.B., *Metallurgical Transactions A*, Vol 11A, pp. 1033-1037, Jun. 1980
39. Fujikura M., Takada K. and Ishida K., *Trans. of the Iron and Steel Inst. of Japan*, Vol. 15, pg. 465, 1975
40. Müllner P., Solenthaler C., Uggowitzer P. and Spiedel M.O., International Conference on Fundermental Aspects of Dislocation Interactions, Ascona, Sep. 1992
41. Angel T., *Journal of the Iron and Steel Institute,* Vol. 165, May 1954
42. Marshall P., *Austenitic stainless steels-microstructure and mechanical properties.*, ElsevierApplied Science Publishers, London and New York, 27, 1984
43. Rayaprolu D.B. and Hendry A., *Materials Science and Technology*, Vol. 5, pp. 328-332, April 1989
44. Kikuchi M., Kajihara M. and Choi S., *Materials Science and Engineering*, A146, pp. 131-150, 1991
45. Presser R. and Silcock J.M., *Metal Science*, Vol. 17, pp. 241-247, May 1983
46. Briant C.L., *Scripta Metallurgica*, Vol. 21, pp. 71-74, 1987
47. Karlsson L., Henjered A., Andrén H.-O. and Nordén H., *Materials Science and Technology*, Vol. 1, pp. 337-343, May 1985
48. Ritter A.M., Henry M.F. and Savage W.F., *Metallurgical Transactions A*, Vol. 15A, pp. 1339-1351, July 1984
49. Jargelius-Pettersson R.A.F., *Scripta Metallurgica et Materialia*, Vol. 30, pp. 1233-1238, 1994
50. Morinaga M., Yukawa N., Ezaki H., *Phil. Mag. A*, , Vol. 51, No. 2, pg. 223, 1985

51. Betrabet H.S., Nishimoto K., Wilde B.E. and Clark W.A.T., *Corrosion* , Vol. 43, No. 2, pp. 77-84, Feb. 1987

52. Sadough Vanini A., Audouard J.-P. and Marcus P., *Corrosion Science*, Vol. 30, No. 11, pp. 1825-1834, 1994

53. Palit G.C., Kain V. and Gadiyar H.S., *Corrosion*, Vol. 49, No. 12, pp 977-991, Dec.1993

54. Oldfield J.W., *Corrosion*, Vol. 46, No. 7, pp. 574-581, July 1990

55. Vinsbo O., *Wear of Materials*, pp. 620-635, 1979

56. Vinsbo O., *Wear of Materials*, pp. 620-635, 1979

57. Kushchov M.M. and Babichev M.A. *Friction and Wear in Machinery*, Vol. 12, pp. 12-26, 1972

58. Ludema K.C. Selecting Materials for Wear Resistance.

59. Suh N.P. *Wear*, Vol. 62, pp. 1-20, 1980

60. Zum Gahr K.H. and Mewes D., *Wear of Materials*, pp. 103-139, 1983

61. Moore M.A., *Wear*, Vol. 27,pp. 1-17, 1974

62. Barker K.C., P.hD Thesis, University of Cape Town, Cape Town, 1988

63. Rigney D.A.and Glaeser W.A. *Structural Materials and Tribology*, Service Characteristics Section, Bettlelle, Colombus Laboratories; pp. 597-638, 1977

64. Richardson R.C.A. *Wear*, Vol. 10, pp. 353-382, 1967

65. Garrison W.M. and Garriga R.A., *Wear*, Vol. 85, pp. 347-360, 1983

66. Ball A., *Wear*, Vol. 91, pp. AISI 201-207, 1983

67. Allen C., Protheroe B.E. and Ball A., *Wear*, Vol. 74, pp. 287-305, 1981-1982

68. Moore M.A., Richardson R.C.D. and Attwood D.G., *Metallurgical Transactions*, Vol. 3, pp. 2485-2491, 1972

69. Avery H.S., Symposium - Materials for the Mining Industry, Barr R.Q. (Ed.), Climax Molybdenum Company, pp. 43-76, 1974

70. Hawk J.A., Simmons J.W. and Rawers J.C., *Journal of Materials Engineering and Performance*, Vol. 3(2), pp 259-272, April 1994

71. Campillo Illanes B.F. and Sarkar A.D., *Journal of Tribology*, Vol. 108 pp 334-339, July 1986

72. Wei R., Wilbur P.J., Sampath W.S., Williamson D.L. Yi Qu and Wang L, *Journal of Tribology*, Vol. 112 pp 27-36, July 1990

73. Moore M.A., *Fundamentals of Friction and Wear of Materials*, Materials Science Seminar, American Society of Metals, Pittsburgh, Pennsylvania, 1980

74. Postlethwaite J., Tinker E.B. and Hawrylak M.W, *Corrosion*, Vol. 30(8), pp. 285-290, 1974

75. El-Koussy R., El-Raghy S.M. and El-Mehairy A.E., *Tribology International*, pp. 323-328, Dec. 1981

76. Dunn D.J., Proceedings of the International Conference on Wear of Materials., Kudema K.C. (Ed), ASME, New York, 1985

77. Noël R.E.J., The abrasive-corosive wear behaviour of metals., M.Sc. Thesis, University of Cape Town, Cape Town, 1981

78. Karimi A. and Martin J.L., *International Metals Review*, Vol. 31, No. 1, 1986

79. Lord Rayleigh, *Philos. Mag.*, Vol. 34, pp. 94-98, 1917
80. Kornfeld m. and Suvorov L., *Journal of Applied Physics*, Vol 15, pp. 495-503, 1944
81. Vaidya S. and Preece C.M., *Metallurgical Transactions A*, Vol. 9A, pp. 299-307, 1978
82. Goebel J.A. and Petit F.S., *Metallurgical Transactions*, Vol. 11, pg. 1943, 1970
83. Thiruvengadam A. and Waring S., *J. Ship. Res.*, Vol. 10(1), pg. 1, 1966
84. Hobbs M.J., in Erosion by Cavitation or Impingement., ASTM, STP, 408, pg. 159, 1967
85. Heymann F.J. in Characterization and determination of erosion resistance., ASTM, STP 474, pp. 212-284, 1970
86. Hammitt F.G. in Characterization and determination of erosion resistance., ASTM, STP 474, pp. 288-322, 1970
87. Richman R.H. and McNaughton, *Wear*, Vol. 140, pp. 63-82, 1990
88. Ahmed S.M., Hokkirigawa K. and Oba R., *Wear*, Vol. 177, pp. 129-137, 1994
89. Woodford D.A. *Metallurgical Trans.*, Vol. 3, pg. 1137, 1972
90. Heathcock C.J., Protheroe B.E. and Ball A., *Wear*, Vol. 80, pp. 311-327, 1982
91. Heathcock C.J., P.hD Thesis, University of Cape Town, Cape Town, 1980
92. Zylla I.-M. and Hougardy H.P., *Steel Research*, Vol. 65, No. 4, pp. 132-137, 1994